NONLINEAR FINITE ELEMENT MODELING OF THE IMPACT OF BRITTLE ROCK PARTICLES AGAINST A FLAT METALLIC SURFACE

SAMUEL GUSTAVO ALVES ARAÚJO

DISSERTAÇÃO DE MESTRADO EM CIÊNCIAS MECÂNICAS
DEPARTAMENTO DE ENGENHARIA MECÂNICA

FACULDADE DE TECNOLOGIA

UNIVERSIDADE DE BRASÍLIA

UNIVERSIDADE DE BRASÍLIA
FACULDADE DE TECNOLOGIA
DEPARTAMENTO DE ENGENHARIA MECÂNICA

NONLINEAR FINITE ELEMENT MODELING OF THE IMPACT OF BRITTLE ROCK PARTICLES AGAINST A FLAT METALLIC SURFACE

SAMUEL GUSTAVO ALVES ARAÚJO

Orientador: PROF. DR. THIAGO DOCA, ENM/UNB

DISSERTAÇÃO DE MESTRADO EM CIÊNCIAS MECÂNICAS

PUBLICAÇÃO PCMEC.DM - XXX/AAAA
BRASÍLIA-DF, 21 DE OUTUBRO DE 2021.

UNIVERSIDADE DE BRASÍLIA
FACULDADE DE TECNOLOGIA
DEPARTAMENTO DE ENGENHARIA MECÂNICA

NONLINEAR FINITE ELEMENT MODELING OF THE IMPACT OF BRITTLE ROCK PARTICLES AGAINST A FLAT METALLIC SURFACE

SAMUEL GUSTAVO ALVES ARAÚJO

DISSERTAÇÃO DE MESTRADO SUBMETIDA AO DEPARTAMENTO DE ENGENHARIA MECÂNICA DA FACULDADE DE TECNOLOGIA DA UNIVERSIDADE DE BRASÍLIA COMO PARTE DOS REQUISITOS NECESSÁRIOS PARA A OBTENÇÃO DO GRAU DE MESTRE EM CIÊNCIAS MECÂNICAS

APROVADA POR:

Prof. Dr. Thiago Doca, ENM/UnB
Orientador

Prof. Dr. Jorge L.A. Ferreira, ENM/UnB
Examinador interno

Prof. Dr. Ariosto Bretanha Jorge, UNIFEI/Itajubá
Examinador externo

Prof. André Teófilo Beck, USP/ São Carlos
Examinador externo

BRASÍLIA, 21 DE OUTUBRO DE 2021.

FICHA CATALOGRÁFICA
SAMUEL GUSTAVO ALVES ARAÚJO
NONLINEAR FINITE ELEMENT MODELING OF THE IMPACT OF BRITTLE ROCK PARTICLES AGAINST A FLAT METALLIC SURFACE
2021xv, 74p., 201x297 mm
(PCMEC/FT/UnB, Mestre, Ciências Mecânicas, 2021)
Dissertação de Mestrado - Universidade de Brasília
Faculdade de Tecnologia - Departamento de Engenharia Mecânica

REFERÊNCIA BIBLIOGRÁFICA

SAMUEL GUSTAVO ALVES ARAÚJO (2021) NONLINEAR FINITE ELEMENT MODELING OF THE IMPACT OF BRITTLE ROCK PARTICLES AGAINST A FLAT METALLIC SURFACE. Dissertação de Mestrado em Ciências Mecânicas, Publicação xxx/AAAA, Departamento de Engenharia Mecânica, Universidade de Brasília, Brasília, DF, 74p.

CESSÃO DE DIREITOS

AUTOR: Samuel Gustavo Alves Araújo
TÍTULO: NONLINEAR FINITE ELEMENT MODELING OF THE IMPACT OF BRITTLE ROCK PARTICLES AGAINST A FLAT METALLIC SURFACE.
GRAU: Mestre ANO: 2021

Samuel Gustavo Alves Araújo
Campus Darcy Ribeiro, Asa Norte. Faculdade de Tecnologia, Departamento de Engenharia Mecânica

Agradecimentos

Agradeço, primeiramente, a Deus.

Aos meus pais, Adão Batista de Araújo e Maria das Graças Alves Araújo, por não medirem esforços em toda minha trajetória acadêmica.

Ao Prof. Doca pelas oportunidades, o constante acompanhamento, disposição e incentivo para realização deste trabalho.

À minha noiva, Vitoria Vieira, que me apoiou de forma perene e tornou possível a realização desta conquista.

E a todos meus amigos do curso,e família, por ensinamentos, companheirismo e por fazerem parte da minha formação.

Muito obrigado!

Samuel Gustavo Alves Araújo

Resumo

Este trabalho aborda a influência da geometria e velocidade de impacto no processo de fratura de projéteis rochosos. A análise inclui seis geometrias distintas projetadas contra um anteparo plano metálico. Três tipos de materiais são estudados (granito, arenito e concreto) sob efeito de quatro velocidades de impacto (10, 20, 40 e 60 m/s). São realizadas comparações de parâmetros como tensão efetiva, deformação e rigidez para cada situação. É empregado o método de elementos finitos para a modelagem do fenômeno de impacto por meio do pacote comercial Abaqus®. Para realizar a análise não linear (incluindo o dano e a perda de rigidez do material), utilizou-se um modelo de dano plástico (Concrete Damage Plasticity). Já para análise do anteparo metálico utilizou-se o modelo de Johnson-Cook. Observou-se que a inclusão dos fenômenos de dano e plasticidade são fundamentais para a precisa representação do comportamento dos materiais analisados. Esse estudo inclui uma etapa de avaliação qualitativa e uma quantitativa dos resultados. A análise quantitativa apresenta análises gráficas da influência do aumento da velocidade de impacto para cada tipo de projétil com sua respectiva geometria e característica material. A análise qualitativa demonstra por meio de imagens e tabelas o percentual de dano do projétil após colidir com o plano metálico. Ao avaliar os resultados obtidos, é observada uma influência direta da velocidade de impacto, da geometria e do tipo de material no dano causado no anteparo metálico e nos projéteis. Verificou-se que o projétil de granito, o material analisado com a menor porosidade e com maior resistência mecânica, é aquele que produz maiores tensões e deformações no anteparo. Adicionalmente, dentre todas as geometrias analisadas, ele é também o que menos se danifica. De maneira geral, o comportamento observado nos modelos implementados permitem avaliar os efeitos mecânicos de impactos singulares e continuados. Tal ferramenta pode ser empregada na análise de problemas industriais visando a redução de custo, otimização de vida útil e desempenho.

Palavras-chave: impacto mecânico, fratura, análise não linear, elementos finitos, materiais rochosos.

Abstract

This work addresses the influence of geometry and impact velocity on the fracture process of rock projectiles. The analysis includes six distinct geometries designed against a flat metallic counterpart. Three types of materials are studied (granite, arenite and concrete) under the effect of four impact velocities (10, 20, 40 and 60 m/s). Parameter comparisons such as effective stress, strain and stiffness are performed for each situation. The finite element method is used to model the impact phenomenon through the commercial package Abaqus®. To perform the non-linear analysis (including material damage and loss of stiffness), a plastic damage model (Concrete Damage Plasticity) was used. For the analysis of the metallic counterpart, the Johnson-Cook model was used. It was observed that the inclusion of damage and plasticity phenomena are fundamental for the accurate representation of the behavior of the analyzed materials. This study includes a qualitative and a quantitative evaluation stage of the results. Quantitative analysis presents graphical analysis of the influence of the increase in impact velocity for each type of projectile with its respective geometry and material characteristics. Qualitative analysis demonstrates through images and tables the percentage of damage of the projectile after colliding with the metallic plane. When evaluating the obtained results, it is observed a direct influence of the impact velocity, geometry and type of material in the damage caused to the metallic shield and in the projectiles. It was found that the granite projectile, the material analyzed with the lowest porosity and the highest mechanical strength, is the one that produces the highest stresses and deformations in the bulkhead. Additionally, among all the analyzed geometries, it is also the one that is least damaged. In general, the behavior observed in the implemented models allows evaluating the mechanical effects of singular and continuous impacts. Such tool can be used in the analysis of industrial problems aiming at cost reduction, optimization of useful life and performance.

Keywords: mechanical impact, fracture, nonlinear analysis, finite elements, rock materials.

SUMMARY

LIST OF FIGURES

LIST OF TABLES

SYMBOLS

σ - Stress [MPa]

K - Plastic deformation resistance coefficient

n - Strain hardening coefficient

A - Initial yield stress [MPa]

B - Plastic resistance constant [MPa]

ϵ - Plastic strain

n - Plastic strain index (work hardening index)

C - Strain Rate Sensitivity coefficient

ϵ_{eq} - Equivalent plastic strain rate

ϵ_0 - Reference plastic strain rate

T - Body temperature [C]

T_r - Reference temperature [C]

T_m - Body temperature [C]

m - Softening coefficient

$d1$ to $d4$ - Material damage constants

e - Coefficient of restitution

v - Poisson's ratio

u^{pl} - Damage evolution law in terms of displacement

${\epsilon_0}'^{pl}$ - Equivalent plastic deformation at the onset of damage

${\epsilon_f}'^{pl}$ - Plastic deformation at fault

D_{Abq} - Global damage

ρ - Density [kg/m³]

σ_y - Elastic limit [MPa]

E - Elastic modulus [GPa]

ε' - Total deformation rate

ε'^{pl} - Elastic Deformation Rate ε^{pl} - Plastic deformation rate

D_0^{el} - Elastic stiffness of the material (without damage)

${\varepsilon_v}^c$ - Volumetric deformation of fracture

ε_v - Total volumetric deformation

${\varepsilon_v}^e$ - Elastic volumetric deformation

Chapter 1

INTRODUCTION

This chapter presents the basic definitions impact phenomena, the motivation, the objective and the adopted textual structure.

1.1 State-of-the-Art review

Impact mechanics is the part of mechanics that studies the collision of solid bodies. It has been the subject of intense research in forensic science, ballistics and industrial applications such as manufacture processes, car crash tests, satellite shields and oil prospection. This phenomena is characterized by the production of relatively high contact forces that act for a brief period of time and it develops strains, material recovery, dissipation of heat and sound. Moreover, large variations in the impact process are caused by small variations in impact conditions, making it quite complex. For this reason, this loading condition is rather difficult to reproduce both in an experimental and numerical setting [1].

The impact phenomena is can be divided into four main stages: contact, yielding, damage and fracture. The brief description of the main advances in these fields are briefly described in the following.

1.1.1 Contact mechanics

Theories of contact mechanics study the behavior of solids in contact, subjected to a given load, in order to determine the corresponding displacements, strains and effective stresses. These theories were established in the field of Elastic Continuing Media Mechanics between 1880 and 1895, using the theory of Boussinesq and Cerutti for the analysis of elastic semi-spaces, and the Hertz theory for the normal contact between elastic solids [8–10]. There is the presence of mechanical contact in almost all manufacturing processes, natural phenomena and in our daily activities, with contact and friction being practically a prerequisite for stress/deformation and movement to occur [11].

A more realistic solution was developed by Hertz where the theory of elasticity was applied in order to obtain an analytical solution to describe the stresses and strains close to the contact point. Other approximations were developed, but due to the complexity in dealing with the nonlinearity associated with the contact area, the number of problems that could be solved remained very limited [11]. It was only in the mid-1970s, with the development of digital computers and finite element codes, based on the Penalties and Lagrange multiplier methods, that it was possible to obtain a numerical solution to a large number of contact problems. Contact problems can be classified as: conforming contact, non-conforming contact, frictional contact and frictionless contact.

- Conformal contact occurs when bodies in contact touch each other at multiple points before deforming;
- Non-conforming contact, the shapes of bodies cause them, without charge, to touch each other at a point or along a line. In this case, the contact area is finite although very small when compared to the dimensions of the two bodies, causing the stresses to be strongly concentrated in these areas;
- In frictionless contact, there is slip between solids without resistance in the direction tangential to the contact surface;
- Frictional contact can occur with or without tangential slip.

When two bodies come into contact, it generates a highly non-linear problem, as there is a non-linear behavior due to the dissipation energy associated with the friction contact and also because the contact area evolves in a non-linear way. The linear hypothesis is only valid under special circumstances and usually involves small deformations and small displacements. These 6 approximations are made by providing a simplified resolution method. However, with the evolution of technology and computational mechanics, the solution of several problems that include non-linear contact phenomena could be obtained numerically [11].

1.1.2 Yielding of brittle materials

Brittle and ductile materials, after application of sufficiently high stresses, present an irreversible deformation, limit is known by several names, such as elastic limit, yield point or yield stress. From this stress value, the stress-strain relationship is no longer linear, and the strain assumes, even partially, permanent values. Nonlinearity is commonly associated with a plastic flow induced by stress in the material, which starts to allow a rearrangement in its microscopic structure, in which atoms are being reasons for new equilibrium positions [12]. This plasticity requires a mechanism for atomic or molecular mobility. Therefore, fragile materials are those that do not allow this mobility and prevent the movement of blocks. Otherwise, the ductile materials allow this type of mobility, and the deformation resulting

from the rearrangement associated with plastic flow in these materials is not reversible in its entirety after removal of stress. The yield point is directly linked to plastic deformation, which can be defined as the stress required to induce plastic deformation in the material. The identification of this point is not always straightforward in stress x deformation graphs, considering that not all curves show a marked separation between the end of the elastic behavior, characterized by the linear relationship between stress and deformation, and the beginning of the plastic behavior, in that this relationship is no longer linear. In some materials, you can see a sharp inflection point or region that demonstrates the separation between the two behaviors. Fragile materials only exhibit elastic behavior.

Yield can be measured in several different ways depending on the type of material and the type of test being performed (stress, compression, etc). The most important results of measuring yield are yield strength and yield stress, as these values are often used to assess whether or not a material is suitable for a particular application. Yield strength is particularly important as it is necessary to determine whether a material meets a required safety factor. The Factor of Safety is determined by dividing the yield strength by the maximum effective applied stress [13]. Ceramic materials usually do not show plastic deformation. Therefore, the yield point is also its breaking strength.

1.1.3 Damage mechanics

The mechanics of damage in continuous media takes into account the effects of degradation, in a diffuse and progressive way, of solids submitted to actions of a mechanical nature or not, through the reduction of the material's strength and stiffness properties. It deals with the effect, on the material response, of a distributed microcracking process that is returned in a preliminary stage to the formation of the discrete crack [14].

Cracks can be modeled in three ways [15]:

- Discrete: the crack is modeled by separating the edges of the elements. In finite element application, unless the crack trajectory is known in advance, discrete cracks are modeled by changing the mesh to support propagation.
- Distributed: the discontinuity of the displacement field caused by the crack is spread along the element, which has its constitutive equation altered.
- Embedded: There is no need to redefine the mesh and the results obtained are independent of the finite element mesh used. This model is based on the concept of discontinuities embedded within standard finite elements.

Isotropic damage formulations are extensively used in the literature due to their simplicity, efficiency and suitability for many practical applications. These isotropic damage models represent the nonlinear behavior of the material through an internal scalar damage

variable known as degradation, d. In view of this, it is possible to describe locally, considering an element of representative volume of material around the considered point, the evolution of the phenomena that develop between an initial state, relative to a situation of intact material, and a final state, characterized by the formation of a macroscopic crack, which is equivalent to the rupture of the volume element.

Damage mechanics is the study that evaluates materials when they are subjected to certain levels of stress or unfavorable conditions, which generate changes in their properties, whether macroscopic or microscopic. Considering that the changes imply the alteration of the material's mechanical properties, it is possible to consider that the damage is a process of progressive physical degradation existing before the material's failure [16]. Damage mechanics considers micro-defects distributed homogeneously and defects continuously distributed in a certain region or in the entire body. This differs from fracture mechanics, which represents discrete defects in the material and considers that the strength of a structure is affected by a particular defect, and the surrounding environment can be considered intact. Macro-mechanics and micro-mechanics can be more precisely exemplified by the continuum damage theory and Griffith's theory, respectively, this being used to formulate the theory of fracture mechanics [17, 18].

1.1.4 Fracture mechanics

Fracture Mechanics is an area of engineering that study the integrity failure of a solid body due to the propagation of a cracks. It entails the behavior of defects inherent to materials, such as discontinuities introduced during the manufacture of a structural component and damage produced during operation. Although materials are not flawless, simplifying them as a continuous and homogeneous medium is one of the solutions found to provide an understanding of some structural characteristics in engineering [19]. The fracture due to high speed impacts is characterized by a localized response observed in the target, which causes an energy dissipation in a small region. Thus, considering the punctuality of the deformation, the critical region is under high stress, while the remaining of the solid do not perceive the a significant load. In this situation, stresses are transferred through the body, at specific speeds (which is known for some materials [20]) leading to the separation of its layers.

The stress and displacement fields at the crack tip are dependent on the forces that gave rise to the crack. Therefore, it is extremely important to understand and classify the rupture modes of materials. The three rupture modes are called mode I, mode II and mode II, shown in the Figure 1.1. The predominant efforts to:

- Mode I is normal stress;
- Mode II is shear stress in the y and x direction;
- Mode III is shear stress in the y and z directions.

In real situations, solids are usually requested from the billing so that the different failure modes occur simultaneously. The interaction between the rupture modes and their intensities determines, among others, the trajectory from the crack to the collapse [21].

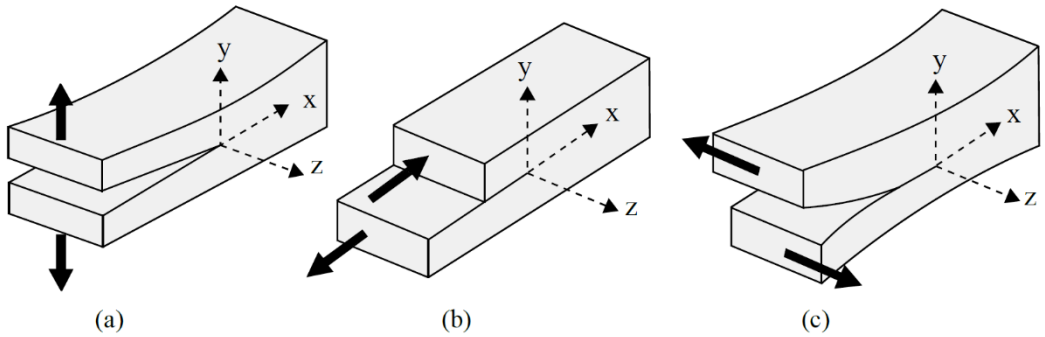

Figure 1.1: Crack mode: (a) Mode I (or open mode), (b) Mode II (or slip mode), (c) Mode III (or anti-plane shear mode)

Fracture mechanics can be divided into:

- Linear elastic: defined as the study of stress and displacement fields in the crack tip region in predominantly elastic, homogeneous and isotropic material, particularly at the beginning of unstable fracture growth. This theory is applicable for brittle materials with minimal inelastic behavior.
- Non-linear: materials that have a predominantly linear elastic behavior, cracks are well described, and the non-linear fracture zone is very small. However, it does not apply to nearly fragile materials such as rocks. For this reason, there was a need to expand the concepts of linear elastic fracture mechanics through non-linear, aiming to describe the fracture in materials that have non-linear behavior.

1.2 Motivation

The impact rock particles on protective layers is a topic not yet fully understood. It has a wide range of non-trivial aspects such as energy transfer, inertia effects, contact, inelastic material behavior, rate effects, buckling, damage and fracture [22]. The problem of the impact of brittle materials on ductile surfaces is frequently observed in our daily lives, such as the impact of sedimentary stones on mowers during lawn mowing, on the wheel fender of a car or the gravel spilled by trucks that just had to hit your windshield. These situations cause damage to appliances and can lead to safety hazards. In order to mitigate these issues numerical simulations are often employed as a tool.

Nowadays the numerical simulations are used in several areas, such as companies and universities, in order to carry out structural analyzes and investigate phenomena with the

intention to make as the experimental study less expensive in terms of resource, time and test execution. Another advantage in using numerical simulation is that it makes it possible to change analysis parameters, such as geometries and thicknesses, without the use of costly tests [23]. A model often used to describe of the behavior of the material when subjected to high strain rates is the Johnson-Cook formulation [24]. It considers the von Mises stress effects of plastic deformation and hardening, modified by the strain rate and temperature, as independent effects that can be isolated. To evaluate the behavior of the material aiming at its physical nonlinearity, the best solution to be adopted is the Concrete Damaged Plasticity (CDP).

1.3 Research objective

The present work intends to study the impact between brittle rock particles and a metallic counterpart. Its main objective is to evaluate the influence of the material type, geometry and impact velocity into the fracture of the particles and the observed effect on the counterpart. It aims at an academic contribution in the field of numerical simulation of the projectile impact against a flat surface.

Herein, the impact is defined as inelastic, considering that there is no conservation of kinetic energy. The study assess six different geometrical contact configurations and for each one three materials are employed: arenite, granite and concrete. As loading conditions, four impact speeds (10, 20, 40 and 60 m/s) are considered. Therefore, 72 different impact conditions are evaluated. The numerical simulations are developed in the commercial package Abaqus®. For the analysis of plastic deformation and damage of the target material, the Johnson-Cook model is considered. For the non-linear analysis of the projectile, the effects of stress, plasticity and damage implemented in with the CDP model are considered. Since the analysis of large impact-related problems requires an extremely high computational cost, the phenomenon was initially studied in a simplification of the three-dimensional configuration, limiting the size of the plane. However, for the projectile real characteristic sizes are considered. In view of the aforementioned considerations, the final objective of the work is to understand the behavior of the two materials after impact with the variation of geometry, material and projectile impact velocity.

1.4 Text structure

Aiming the achievement of the proposed objective, the work was divided into five chapters. The first chapter presents the contextualization through the introduction, the description of the problem and the objective of the dissertation.

The second chapter describes the main theoretical concepts for the development of the

work. Initially, the impact theory is discussed, followed by the mechanics of fracture and rock damage. The third part exposes the finite element methodology. Finally, the constitutive models used in the work for ductile and non-linear materials, the Johnson-Cook constitutive model and the damage and plasticity model of concrete are discussed.

The third chapter presents the implementation steps, which consists of a detailed description of the development of numerical simulations, using the specific concepts of the software used. This chapter describes the material properties, as well as the geometry of the simulated bodies and the type of mesh used.

The fourth chapter presents the analysis of the results. It was subdivided into two subjects: qualitative analysis and quantitative analysis. The qualitative analysis exposed, through images extracted from simulations and tables, the percentage of damage of each projectile after the impact with the plane, in addition to presenting the maximum equivalent von Mises stress for each geometry. For the quantitative analysis, graphs related to the results obtained in the computer simulations were generated.

Lastly, chapter five presents the conclusions and observations about the studies carried out in this dissertation, which deserve special attention, since in addition to verifying the results obtained in this work, possible future studies in different works were also suggested.

Chapter 2

THEORETICAL BACKGROUND

This chapter presents definitions on Impact mechanics, Fracture mechanics, Brittle rock materials and Numerical modeling.

2.1 Impact mechanics

When bodies experience impact, they are in contact for a brief period of time and subjected to a force that evolves in a complex way. Those forces are called impulsive forces. Impulsive forces acting on impact are internal forces that do not influence the conservation of the total linear momentum of the system. However, even though the total linear momentum is always conserved during impact, the kinetic energy might not be conserved. Therefore, the impact can be classified as:

- Elastic Impact: conserved kinetic energy;
- Inelastic Impact: no conservation of kinetic energy;
- Perfectly elastic impact: the loss of initial kinetic energy is as high as possible and compatible with the conservation of linear momentum.

2.1.1 Direct Central Impact

As an introductory impact analysis, we can take as a basis the co-linear motion of two spheres with masses m_1 and m_2, as shown in Fig. 2.1a, moving with velocity v_1 and v_2. If we consider that v_1 is greater than v_2, the condition called direct central impact occurs, which is when the collision occurs with the contact forces directed along the line of centers.

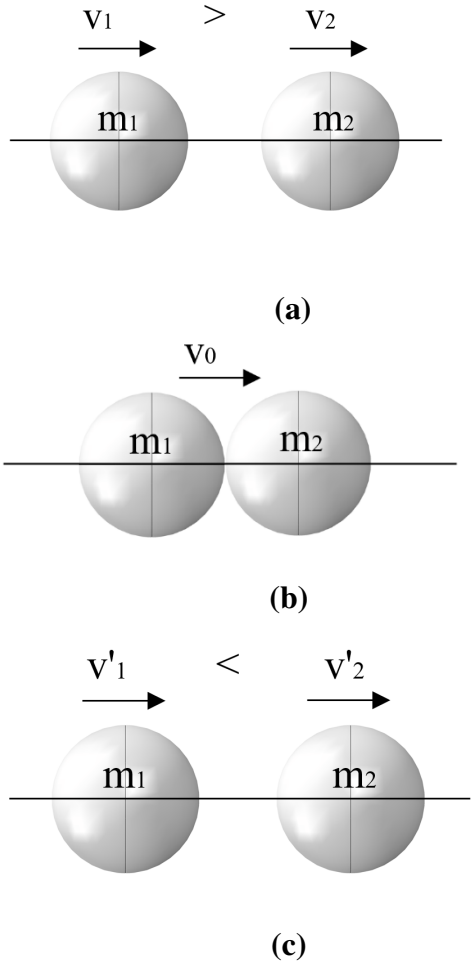

Figure 2.1: Impact of spheres. (a) Before impact (b) Maximum deformation during impact (c) After impact. Modified from [1].

After the initial contact of the spheres, the deformation increases for a short period until the area of contact between the spheres no longer increases. At this moment, the two spheres move with the same velocity v_0, as shown in Fig. 2.1b. As a result, throughout the remaining contact, a restoration period ensues, in which the contact area decreases to zero. In Fig. 2.1c, it represents the final condition, where the spheres have new velocities $v_1^{'}$ and $v_2^{'}$, where $v_1^{'}$ is necessarily smaller than $v_2^{'}$. It is important to emphasize that the direction of the velocities was defined for a better understanding of the situation, where the velocities considered positive will be to the right, so that with this notation, scaling a velocity to the left will receive a negative sign. And if the impact is of a light nature, generating low efforts to the point that the spheres do not plastically deform, they will recover their original shape, however, if the impact generates high efforts, plastic deformation can occur [1].

The amount of linear movement of the system between the spheres does not change as the contact forces are of the same magnitude and opposite during impact. Therefore, it is possible to apply the law of conservation of linear momentum, obtaining Eq. (2.1). Assuming that only the internal contact forces will be high, and any other forces acting on the phenomenon are relatively small, and end up producing negligible impulses when

related to internal contact forces. And considering that there is no significant variation in the positions of the centers of mass over the short contact time.

$$m_1 v_1 + m_2 v_2 = m_1 v_1' + m_1 v_2'. \tag{2.1}$$

2.1.2 Coefficient of Restitution

From equation (2.1), we can note that given the mass and initial conditions, we will have two unknowns in the equation, v_1' and v_2'. This requires an additional ratio to find the final speeds. This relationship can be found from the impact recovery capacity of bodies in contact, it is represented by the ratio e, known as restitution coefficient.

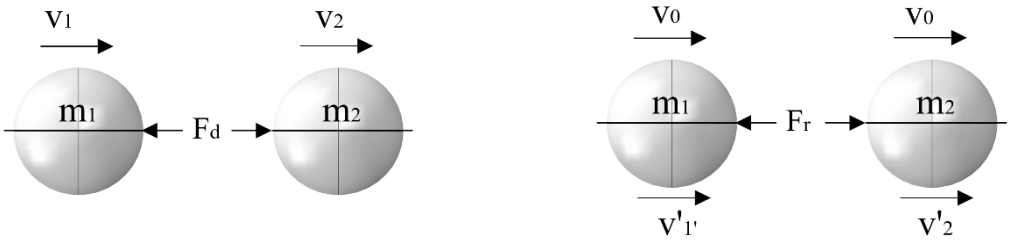

Figure 2.2: Sphere impact (a) Before impact (b) Maximum deformation during impact (c) After impact. Modified from [1].

From Figure 2.2 it is assumed that F_r and F_d represent the modules of the contact forces during the restoration and deformation periods, respectively. Defining the restoration coefficient together with the momentum-amount of motion equation provides equation (2.2).

$$e = \frac{\int_t^{t_0} F_r dt}{\int_{t_0}^{0} F_r dt} = \frac{m_1[-v_1' - (-v_0)]}{m_1[-v_0 - (-v_1)]} = \frac{v_0 - v_1'}{v_1 - v_0} \tag{2.2}$$

Likewise, for particle two, it gives equation (2.3).

$$e = \frac{\int_t^{t_0} F_r dt}{\int_{t_0}^{0} F_r dt} = \frac{m_1[-v_2' - (-v_0)]}{m_1[-v_0 - (-v_2)]} = \frac{v_0 - v_2'}{v_2 - v_0}, \tag{2.3}$$

where:

- t_0 is the deformation time;
- t is the total impact time.

In Eq.s (2.2) and (2.3) it is necessary to be careful in expressing the variation of the amount of movement in the same direction as the impulse. By eliminating v_0 in the two

expressions, the restitution coefficient is obtained,

$$e = \frac{v_0 - v_2'}{v_2 - v_0}. \tag{2.4}$$

2.1.3 Energy Loss

Impact phenomena are always related to energy loss, which can be found by subtracting the kinetic energy of the system right after the impact minus the kinetic energy just before the impact occurs. This energy is lost through the means of heat generation during the localized inelastic deformation of the material, through the generation and dissipation of elastic tension waves inside the bodies and the generation of sound energy.

According to classical impact theory:

- e = 1 (Elastic impact): Recovery capacity of the two particles is equal to their tendency to deform;
- 0 < e < 1 (Inelastic impact): Kinetic energy is not conserved.
- e = 0 (Perfectly inelastic or plastic impact): The particles adhere to each other after the collision and the energy loss is maximum.

Importantly, all impact conditions fall between these two extremes. However, it should be noted that a restitution coefficient must be associated with a pair of bodies in contact. The restitution coefficient, e, is normally considered a constant for certain geometries and a given combination of materials in contact. To be more exact, this depends on the impact velocity and approaches unity as the impact velocity approaches zero, as depicted in Fig. 2.3.

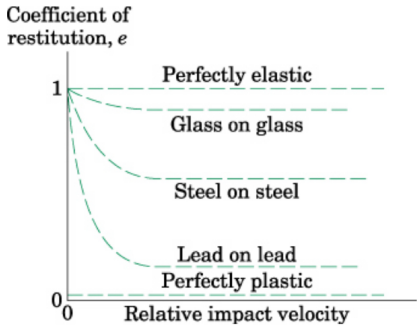

Figure 2.3: Restitution coefficient x relative impact velocity [1]

2.1.4 Contact Mechanics

Contact problems involve several factors that influence the form of the problem, which can make it extremely complex. The variation in temperature, roughness, or some mechanical action, individual material parameters (e.g., fragility, plasticity, etc.) and the change in

its geometry are factors that illustrate the diversity of effects that can be considered in mechanical problems of the contact [25]. When two nonconforming bodies are in contact they initially touch each other at a single point or along a line. Under the action of a small load they deform in the vicinity of their first point of contact causing them to start touching over a finite area, but very small compared to the dimensions of the two bodies. A contact theory is needed to predict the shape of this contact area and how it grows with increasing applied load. The contact between two similar elastic bodies occurs by the application of a force or a displacement, which generate a contact length. One of the approaches for solving a mechanical contact problem involves the analytical formulation based on the Hertz formulae and on the formulation of Cattaneo-Mindlin [26–28]. The first satisfactory analysis of the contact stresses of two elastic solids was formulated by Heinrich Hertz. The analytical equations developed by Hertz generate results that can be compared to results from numerical simulations of a finite element program. The assumptions made by Hertz can be summarized as follows:

- Surfaces are continuous and non-conforming;
- Deformations are small;
- Each solid can be thought of as an elastic half-space;
- There is no friction.

Thus, to ensure the first three hypotheses, it is necessary that the contact area is much smaller than the radius of the analyzed body. As it considers small deformations, the body must be analyzed only in the elastic regime, with no deformations occurring [29]. According to [30], contact conditions can be classified as:

- Unilateral contact problems: bodies can come into contact with each other, closing an initial gap between them, but they cannot penetrate each other;
- Friction contact problem: two or more bodies, under a given load and boundary conditions, can contact each other closing an initial gap between them. Soon after, the sliding movement between them opposes the friction force;
- Friction problem: two or more bodies are already in contact with each other, under a given load and boundary conditions the friction force resists the sliding movement between them;
- Hertzian problem: frictionless contact between elastic solids with characteristic geometries (planes, cylinders and spheres);
- Indentation problems: when a solid of acute geometry (cone or prism) promotes indentation on a flat surface. This setting is used in surface hardness tests;

- Cattaneo-Mindlin problems: contact with friction, small elastic deformations and small displacements;
- Signorini problems: motion constraints are satisfied on both sides of the interface and at any point of contact.

2.2 Fracture mechanics

The analysis of crack propagation is vitally important to understand the behavior of structures and define engineering solutions, considering that the presence of these faults is responsible for changing the stress state in the vicinity. Initially, studies on the influence of these failures were mostly carried out through laboratory tests and practical experiments. However, there are several methods to detect damage, such as visual inspection techniques, X-rays, dynamic methods, magnetic methods, penetrating liquids, eddy currents, radiography, ultrasound and acoustic emissions. The basis of fracture mechanics is based on the criteria below:

- Griffith's energy criterion, which consists of evaluating the energy capable of producing the unstable propagation of a pre-existing crack, thus determining the body's carrying capacity;
- Irwin's stress intensity factor criterion, in which it is assumed that crack propagation is a function of the stress state near the end of the crack.

The stress-strain curve obtained from the compression tests, whether uniaxial or triaxial, can be divided into several regions or zones, as has been discussed by different authors [2, 17, 31–36], where the behavior of the rock changes with axial deformations.

Zone I: clearly presents the results of uniaxial compression, characterized by a positive concavity caused by the closure of pre-existing fractures in the rock, shown in Fig. 2.4. The phenomenon is little noticed in triaxial tests, considering that the stress of confinement can lead to fracture closure, and would not be recorded in the axial loading step. In zone I, the deformation is considered as non-linear elastic, although there are signs of localized deterioration of the material and its crushing [35]. There is no acoustic emission.

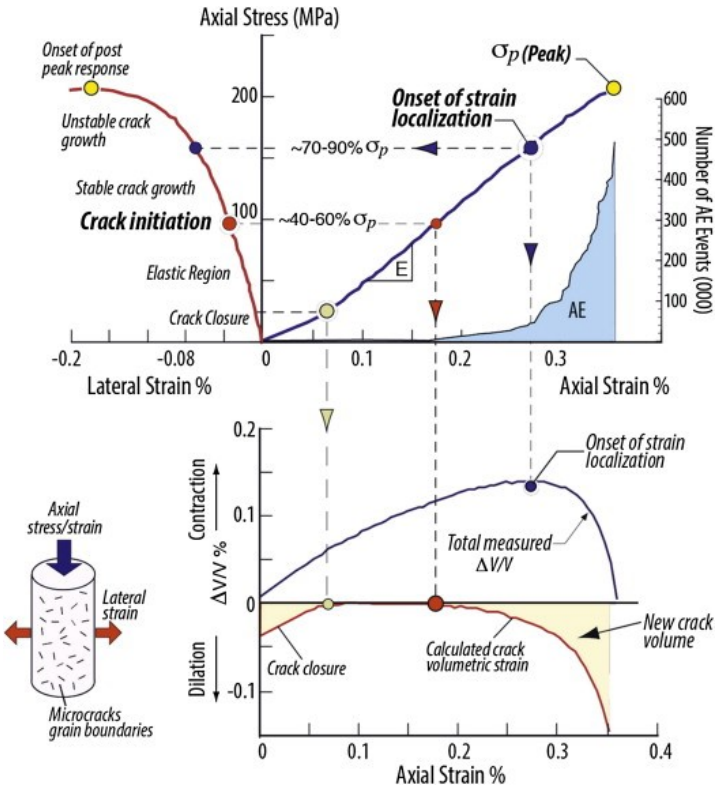

Figure 2.4: Schematic of the stress-strain curve under compression conditions with regions or zones with different behavior [2].

Zone II: this is the linear elastic deformation step, shown in Fig. 2.4. The range that the zone can reach depends on the type and rock analyzed, the confinement stress and the sensitivity in obtaining the results (a low sensitivity cannot capture rapidly changing behavior to nonlinear and consequently increasing the elastic zone range). At this stage, there are some signs of irreversible processes due to hysteresis in the material's behavior. There is no acoustic emission.

Zone III shows a progressive departure from the linear behavior, shown in Fig. 2.4, as the material begins to dilate, slightly increasing the acoustic emissions, reducing the speed of elastic waves, increasing the apparent Poisson coefficient, among other signs [17, 35]. The beginning of this step, point b in figure 5, usually happens between 30% and 70% of the maximum resisted stress. This stress is commonly known as fracture onset stress (σ_{ci}) and is associated with the stable generation of tensile fractures. (σ_{ci}) can be better identified by plotting the volumetric deformation curve of fractures ϵ_v^c versus axial deformation being the first calculated according to Eq. (2.5).

$$\epsilon_v{}^c = \epsilon_v - \epsilon_v^e, \tag{2.5}$$

The total volumetric deformation, ϵ_v, can be approximated for the case of the triaxial test, as follows,

$$\epsilon_v = \epsilon_a + 2\epsilon_l, \tag{2.6}$$

where ϵ_a and ϵ_l are the axial and lateral deformations measured directly from the test. ϵ_v^e is the elastic volumetric deformation, given in terms of the Poisson coefficient, v, and Young's modulus, E, and the principal stresses, σ_1 and σ_3, such that,

$$\epsilon_v = \frac{(1-2v)}{E}(\sigma_1 - \sigma_3). \tag{2.7}$$

The point where the volumetric deformation of the fractures starts dilation is considered as the beginning of zone III. This happens because in this zone there is a propagation of pre-existing fractures, which predominate in the direction of the major principal stress [32]. Furthermore, there is the nucleation of new ones due to the shear between their faces and the concentration of stresses around voids, along the surface of the grains and in the contact between them.

Zone III can also be called stable propagation, considering that fractures grow in a limited amount in response to the increase in applied tension, without generating macroscopic fractures. Evidence indicates that acoustic emissions result mainly from shear events, suggesting a predominance of fractures of this type.

In zone IV, the micro-cracks are located in a concrete region or band. Any increase in tension will lead to a permanent degeneration of the material and later to the generation of macroscopic fractures. This zone starts at point c in Figure 2.4, and is called fracture damage stress σ_{cd} (or simply damage stress), whose value is between 70% and 90% of the peak stress, and is generally associated with the point of inversion of volumetric deformations. The value of σ_{cd} depends on the stress confinement and is related to the slip along the fracture faces. It is emphasized that for stresses greater than σ_{cd} and less than the peak stress, it is possible for the material to fail over time, so the fracture damage stress is considered as a material parameter and as the maximum stress for the long term condition. Fractures in zone IV are predominantly in the axial direction, however, inclined or shear fractures present themselves in large numbers, considering that they begin to report, finally generating a macroscopic fracture. The non-homogeneous deformation of the material generates the behavior registered as a mixture between the deformation of the localized zone and part of the elastic recovery of other undamaged regions. There is also a greater departure from linearity, greater rate of lateral deformations and considerable increase in acoustic emissions, until the material reaches its maximum tension, at point d in figure 2.4.

The last zone of Fig. 2.4, shown as zone V, is evaluated with post-peak behavior. It is necessary to evaluate the general representation of the material's behavior, mainly due to the presence of failed zones (macro-fractures) and the discontinuity of the specimen, and the answer depends on the properties of the loading system. The beginning of this step is defined by the peak stress, which is not considered as a material parameter because of its dependence on specimen size, loading rate and load application time. Acoustic emission indicates greater development of inclined fractures by shear in this zone.

2.3 Brittle Rock Materials

Natural solid bodies derived from a pre-determined geological method are determined as rocks. These are constituted by the association of one or more minerals, associated due to the conditions of temperature and pressure existing during their formation. The properties of rock matrices are influenced by the size and spatial arrangement of mineral grains, by the shape, quantity and distribution of discontinuities or voids. This aspect shows that each rock has its particularity, making research about these materials and their properties quite complex and particular.

Rocks can be classified as igneous, sedimentary and metamorphic, Fig. 2.5 presents three examples of rock matrices with different textures for each type.

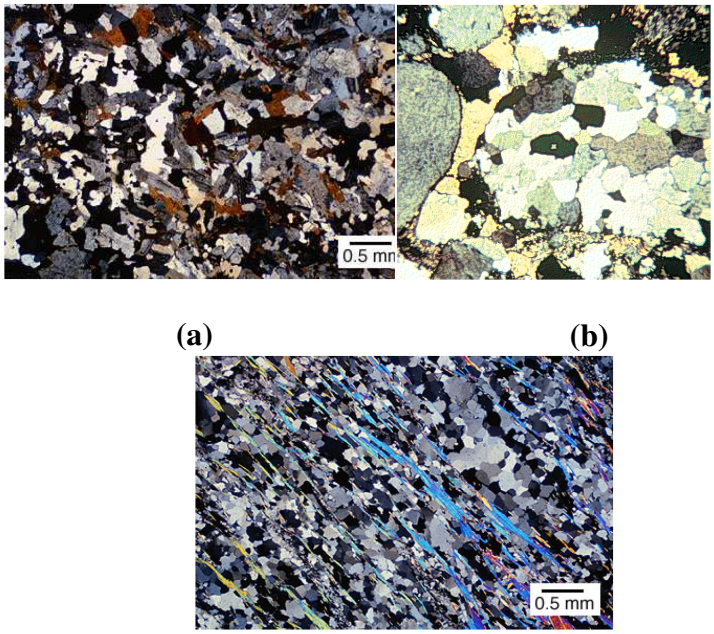

Figure 2.5: Rock micro structures: (a) igneous (b) sedimentary (c) metamorphic. [3]

- Igneous or magmatic rocks are the result of solidification of partially to fully molten rock material (magma), generated within the earth's crust. Example: Granite, syenite, rhyolite, basalt and diorite.
- The metamorphic rocks are the result of pre-existing rocks, which along the geological processes occurred mineralogical, chemical and structural changes in the solid state. Example: Marble, quartzite, schist and corneal.

The main physical characteristics of brittle rocks are: Porosity and Permeability; Strength; and Effects of time on deformations (Fluency/Creep). They are described in the following.

2.3.1 Porosity and Permeability

Porosity is the ratio between the void volume of a rock sample and its total volume. The voids or defects existing in the continuous medium formed by the minerals that constitute the rock matrix represent discontinuities. The porosity value usually shown in percentage, for rocks the average value is 10%, 5% is a low value and the high value is considered to be around 15%. The porosity of igneous rocks is less than 1.5% [37].

The permeability coefficient is measured by the ease of water flow through the continuous medium. Rocks have increasing permeability with cracking and degree of alteration. The decrease in the permeability of rocks can be caused by the increase in compressive stresses, however, after a certain limit, new fractures can start, consequently increasing the permeability.

2.3.2 Strength

The uniaxial study of rocks provides an evaluation of the phenomenon aiming at essential interests in the mechanics of rock materials. The use of simple compression testing is a recurrent practice in determining the mechanical characteristics of rocks. The deformation suffered by the rock, normally, can never be fully recovered if there is a discharge, which shows that the rock has a non-reversible behavior. This characteristic is due to the fact that the cracks present in the rocks close at the beginning of compression, causing a decrease in compressibility. Fig. 2.6 represents the relationship between the vertical stress and the deformation itself [38].

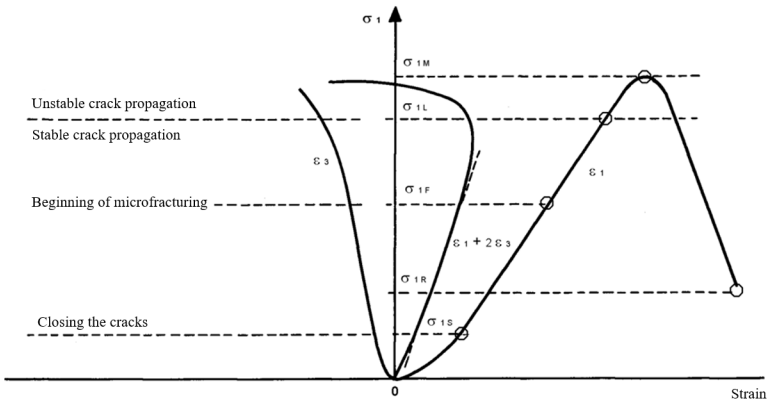

Figure 2.6: Main stages of rock behavior during a compression test. [3]

Analyzing in more detail the main phases of the behavior of a rock during a compression test, we can identify five characteristic values of the vertical stress ($\sigma_1 = \sigma_v$) that limit different types of behavior of the sample:

- σ_{1S} crack closing stress

- σ_{1F} crack initiation stress
- σ_{1L} crack stress limit
- σ_{1M} maximum resistance stress (σ_c)
- σ_1 maximum main stress (σ_v)
- Deformations: $\epsilon_1 = \epsilon_l; \epsilon_3 = \epsilon_t$

2.3.3 Creep

The tendency of a material to deform over time is known as creep. This deformation is due to the effect of the long exposure time to deviating stress levels that are below the ultimate strength of the material. Creep varies depending on material properties, increased stresses or applied overload and time, that is, it is the evolution of plastic deformations over time due to the continuous application of constant deflection stresses [39].

2.4 Numerical modeling

Numerical methods are algorithms capable of formulating and solving mathematical problems using arithmetic operations with less complexity, they can also be called indirect methods. Numerical methods aim to obtain approximate solutions for very complex problems, in this work the finite element method was adopted to solve the problem, seeking the best compression of the phenomenon. However, other numerical methods can also be used to solve this problem, such as:

- Discrete Element Method (DEM): It is associated with molecular dynamics, but differs due to the inclusion of rotational degrees of freedom, contact between discrete elements and complex geometries used to define it.
- Boundary Element Method (BEM): the contour of the analyzed domain is discretized. In other words, it reduces the size of the problem, which makes the implementation easier to generate the geometries and meshes of the analyzed problem.

Engineering problems, for the most part, can be represented through Ordinary Differential Equations (ODEs) and Partial Differential Equations (EDPs). However, the complexity of these questions generates only a portion of problems that can be solved by analytical equations, making it essential to invest in numerical solutions that approach the solution of problems.

According to [40] "in engineering this method was used for the first time in 1960 by Clough in a study on problems of plane elasticity". Initially, the method was implemented

in the study of stresses in aircraft. However, since the work developed by Clough in the 60s, finite element methods have been widely used for linear stress, deflection and vibration analysis in engineering areas, considering that validation of the method's effectiveness has begun.

The development of technology led to an evolution for impact analysis using the finite element method, as computers now have greater operational capacity, consequently reducing analysis time, more complex modeling, with distinct geometries and evaluation of multiple natural elements.

2.4.1 Finite Element Method

The Finite Element Method (FEM) defines the region where the problem is analyzed by forming small elements interconnected with each other. This region is modeled or approximated by a set of predefined discrete elements. Elements can be brought into contact in different configurations and geometries, for this reason it is possible to model analysis geometries with great complexity. Furthermore, this flexibility also provides flexibility in the application of loads and conditions surrounding the phenomenon analyzed.

The problems that can be solved by the finite element method can be classified according to [41, 42] in:

- Balance problems (Static analysis);
- Eigenvalue problems (Dynamic structural analysis);
- Propagation problems (Transient time analysis);

The FEM can be basically summarized in 3 steps: pre-processing, solution and post-processing [43].

- Pre-processing: step that prepares the problem to be solved. The phenomenon is modeled by inducing some operating and boundary conditions such as load. Elements, material properties and simplifications are selected. The simplifications are intended to assist in the analysis and not generate harmful influences on the results. Pre-processing is divided into two steps;
  - Model discretization: After modeling the solids, the model is divided into finite elements, which can be used with geometries that best fit the analyzed model. These elements have nodes, which can be internal or external, so they belong to the interior or on the edges of the element. These elements are interconnected by nodes located on the outline of the elements (node displacements are the basic unknowns quantities of the analyzed problem).

  - Selection of interpolation functions: Once the finite element geometry is defined, there are classically accepted associated interpolation or displacement functions that will represent the exact or real distribution of the displacements. Due to the simplicity of mathematical manipulation, the best interpolation function to be adopted is the polynomial. The three interrelated factors in the selection of the interpolation function are the choice of function type and degree, the type of field variables that describe the model, and the model which must satisfy certain requirements that ensure that the numerical result represents the real solution.Eigenvalue problems (dynamic structural analysis);

- Solution: step dependent on the pre-processing template configuration. In order to solve the differential equations generated in the phenomenon and in the numerical simulation with all the restrictions imposed on the model, a numerical algorithm is carried out that aims to efficiently solve all the variables of the problem. The solution is divided into four steps:

  - Obtaining the elementary stiffness matrix: It is based on the coefficients of the equilibrium equations from the geometric and material properties of an element. It can be obtained by using the principle of minimum potential energy. The stiffness matrix for an element depends on the interpolation function, element geometry, and local material properties selected in preprocessing;
  - Assembly of algebraic equations for the entire domain: Inserts the assembly of the global stiffness matrix for the entire model from the elementary stiffness matrices and the global force vector from the elementary force vectors. The basis for an assembly method is the requirement for nodal interconnects. The offsets within a node must be the same for all adjacent elements;
  - Solutions for the unknown displacements: The equations structured in the previous step are solved for the unknown displacements. For linear problems, the application is more objective using algebra matrix techniques. For nonlinear problems, the solutions require a sequence of steps, involving the modification of the stiffness matrix and/or the force vector;
  - Calculation of deformations and elementary stresses from nodal displacements: Nodal displacements are the variables in study for the solution in several cases. However, other quantities derived from the unknown variables, such as stresses and strains, which must be calculated. Generally speaking, stress and strain are proportional to the derivatives of the displacements.

- Post-Processing: It depends on the need of the user responsible for modeling the problem. However, there is a variety of data that can be analyzed from the data provided, such as:

  - Nodal displacements;

- Geometry deformations;
- Stress gradient according to the chosen strength criteria;
- Temperature gradient;
- Nodal shifts over time;
- Natural frequencies and modes of vibrating the structure.

2.4.2 Non-linear analysis

The non-linear behavior of the phenomena must be taken into account when performing impact simulations. Nonlinearity can occur for several reasons (plasticity, large displacements, large rotations, non-infinitesimal deformations and the effects derived from contact and friction between sheets), and can be reunited into three groups:

- Geometric nonlinearity;
- Material non-linearity;
- Change of status (contact).

The Figure 2.7 represents examples of nonlinearity phenomena. It also presents load/deflection graphs for each example and it is possible to observe the fundamental characteristics of the behavior of structural nonlinearity, due to the change in structural stiffness. Figure 2.7a exemplifies the process of nonlinearity when stapling paper, the metal of the staple always bends in different ways. Figure 2.7b exemplifies the overload of a wooden shelf, as time goes by. The last example shown, in Figure 2.7c, exemplifies a weight added to a car, the surface contact between the tires and the pavement changes according to the added load. The complexity of nonlinearity generates the need for the help of numerical algorithms and high computational resources.

The Nonlinear behavior can be attributed to three main causes [44]:

- Non-linear kinematic behavior due to large displacements, rotations and deformations that occur in the process;
- Non-linear behavior of the constitutive type, due to the inelastic character (plastic, viscoplastic, degradation) which characterizes the material's deformations;
- Non-linear character of the boundary conditions due to the interaction (contact and friction) that takes place between the solids that act in the process along a contact surface that is not initially known and that varies along the process.

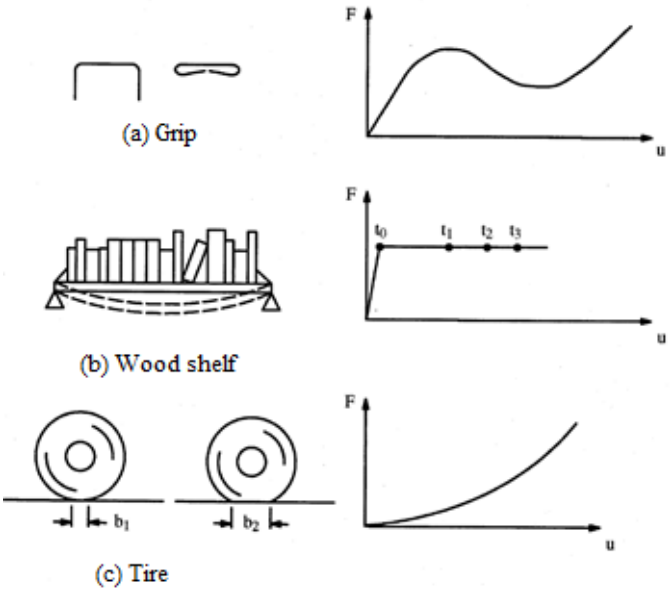

Figure 2.7: Common examples of nonlinear force-displacement behavior. (a) grip, (b) wood shelf, (c) tire. [4]

The equation of motion (2.8) is used to solve dynamic problems [44]:

$$|M|(u) + |C|(u) + |K|(u) = (F^a) \tag{2.8}$$

When:

- |M| is the mass matrix;
- |C| is the damping matrix;
- |K| is the hardness matrix;
- (ü) is the acceleration vector;
- (u) is the velocity vector;
- (F^a) is the vector of applied forces.

For static type problems the acceleration and velocity vectors are null and the (2.8) becomes the (2.9).

$$|K|(u) = (F^a) \tag{2.9}$$

Equations (2.8) and (2.9) become nonlinear when the stiffness matrix |K| is dependent on the displacement u or its derivatives. Therefore, these equations can be represented in equations (2.10) and (2.11).

$$|M|(x"(t)) + |C|(x'(t)) + |K(x(t))|(x(t)) = |F(t)| \tag{2.10}$$

$$|K(x(t))|(x(t)) = |F(t)| \tag{2.11}$$

Mathematically equation (2.8) represents a system of second order linear equations. Usually, the solution to these equations can be obtained through standard procedures for differential equations. However, the system solution becomes extremely complex if the order of the matrices is large. At this point, the alternative procedures for solving the equation can be divided into two groups:

- Method of direct integration in time: in this method, the interests of plasticity and contact are brought together in problems that are solved by means of displacement increments. At each step of the integration in time, the displacement increment that the contact is used for is found and allows us to find the stress and strain values.
- Mode Overlay Method: Used when the basic geometry does not change. In cases involving plasticity and contact, the vibrating modes change during the process, which unable the use of this method.

2.4.3 Johnson-Cook Model

Hooke's Law determines that stress and strain quantities are directly proportional and the elastic behavior of metallic materials is linear. The proportionality constant is given by the modulus of elasticity. Therefore, the elastic field can be determined by only two properties: elastic modulus and Poisson's coefficient.

When analyzing plastic behavior, the constitutive model can be a little bit more challenging. The Hollomon equation helps in the evaluation by proposing a good approximation of the curve representing the plastic region of a graph (stress) x (strain)(ϵ), of a tensile test [45]:

$$\sigma = K\epsilon^n \tag{2.12}$$

Where:

- K is the coefficient of resistance to plastic deformation;
- n is the hardening coefficient.

The (2.12) only considers the plastic field and, therefore, the stresses range from the yield point to the material strength limit. However, the behavior of the material when subjected to high strain rates may differ from that obtained in a conventional tensile test. For this reason, in cases of dynamic compression, for example, it is necessary to use a more elaborate constitutive model.

Johnson-Cook's formulation is the best model to represent the behavior of the material when subjected to high strain rates [24]. It considers, for von Mises stress calculations, the effects of plastic deformation and work hardening (first term), modified by strain rate (second term) and temperature (third term) as independent effects that can be isolated, as represented in the equation (2.13).

$$\sigma = [A + B\epsilon^n][1 + Cln\frac{\epsilon_{eq}}{\epsilon_0}][1 - \frac{T - T_r}{T_m - T_r}]^m \tag{2.13}$$

Where:

- A, B, n, m and C are material constants;
- σ – Equivalent stress;
- A – Initial yield stress;
- B – Plastic resistance constant;
- ϵ – Plastic Deformation ;
- n – Plastic deformation index (hardening index);
- C – Sensitivity coefficient to the strain rate;
- ϵ_{eq} – Equivalent plastic deformation rate;
- ϵ_0 - Reference plastic strain rate;
- T – Body temperature;
- T_r – Reference temperature;
- T_m – Body temperature;
- m – Softening coefficient.

Johnson-Cook's constitutive model constants can present different values for the same material with different heat treatments. This happens because the plastic curve of the material is altered as heat treatments change the crystalline structure.

Ideally, the cross-effect between plastic deformation, deformation rate and temperature should be considered, however, measurements of these values would be difficult to perform. Therefore, the isolated effects (static, dynamic and thermal) are considered through tests under specific conditions [24]. The work carried out by Johson and Cook exposes how the material parameters are obtained by performing a torsion test at a wide range of strain rates, static tensile tests, tensile tests and Hopkinson compression tests at high temperatures [46].

The constants A, B and n can be obtained by a tensile test, assuming that there are no influences from the strain rate and temperature. Coefficient A is the initial true yield stress. The parameter n is the slope of the straight line in the log-log graph of true stress (σv)x true strain (ϵv), represented in Fig. 2.8 and denoted by Eq. (2.14).

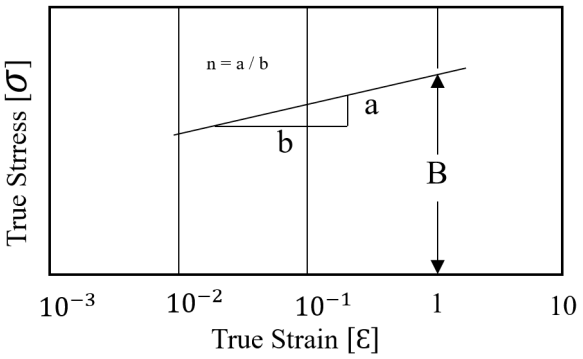

Figure 2.8: Logarithm of true stress, σ, versus logarithm of true strain, ϵ.

$$n = \frac{ln(\sigma_{v2}) - ln(\sigma_{v1})}{n(\epsilon_{v2}) - ln(\epsilon_{v1})} \tag{2.14}$$

The neperian logarithm of parameter B, (ln B), is to find a linear regression on the graph (ln v) x (ln v), as can be seen in Fig. 2.8 and corresponds to the stress value for ln = 1. Therefore, the value of B is then determined by the exponential of the value found for ln B [47].

2.4.4 Damage and Fracture of ductile materials

When performing fracture simulations of ductile materials in the Abaqus® software, it is necessary to define the onset of damage and the behavior of the material in the moments following the fracture (by default the elements that failed are eliminated from the analysis). The damage onset is related to a damage initiation criterion, which can be, for example, a plastic deformation value, where the Abaqus® software considers the global damage $D_{Abq} = 0$. The damage evolution law defines the behavior of the material in the following instants, computes the speed at which the element will lose its capacity to support the load until it is eliminated from the analysis (by default when the global damage $D_{Abq} = 1$, which implies zero stress).

The law of damage evolution can be defined in terms of a displacement, u^{-pl}, for example. An internal Abaqus® math then computes the stress drop across the element according to this law. The rigidity reduction of the element can occur progressively for values of u^{-pl} different from zero or instantaneously equal to zero [5].

Fig. 2.9 represents the stress-strain curve for the behavior of a ductile material that experiences damage (solid line) and the behavior of the material if there was no damage (dashed

line), stress given by σ. Analyzing the graph, σ_0 is the yield stress, ${\epsilon_0}^{-pl}$ is the equivalent plastic strain at the start of the damage (σ_{y0} is the corresponding stress), ${\epsilon_f}^{-pl}$ is the plastic strain at the fracture (zero stress).

Abaqus® software refers to stiffness reduction as degradation of the material stiffness. It is expressed as an SDEG (Scalar stiffness degradation variable), which ranges from 0 to 1. The value 0 means that the element did not meet any active damage criteria in the analysis. When the element reaches a criterion and proceeds with loading, this index can assume the maximum value of the analysis, 1, and the stress in the element becomes null and it is no longer considered in the software's calculations. The material elasticity reduction is calculated as $\sigma = (1 - D_{Abq})E$ while the stress drop is given by $\sigma = (1 - D_{Abq})\sigma'$.

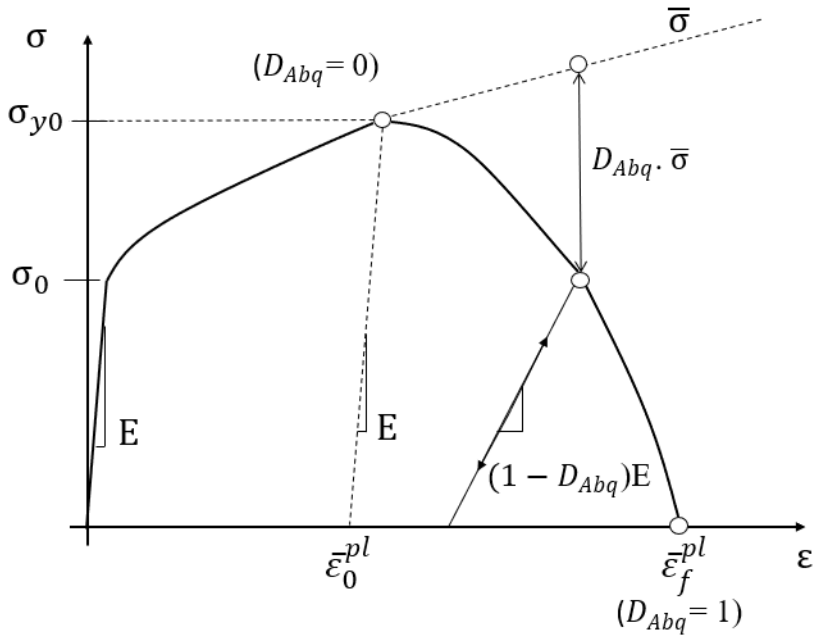

Figure 2.9: Example of a stress-strain curve including global damage, D_{Abq} [5].

The onset of damage can be considered by the onset of tightening, using a tensile test, for example. Therefore, the evolution law must have the value calibrated in order to represent the behavior of the material in the final moments of the test. The damage evolution law, associated by the corresponding damage initiation criterion, will determine the behavior of the curve between the points ${\epsilon_0}^{-pl}$ and ${\epsilon_f}^{-pl}$. With the possible elimination of elements during the analysis, faces of internal elements may be exposed, as in the case of erosion simulations. It is therefore recommended to define a contact surface based on nodes.

A widely used criterion in machining analysis, ballistics and dynamic compressions in general is Johnson-Cook's failure model. This model considers that the plastic deformation at damage onset, ${\epsilon_f}^{-pl}$, is a function of the triaxial state of stresses (η) the strain rate ϵ^{-pl}, the temperature (T) and the failure parameters of the material. The first term in equation (2.15) refers to the plastic deformation at the beginning of the damage, and is influenced by the

deformation rate (second term) and temperature (third term).

$$\epsilon^{-pl} = [d_1 + d_2 exp(d_3\eta)][1 + d_4 ln\frac{\epsilon}{\epsilon_0}][1 + d_s\frac{T - T_r}{T_m - T_r}] \tag{2.15}$$

Where:

- η is computed as the ratio between p (hydrostatic stress) and q (von Mises equivalent stress);
- d_1, d_2, d_3, d_4 e d_5 are damage constants and ϵ_0 the reference strain rate, which must be informed [24].

The model assumes that internal damage accumulates linearly. This internal damage starts with the plastic phase, the software computes the ratio between the current plastic deformation and the plastic deformation chosen for the damage onset. This internal damage can be expressed by an index (D_{JC}) ranging from 0 to 1, as can be seen in equation (2.16), referred to in the analysis as index of Johnson-Cook's damage initiation criterion ("Johnson-Cook damage initiation criterion" - JCCRT).

$$D_{JC} = \Sigma\frac{{\epsilon_i}^{pl}}{{\epsilon_f}^{-pl}} \tag{2.16}$$

Parameters d_1, d_2, d_3, d_4 and d_5 of the material can be obtained by performing experimental tests. [46] [48] [49]

The onset of damage could be interpreted as the onset of shrinkage in a tensile test, or any other plastic deformation that would render the component unusable according to a design criterion. The harm evolution law is more related to the elimination of the element of analysis. Thus, if one only wants to know if an element has reached a failure criterion or not, this can be verified by the DJC, for example, for Johnson-Cook, without the need to define a law of evolution.

2.4.5 Concrete Damage Plasticity Model

In order to represent the non-linear behavior of concrete, including failure in compression and in tension, Lubliner [50] proposed a model based on the Theory of Plasticity and also on the Mechanics of Continuous Damage. The damage concepts are incorporated in a plastic model, that is, the concept of effective stresses from Damage Mechanics is used to represent the loss of stiffness [51]. In this model, concrete and other materials are considered as cohesive materials with friction, from which an eventual loss of stiffness (damage) can be related to a loss of cohesion.

The Abaqus® software provides three constitutive concrete models for concrete modeling under low pressure confinement (values four to five times smaller than the ultimate

compressive stress at axial loading):

- Concrete Smeared Cracking (Abaqus/Standard);
- Brittle Cracking (Abaqus/Explicit);
- Concrete Damage Plasticity (CDP)(Abaqus/Standard e Abaqus/Explicit).

The most complex concrete model associated with Abaqus® is the CDP, which can be used in any loading regime, however, the model requires several parameters and its calibration can be reasonably challenging. According to [52] [53], the CDP model is a modification of the Drucker-Prager resistance hypothesis and in recent years it has been improved by [54] and by [51], for having modeling of concrete and other quasi-brittle materials in all types of structure, the concepts of isotropic elastic damage and isotropic tension and plastic compression are used to represent the inelastic behavior of concrete, in addition to the fact that the model requires the elastic behavior of the material is considered to be isotropic and linear.

In concrete and other quasi-brittle materials the capture of irreversible damage effects related to failure mechanisms are associated with the following Macroscopic properties [7]:

- Different yield strengths in tensile and compression, the initial yield strength to compression being about 10 or more times greater than the initial yield strength to tension;
- Relaxation behavior in tension opposite to initial work hardening followed by relaxation in compression;
- Different degradation of elastic stiffness in traction and compression;
- Stiffness recovery effects under cyclic behavior;
- Sensitivity rate, especially an increase in peak strength with strain rate.

The total strain rate ε' is decomposed according to Eq. (2.17).

$$\varepsilon' = \varepsilon'^{el} + \varepsilon'^{pl} \tag{2.17}$$

Where:

- ε'^{el} is the elastic strain rate;
- ε'^{pl} is the plastic strain rate.

The stress-strain relationships are governed by elasticity and scale damage, as in the Eq. (2.18). The damage associated with concrete failure mechanisms (cracking or crushing) results in a reduction in elastic stiffness.

$$\sigma = (1-d){D_0}^{el} : \varepsilon - \varepsilon'^{pl} = D^{el} : \varepsilon - \varepsilon'^{pl} \tag{2.18}$$

Where:

- ${D_0}^{el}$ is the elastic stiffness of the material (no damage);
- $(1-d){D_0}^{el}$ is the damaged elastic stiffness;
- d is the scalar stiffness degradation variable that has values from zero (materials without damage) to one, where the material is considered to have had its stiffness totally deteriorated.

The effective stress,σ', presented in Eq. (2.19), is related to the Cauchy stress,σ, through Eq. (2.20). The stiffness degradation response presented in Eq. (2.20) is of best interest for numerical simulation. Since in the absence of damage $d = 0$, the effective stress equals the Cauchy stress. However, when damage occurs, the effective stress is more representative than the Cauchy stress due to the area of effective stress that is resisting extreme loads. The damage variable d is controlled by a set of effective stress and work hardening variables, $d = d(\sigma', \varepsilon'^{pl})$.

$$\sigma = {D_0}^{el} : \varepsilon - \varepsilon'^{pl} = D^{el} \tag{2.19}$$

$$\sigma = (1-d)\sigma' \tag{2.20}$$

Two hardening variables related to tensile and compression states are respectively characterized by ${\epsilon_t}'^{pl}$ and ${\epsilon_c}'^{pl}$ correspond to the equivalent plastic strain. The evolution of these variables is given according to Eq. (2.21) and may represent, in addition to the tensile fracture and crushing process, through the control of the evolution of the flow surface and degradation of elastic stiffness, the energy dissipated in fracture for generate microcracks.

$$[\frac{{\epsilon_t}^{pl}}{{\epsilon_c}^{pl}}], \epsilon' = h(\sigma', {\epsilon_t}'^{pl}).\epsilon'^{pl} \tag{2.21}$$

The flow function represents a surface in the effective stress space that determines the state of failure or damage. For the inviscid model of damage and plasticity, we have Eq. (2.22), which will be better detailed throughout the text. The plastic flux is governed according to the flux rule in Eq. (2.23) by a potential flux $\mathbf{G}$. In the CDP model the potential flux uses non-associated plasticity requiring the solution of non-symmetric equations.

$$F(\sigma', \epsilon'^{pl}) \leq 0 \tag{2.22}$$

$$\gamma\epsilon'^{pl} = \gamma'\frac{dG(\sigma')}{d\sigma'} \tag{2.23}$$

Where γ' is a non-negative plastic multiplier. The elastoplastic response of the concrete plasticity and damage model is described in terms of the effective stresses and work

hardening variables given in Eq. (2.28). In this equation, γ' e F are governed by the Kuhn–Karush–Tucker conditions as shown in Eq. (2.25).

$$\sigma' = {D_0}^{el} : (\varepsilon - \varepsilon^{pl})\epsilon\sigma | F(\sigma, \varepsilon - \varepsilon^{pl}) \leq 0 \tag{2.24}$$

$$\varepsilon^{pl} = h(\sigma, \varepsilon^{pl}).\varepsilon^{pl} \tag{2.25}$$

$$\varepsilon^{pl} = \gamma' \frac{dG(\sigma')}{d\sigma'} \tag{2.26}$$

$$\gamma' F = 0; \gamma' \geq F \leq 0 \tag{2.27}$$

Stiffness degradation and damage are formulated by considering uniaxial conditions first and then extending to multiaxial conditions. The stress vs strain curves are converted into stress vs plastic strain curves as shown in Eq. (2.28).

$$\sigma_t = \sigma_t({\varepsilon_t}^{pl}, {\varepsilon_t}'^{pl}, \theta, f_i) \tag{2.28}$$

$$\sigma_c = \sigma_c({\varepsilon_c}^{pl}, {\varepsilon_c}'^{pl}, \theta, f_i) \tag{2.29}$$

where:

- ${\varepsilon_t}^{pl}$ and ${\varepsilon_c}^{pl}$ are equivalent plastic deformation rates and under uniaxial conditions are given in Eq. (2.30).

$${\varepsilon_t}^{pl} = {\varepsilon_{l1}}^{pl} \tag{2.30}$$

$${\varepsilon_c}^{pl} = -{\varepsilon_{l1}}^{pl} \tag{2.31}$$

- ${\varepsilon_t}^{pl}$ and ${\varepsilon_c}^{pl}$ are equivalent plastic deformations, presented in Eq. (2.32).

$${\varepsilon_t}^{pl} = \int {\varepsilon_t}'^{pl} dt \tag{2.32}$$

$${\varepsilon_c}^{pl} = \int {\varepsilon_c}'^{pl} dt \tag{2.33}$$

- θ is the temperature;

- f_i are other predefined variable fields.

Fig. 2.10 show the response of concrete to uniaxial loading conditions, in which it can be observed that the degradation of elastic stiffness is different between the tensile and compression behavior. The degraded concrete response is characterized by two independent variables of uniaxial damage, d_t e d_c, which are functions of plastic deformations, temperature and other variable fields. These damage variables are presented in Eq. (2.34) and assume values between zero and one, in which the value of zero means that the material has no damage and the value of one means total loss of stiffness and total damage to the material.

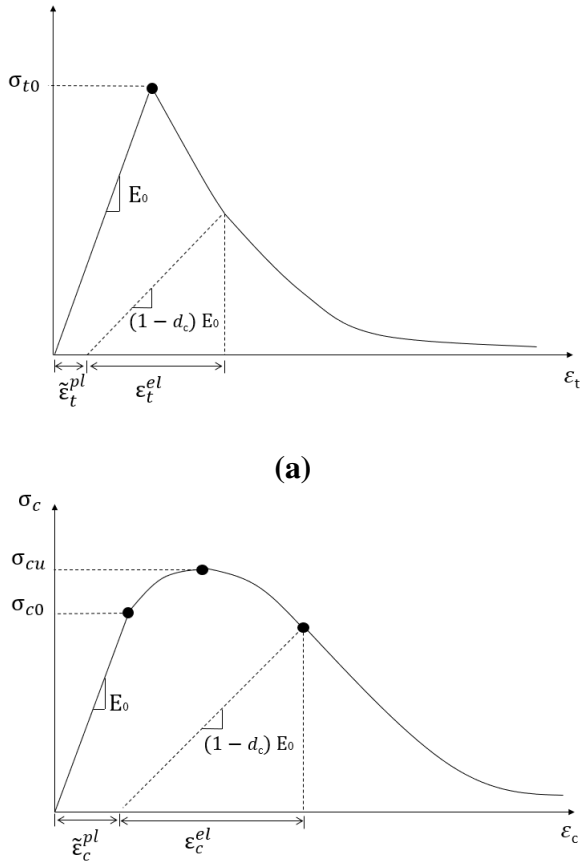

Figure 2.10: Stress-strain behavior of concrete in uniaxial condition. a) Tensile, b) Compression. [6]

$$d_t = d_t(\varepsilon_t{}^{\prime pl}, \theta, f_i), (0 \leq d_t \geq 1). \tag{2.34}$$

$$d_c = d_c(\varepsilon_c{}^{\prime pl}, \theta, f_i), (0 \leq d_c \geq 1). \tag{2.35}$$

The stress-strain relationships are represented in Eq. (2.36), where E_0 is the initial elastic stiffness of the material. The crack propagates in a direction perpendicular to the direction of

pull. Nucleation and propagation cause a reduction in the available load-bearing area, which leads to an increase in effective stresses. The effect is less pronounced under compressive loading, as the cracks propagate parallel to the loading direction. However, after a significant amount of crushing, the available load-bearing area is significantly reduced. The effective cohesion stresses are shown in Eq. (2.40) and determine the size of the flow surface.

$$\sigma_t = (1 - d_t)E_0(\varepsilon_t, {\varepsilon_t}'^{pl}) \tag{2.36}$$

$$\sigma_t = (1 - d_c)E_0(\varepsilon_c, {\varepsilon_c}'^{pl}) \tag{2.37}$$

$$\sigma'_t = \frac{\sigma_t}{(1 - d_t)}E_0(\varepsilon_t, {\varepsilon_t}'^{pl}) \tag{2.38}$$

$$\sigma'_c = \frac{\sigma_t}{(1 - d_c)}E_0(\varepsilon_c, {\varepsilon_c}'^{pl}) \tag{2.39}$$

In order to use the uniaxial condition equations for the multiaxial general case, the equivalent plastic strain rates are given according to Eq. (2.40) [51].

$${\varepsilon_t}^{pl} = r(\theta){\varepsilon_{max}}^{pl}. \tag{2.40}$$

$${\varepsilon_c}^{pl} = (1 - r(\theta)){\varepsilon_{min}}^{pl}, \tag{2.41}$$

Where ${\varepsilon_{max}}^{pl}$ and ${\varepsilon_{min}}^{pl}$ are the maximum and minimum eigenvalues of the plastic formation rate tensorε^{pl} . The term $r(\theta)$ given by Eq. (2.42) is unity if all principal stresses $\theta''_i (i = 1, 2, 3)$ are positive and equal to zero if they are negative.

$$r(\theta'') = \frac{\Sigma(\sigma_i)}{\Sigma|\sigma_i|}; 0 \leq r(\theta'') \leq 1 \tag{2.42}$$

The term $<.>$ is the MacAulay function defined by $<x> = 1/2(|x|+x)$. The eigenvalues of the plastic formation rate tensor $\varepsilon_i (i = 1, 2, 3)$ ordered so that the conditions for the general case of multiaxial stress it will be expressed in the matrix form given in Eq. (2.43).

$$\varepsilon^{pl} = [\frac{{\varepsilon_t}^{pl}}{{\varepsilon_c}^{pl}}] = h'(\theta', {\varepsilon_c}^{pl}).{\varepsilon_c}^{pl}, \tag{2.43}$$

Where $h'(\theta', {\varepsilon_c}^{pl})$ and ${\varepsilon_c}^{pl}$ are presented in Eq's (2.44) and (2.45).

$$h'(\theta', \varepsilon_c{}^{pl}) = \begin{bmatrix} r\theta'' & 0 & 0 \\ 0 & 0 & -(1 - r\theta'') \end{bmatrix} \tag{2.44}$$

$$\varepsilon^{pl} = \begin{bmatrix} \varepsilon_1 \\ \varepsilon_2 \\ \varepsilon_3 \end{bmatrix} \tag{2.45}$$

The definition of the stiffness degradation scalar variable must be consistent with the monotonic axial responses (d_t and d_c) and are able to capture the complexity associated with degradation mechanisms under cyclic loading [7]. In the case of multiaxial stresses, the generalization presented in Eq. (2.46) is assumed, with s_t and s_c given as a function of $r(\theta'')$ presented in Eq. (2.47).

$$(1 - d) = (1 - s_t d_t)(1 - s_c d_c); 0 \leq s_t s_c \leq 1 \tag{2.46}$$

$$s_t = 1 - w_t r(\theta''); 0 \leq w_t \leq 1 \tag{2.47}$$

$$s_c = 1 - w_c r(\theta''); 0 \leq w_c \leq 1 \tag{2.48}$$

The compressive stiffness considered in the CDP model is recovered with fracture closure due to a change in load from traction to compression $(w_c = 1)$. As for tensile stiffness, stiffness recovery in a change from compression to traction load $(w_t = 0)$ is not considered. The CDP model uses a conformal flow function [54] and incorporates the modifications proposed by [51] to take into account different evolutions of tensile and/or compression strength. The flow function in terms of effective stresses is given by Eq. (2.49), where α and γ are material dimensionless constants. The effective standing pressure, the effective equivalent von Mises stress and the deviating part of the tensor effective stress σ' are given, respectively presented in Eq's (2.50), (2.51) and (2.52).

$$F(\sigma', \varepsilon^{pl}) = (\frac{1}{1 - \alpha})(q' - 3\alpha p' + \beta(\varepsilon^{pl}) < \sigma_{max} >) - \sigma_c(\varepsilon^{pl}) \leq 0 \tag{2.49}$$

$$p' = -\frac{1}{3}\sigma : I \tag{2.50}$$

$$q' = \sqrt{\frac{3}{2} S : S} \tag{2.51}$$

$$S = pl + \sigma \tag{2.52}$$

The term σ_{max} is, algebraically, the maximum value of σ and if $\sigma_{max} = 0$ the Eq. (2.49) is reduced to the Drucker-Prager flow condition $\beta(\varepsilon^{pl})$ is presented in Eq. (2.53) and the coefficient α can be determined from the equibiaxial (σ_{b0}) and uniaxial (σ_{c0}) compressive flow stresses is presented in Eq. (2.54).

$$\beta(\varepsilon^{pl}) = \frac{\sigma_c(\varepsilon_c{}^{pl})}{\sigma_t(\varepsilon_t{}^{pl})}(1-\alpha) - (1+\alpha) \tag{2.53}$$

$$\alpha = \frac{\sigma_{b0} - \sigma_{c0}}{2\sigma_{b0} - \sigma_{c0}}; 0,08 \leq \alpha \leq 0,12 \tag{2.54}$$

$$1,10 \leq \frac{\sigma_{b0}}{\sigma_{c0}} \leq 1,16 \tag{2.55}$$

Comparing the flow conditions along the traction and compression meridians and integrating the flow function, presented in Eq. (2.49), it is possible to determine the material coefficient γ, only in the case of triaxial compression, when $\sigma_{max} < 0$. Regarding the meridians, the following is defined as the traction meridian (TM) is the locus of stress states satisfying the condition $\sigma_{max} = \sigma_1 > \sigma_2 = \sigma_3$ the eigenvalues of the effective stress tensor; the compression meridian (CM) is the locus of stress states that satisfy $\sigma_{max} = \sigma_1 = \sigma_2 > \sigma_3$".

The term σ_{max} along the tension and compression meridians is presented in Eq. (2.56), and with $\sigma_{max} < 0$, the corresponding flow function is presented in Eq. (2.58).

$$(\sigma_m ax)_{TM} = \frac{2}{3}q' - p' \tag{2.56}$$

$$(\sigma_m ax)_{CM} = \frac{1}{3}q' - p' \tag{2.57}$$

$$(\frac{2}{3}\gamma + 1)q - (\gamma + 3\alpha)p = (1-\alpha)\sigma_c(TM) \tag{2.58}$$

$$(\frac{1}{3}\gamma + 1)q - (\gamma + 3\alpha)p = (1-\alpha)\sigma_c(CM) \tag{2.59}$$

Considering the $K_c = \frac{q_{TM}}{q_{CM}}$ for any value of the hydrostatic pressure p with $\sigma < 0$, we obtain Eq. (2.60). In this equation, taking into account experimental evidence, it is noted that K_c is constant, so γ can be evaluated according to Eq. (2.61). The K_c ratio is always greater than 0.5. When the value of the ratio reaches 1,0 the fault surface of the deviating cross section becomes a circle, as in the classical resistance hypothesis of Drucker-Prager [52].

The typical value for concrete is $K_c = 2/3$ giving $\gamma = 3$. Based on the modifications of the works of Lubliner and Lee and Fenves, the fault surface in the deviating cross section does not need to be circular and is governed by the parameter K_c [54]. The parameter K_c is understood as the ratio of the distances between the hydrostatic axis and, respectively, the compression meridian (CM) and the traction meridian (TM) in the diverter cross section.

$$K_c = \frac{\gamma = 3}{2\gamma + 3} \tag{2.60}$$

$$\gamma = \frac{3(1 - K_c)}{2K_c - 1} \tag{2.61}$$

Considering $\sigma_{max} > 0$ the flow conditions along the traction and compression meridians reduce to Eq. (2.62). Knowing that $K_c = \frac{q_{TM}}{q_{CM}}$ for any value of hydrostatic pressure p with $\sigma_{max} < 0$, one obtains similarly K_c in Eq. (2.64). The flow surfaces referring to the deviatoric plane and for flat stress are given respectively in Fig. 2.11 and Fig. 2.12.

$$(\frac{2}{3}\beta + 1)q - (\beta + 3\alpha)p = (1 - \alpha)\sigma_c(TM) \tag{2.62}$$

$$(\frac{1}{3}\beta + 1)q - (\beta + 3\alpha)p = (1 - \alpha)\sigma_c(CM) \tag{2.63}$$

$$K_c = \frac{\beta + 3}{2\beta + 3} \tag{2.64}$$

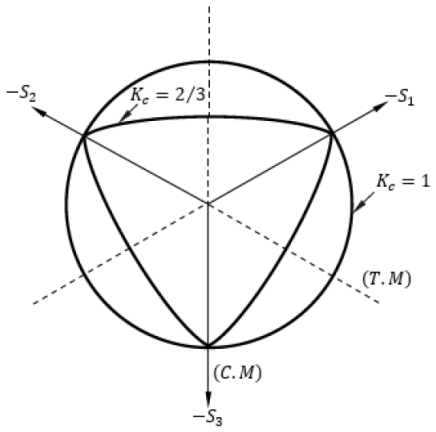

Figure 2.11: Flow surface in the deviatoric plane, corresponding to different Kc values for the CDP model [7].

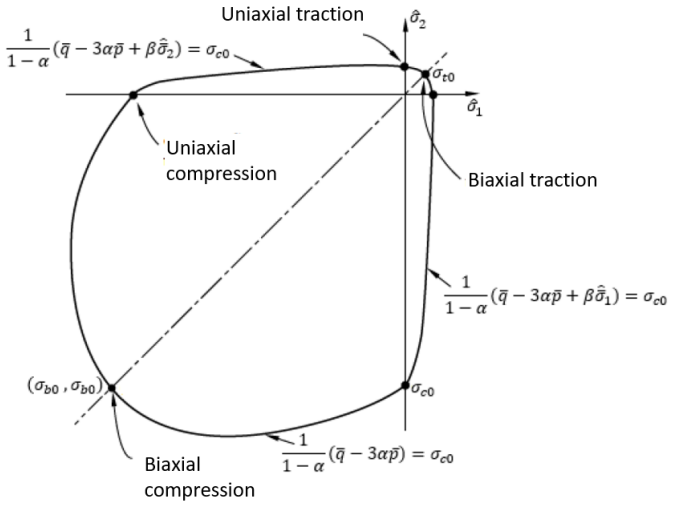

Figure 2.12: Flow surface in flat stress [7].

Chapter 3

IMPLEMENTATION

This chapter presents the Problem setup, Material properties, Assembly and Simulation steps, Interactions and Loads, Mesh and Output variables.

3.1 Problem setup

The numerical impact analysis is performed in the finite element software Abaqus®. This software is licensed by Dassault Systèmes and is recurrently used by engineers to solve industrial problems. Herein, the problem is addressed as a 3D model of a projectile impact (different shapes and/or orientations) against a flat counterpart. Both bodies are defined as deformable solids. The total of seven configurations are shown in the Fig. 3.1.

A naming scheme for each impact conditions is proposed: it includes the type of material analyzed, the geometry and impact velocity. The concrete, arenite and granite are denoted by CON, ARE and GRA, respectively. The sphere, oval and sharp particles are denoted by SPH, OVA and SRP. As an example: CON-SPH75-10 is the acronym of a concrete sphere of 7.5mm at 10m/s.

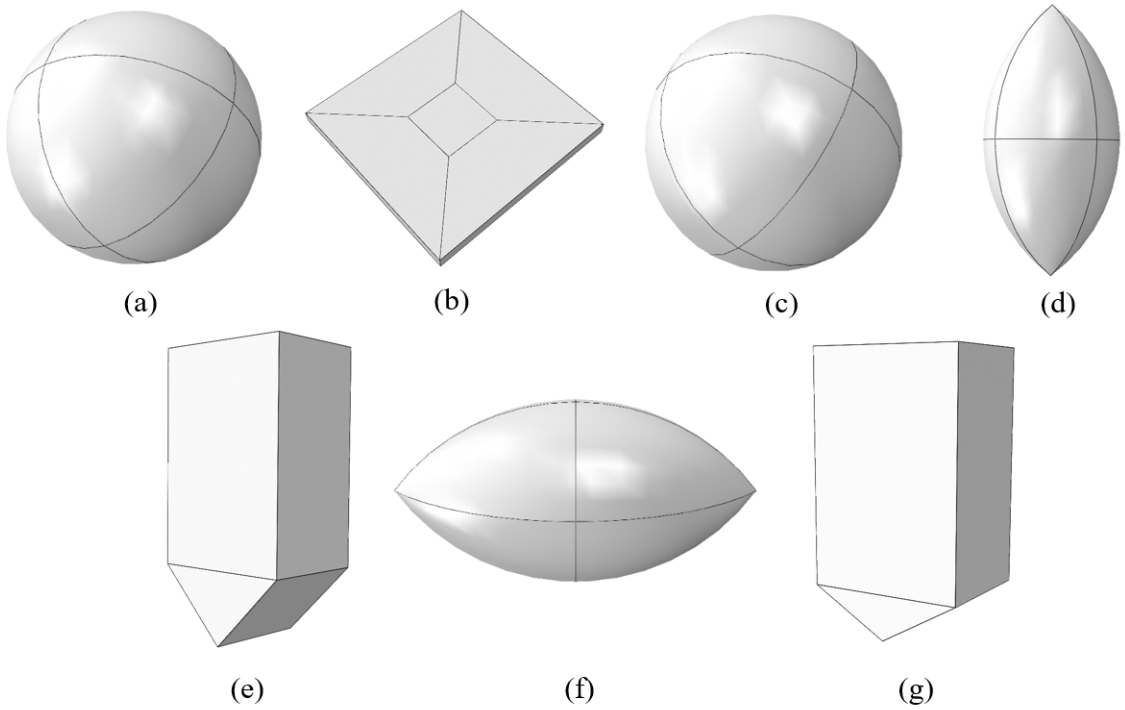

Figure 3.1: Analyzed geometries: (a) Sphere 7.5mm diameter (b) Flat counterpart (100mm x 100mm x 6.35mm). (c) Sphere 15mm diameter. (d) Oval 7.5mm by 15mm. (e) Sharp 45° (square section 10mm wide, 26mm long and a sharp corner centered at 45°). (f) Oval 15mm by 7.5mm. (g) Sharp 30° (10mm wide square section, 22mm long and a sharp corner centered at 30°).

3.2 Material properties

This section describes the mechanical properties with the necessary data for the implementation of the Johnson-Cook models for the metallic flat counterpart and the plastic model of the concrete projectiles. This information is used as input for computational simulation using Abaqus® finite element software.

3.2.1 Counterpart properties

The material properties used in the analyzes are shown in Tables 3.1 and 3.2. To obtain a model relevant to the behavior of the material, Johnson-Cook's formulation was used.

Table 3.1: AISI 1020 steel properties.

Material	Density	Elastic Modulus	Poisson's Coefficient	β	Specific Heat
Steel	7830	210	0.3	0.9	477

Table 3.2: Plasticity Model Parameters.

A	B	n	m	Tm	Tr	c	ϵ
324	114	0.42	0	1793	298	0.008	1

The damage criterion used was the initiation criterion and damage evolution law for ductile materials. Johnson-Cook's damage criterion was used considering the influence of strain rate and temperature. Damage parameters are in Table 3.3.

Table 3.3: Johnson-Cook Damage Criteria Parameters.

Material	d1	d2	d3	d4	d5	$\epsilon[s1]$
Steel	-0.77	1.45	0.47	0.001	0	1

3.2.2 Projectile properties

The criterion used for the projectiles was the use of the Concrete Damaged Plasticity (CDP), since it is a model based on plasticity and material damage, being used to model concrete and other fragile materials. The properties used in the analysis are shown in Tables 3.4-3.6.

Table 3.4: Concrete constitutive parameters.

Dilatation Angle	e eccentricity	F	Kc	Young Module [MPa]	Poisson's Coefficient	Density [kg/m³]
36º	0.1	1.16	0.67	33000	0.18	2400
Compressive Behavior						
Stress	Inelastic Deformation	Stress	Inelastic Deformation	Stress Stress	Inelastic Deformation	
9.0	0	25.17	0.0008	24.26	0.0018	
15.95	0.0001	26.81	0.0010	22.26	0.0021	
21.54	0.0005	26.85	0.0013	20.59	0.0024	
Traction Behavior						
Stress				Fracture Deformation		
3.67				0		
2.82				0.0001		
2.41				0.00022		
2.16				0.00033		

Table 3.5: Granite constitutive parameters.

Dilatation Angle	**e**	F	Kc	Young Module [MPa]	Poisson's Coefficient	Density [kg/m³]
10º	0.1	1.12	0.66	56200	0.16	2650
Compressive Behavior						
Stress	Inelastic Deformation	Stress	Inelastic Deformation	Stress	Inelastic Deformation	
191.51	0	25.17	0.0075	38.49	0.0123	
181.53	0.0052	85.93	0.0094	18.52	0.0136	
146.30	0.0063	65.78	0.0108	-	-	
Traction Behavior						
Stress				Fracture Deformation		
10.00				0		
6.67				0.0004807		
3.75				0.0011072		
1.67				0.0020679		

Table 3.6: Arenite constitutive parameters.

Dilatation Angle	e	F	Kc	Young Module [MPa]	Poisson's Coefficient	Density [kg/m³]
20º	1.12	0.66	28000	0.2	2560	
Compressive Behavior						
Stress	Inelastic Deformation	Stress	Inelastic Deformation	Stress	Inelastic Deformation	
125.87	0	116.09	0.0053	40.48	0.0105	
120.60	0.003	111.10	0.0060	26.26	0.0122	
120.07	0.004	60.66	0.0088	-	-	
Traction Behavior						
Stress				Fracture Deformation		
6.20				0		
4.13				0.00105		
2.33				0.00226		
1.03				0.00415		

Each solid modeled and used in the simulation was assigned a material property. In this work, the material used in the projectiles were concrete, granite and arenite, while the counterpart is modeled as steel. Once materials are applied to solids, sections are created to meet part specifications. Since each part is made of one type of material, a section is created for each part and the correct material property is associated with its respective section.

3.3 Assembly and Simulation steps

In the assembly, instances of the parts are created and positioned relative to each other in a global coordinate system, as shown in Fig. 3.2, so that the bodies are approximately 2mm apart. Knowing that Abaqus® uses the time period value and the increment values to determine the duration of an increment, it was determined that for the speeds of 10, 20, 40 and 60m/s the time period values would be 1, 0.5, 0.25 and 0.16ms, respectively, so that all simulations have 100 frames.

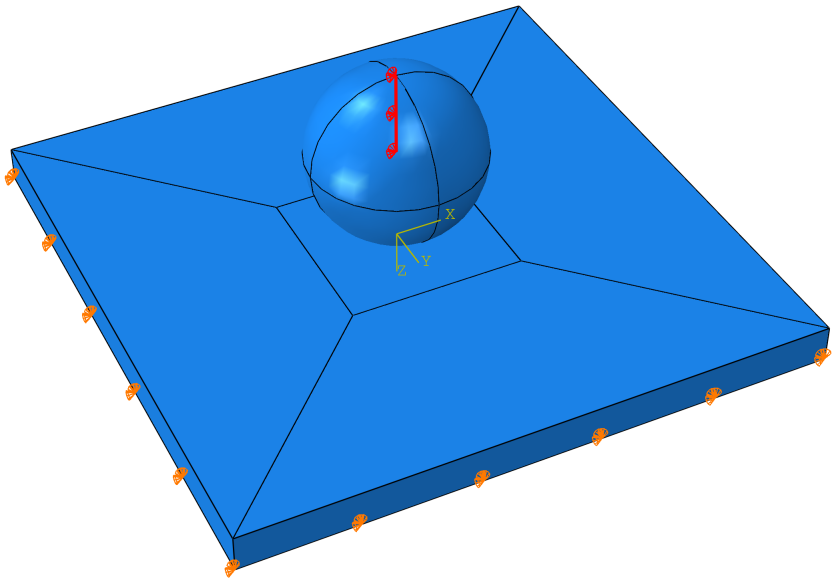

Figure 3.2: Assembly configuration and boundary conditions.

The boundary conditions were defined in order to obtain the best results. In the flat counterpart, restrictions were implemented in the three directions applied at the ends. In the projectile, restrictions were implemented on the X and Y axis, making the projectile only move in the Z direction, this restriction was implemented at the center of mass and at the end.

The simulation was carried out in two stages, thus defining the impact between the projectile and the flat counterpart. In the initial stage, the contact interaction between the projectile and the flat counterpart was defined, as well as the definition of the impact velocity. The second step establishes the boundary conditions that the specimen is completely contained in its base, with the projectile not moving in other directions except the impact one, and the flat counterpart is with displacement restriction in the three directions.

3.4 Interactions and Loads

The interaction module is used to define the impact interactions, contact between bodies and coupling constraints in the model. Once the contact interaction type is determined, the

contact formulation is defined and will result in how the surfaces interact based on the master and slave definitions, contact discretization and tracking approach. Since the flat counterpart is more rigid and may have a thicker mesh, its contact surface is defined as the master, while the projectile surface acts as a slave to the surface. Contact discretization is defined as surface-to-surface and is responsible for how constraints are applied to interaction surfaces. When working with the mechanics of contact, the relationship that establishes a rule for the surface movement must be defined. The chosen contact constraint application method establishes how the contact constraints are resolved in the analysis. Two main approaches can be taken which are the penalty multiplier and the Lagrange methods.

The load and limit conditions are applied to the model and, since they are step-dependent objects, it is necessary to specify in which steps they are active, as described in the Steps module section. The initial position of the projectile is defined allowing its movement only in the vertical direction. This is achieved by restricting projectile movement in other directions. The position of the flat counterpart is defined by not allowing movement in three directions.

3.5 Mesh

For efficiency purposes, a contact region in the projectile and in the counterpart was defined to allow the assignment of dissimilar meshes to the same body without the need for a transition zone between them, as shown in Fig. 3.3.

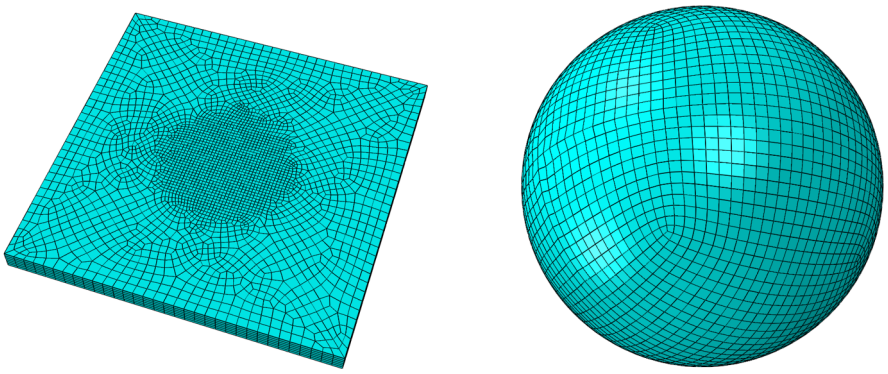

(a) (b)

Figure 3.3: Discretized representations. (a) flat counterpart, (b) sphere.

As you can see in Fig. 3.3, the counterpart contact zone has a finer mesh than the other regions, considering an approximate element size of 1mm, and the projectile's mesh has an approximate element size equal to 0.5mm and the type of elements used for both geometries is the C3D8R: In 8-node linear brick, reduced integration, hourglass control. The contact is enforced via the surface-to-surface segmentation method.

3.6 Output variables

In order to consolidate the numerical implementation methodology for the impact analysis in a nonlinear regime of brittle particles, the output variables analyzed are:

- CPRESS: contact pressure;
- DAMAGEC: compressive damage;
- PEEQ: equivalent plastic deformation;
- S,MISES: von Mises equivalent stress.

After the simulation of the impact of six brittle materials onto the ductile surface, it was possible to observe the behavior of the solids at the velocities 10, 20, 40 and 60m/s. The results are presented and discussed in Chapter 4. This study accurately analyzes failure modes due to transient dynamic impact loads. Commercial finite element software makes it possible to establish several parameters for the analysis control during non-linear analysis, which automatically active in order to guarantee that the load increment variation is neither too large nor too conservative.

Chapter 4

RESULTS AND DISCUSSIONS

This chapter presents a Qualitative analysis and a Quantitative analysis of the numerical simulations results.

The results will be presented in two parts, where initially the a qualitative evaluation of the results will be carried out, in which the impact images of the geometries and how much the projectiles were damaged will be presented. Finally, important aspects of the analysis of geometries are discussed, comparing which is the most harmful geometry for the flat counterpart. Then, quantitative analysis of the results will be evaluated, through the graphs obtained from the impact between the projectile and the flat counterpart. The graphs presented will show the behavior of six geometries with non-linear properties (concrete, granite and arenite), varying the impact velocity and the influence of these geometries on the metallic flat counterpart.

4.1 Qualitative analysis

Collision processes are applications of the laws of energy conservation and linear momentum. Collisions can be classified according to conservation, or not, of kinetic energy. As conditions analyzed in this work, they are inelastic collisions, considering that the kinetic energy is not conserved, that is, the final kinetic energy is less than its initial value and this difference is converted into deformation energy, so far allow the material to break and initiate damage to the projectile.

The tables below show the damage percentages of concrete, arenite and granite projectiles during impact on the metallic flat counterpart. The figures below show the main final damage outputs in compression and the maximum equivalent von Mises stress related to the impacts performed in the Abaqus® CAE software, varying the speed from 10 to 60m/s, evaluating the damage of the material after the impact of according to the material used in the projectile. During the evaluation of images and data, it will be possible to understand the non-linear behavior of the materials analyzed, and identify the concepts of damage incorpo-

rated into the plastic model, that is, the concept of effective stresses from Damage Mechanics is used to represent the loss of stiffness. In addition, the loss of stiffness of the materials will be identified, due to the decrease in stresses, after reaching the maximum stress, as the deformations increase.

It was possible to confirm that granite has a lower percentage of damage, since the material has low porosity. In other words, it has greater mechanical strength compared to the materials analyzed, unlike concrete, which is a material with a lot of porosity, which leaves it with low mechanical strength.

Table 4.1 shows the damage percentages of all concrete projectiles that can be seen in Fig's. 4.1-4.6 and show the maximum von Mises equivalent stresses and the final damages of each geometry at velocities of 10, 20, 40 and 60m/s, respectively. The results can be summarized as follows,

- At an impact speed of 10m/s only the 45° pointed projectiles and the 7.5mm oval were damaged less than 50% of the initial volume.
- At an impact velocity of 20m/s only the 45° sharp projectile was damaged less than 60% of the initial volume.
- At an impact speed of 40m/s only the 45° pointed projectiles and the 7.5mm oval were damaged less than 90% of the initial volume.
- At a speed of 60m/s all projectiles were damaged more than 90% of the initial volume.

Table 4.1: Percentage of damage to concrete projectiles after impact on the metallic flat counterpart

V(m/s)	SPH7.5mm	SPH15mm	SRP30º	SRP45º	OVA7.5mm	OVA15mm
10	65%	55%	55%	25%	45%	60%
20	85%	88%	70%	30%	65%	90%
40	99%	95%	95%	80%	85%	98%
60	100%	99%	98%	95%	90%	100%

4.1.1 Concrete qualitative behavior

By evaluating Fig's 4.1-4.6, it is possible to understand how the shape and velocity of the particle affect the mechanical behavior, considering that for each of the 6 geometries, four velocities were used with the concrete projectile and specific stresses and damage were generated for each geometry.

The increase in impact velocity shown in Fig. 4.1 illustrates the evolution of the von Mises equivalent stress and the damage to the Ø7.5 sphere particle. The first column of Fig. 4.1 shows the von Mises equivalent stress values at the moment of impact in frame 21

and the second column shows it in frame 25. In view of this, it is possible to observe the shape of the stress distribution in the projectile and stress displacement critical according to the evolution of the evaluated frame. It is important to emphasize that when evaluating the equivalent von Mises stress in frame 25, the numerical values are lower than the value in frame 21 in this condition. Exception to this is the speed of 60m/s, considering that as the contact time increases, the contact area will be larger due to the increase in deformation. The increase in speed causes significant damage to the material, and from the speed of 10m/s onwards the projectile goes through the shattering process and the material is completely damaged from 40m/s onwards.

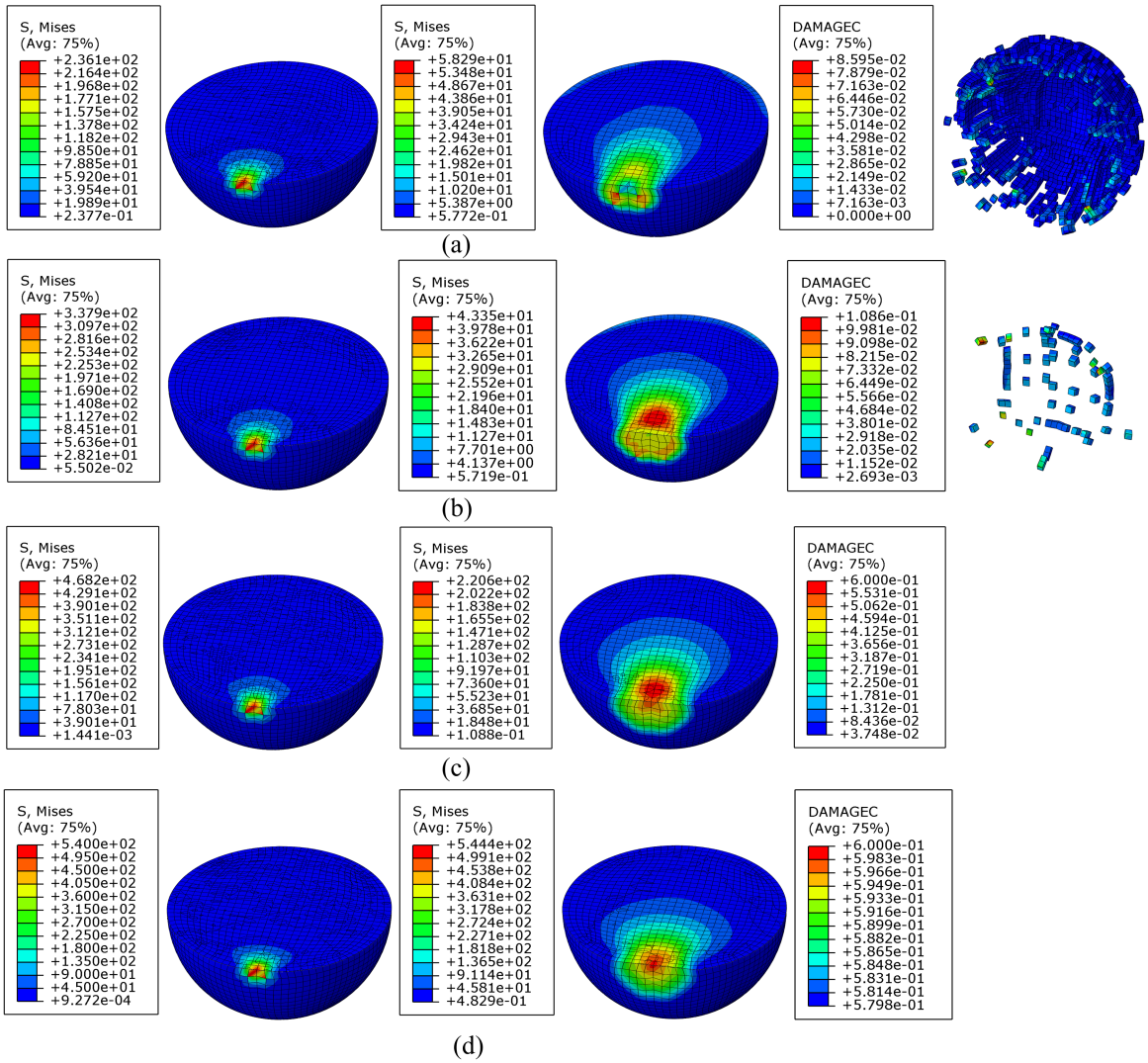

Figure 4.1: In the first column, the equivalent von Mises stresses in the impact frame 21 are presented, in the second column in frame 25 and in the last column the final damage of the material under conditions (a) CON-SPH75-10 (b) CON-SPH75-20 (c) CON-SPH75-40 (d) CON-SPH75-60

The increase in impact velocity shown in Fig. 4.2 illustrates the evolution of the von Mises equivalent stress and the damage to the Ø15 sphere particle. The first column of

Fig. 4.2 shows the von Mises equivalent stress values at the moment of impact in frame 21, and the second column shows it in frame 25. In light of this, it is possible to observe the shape of the stress distribution in the projectile and the displacement of the critical stress according to the evolution of the evaluated frame. It is important to note that when evaluating the equivalent von Mises stress in frame 25, the numerical values are lower than the value of frame 21 in this condition, with the exception of the speed of 60m/s, considering that according to the increase in the contact, the greater the contact area due to increased deformation. The increase in speed causes significant damage to the material. From a velocity of 10m/s onwards, the projectile goes through the shattering process and the material is completely damaged from 40m/s onwards.

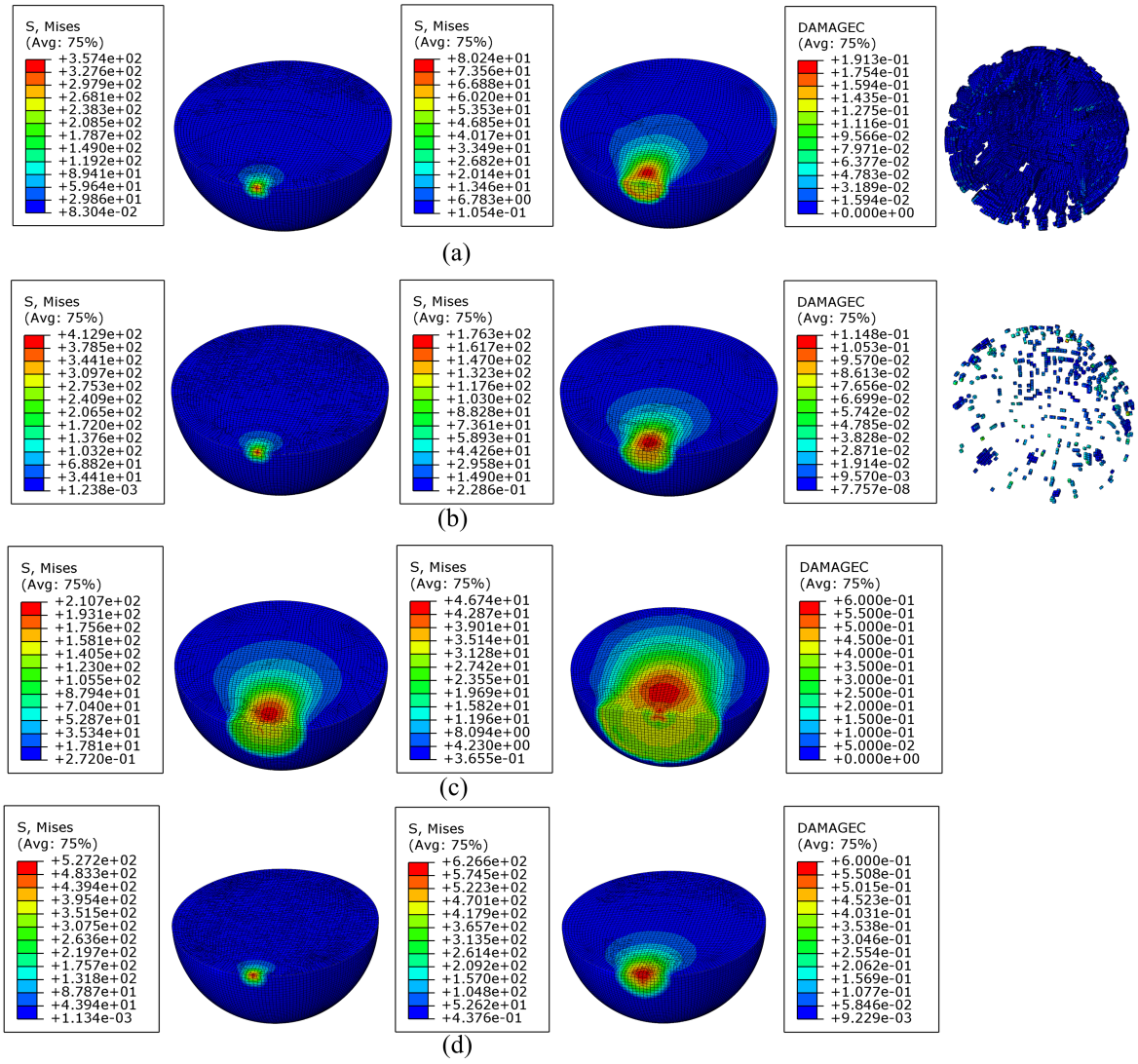

Figure 4.2: In the first column, the equivalent von Mises stresses in the impact frame 21 are presented, in the second column in frame 25 and in the last column the final damage of the material under conditions (a)CON-SPH15-10 (b) CON-SPH15-20 (c) CON-SPH15-40 (d) CON-SPH15-60

The increase in impact velocity shown in Fig. 4.3 illustrates the evolution of the von

Mises equivalent stress and the damage to the Ø7.5 oval particle. The first column of Fig. 4.3 shows the von Mises equivalent stress values at the moment of impact in frame 21, while the second column shows in frame 25. In view of this, it is possible to observe the shape of the stress distribution in the projectile and the displacement of the critical stress according to the evolution of the evaluated frame. It is important to note that when evaluating the equivalent von Mises stress in frame 25 the numerical values are higher than the value in frame 21 in this condition, considering that, according to the analyzed geometry, the contact area does not increase significantly between these two frames which provides greater tensions. The increase in speed causes significant damage to the material. From a speed of 10m/s, the projectile goes through the shattering process, but the material is not completely damaged.

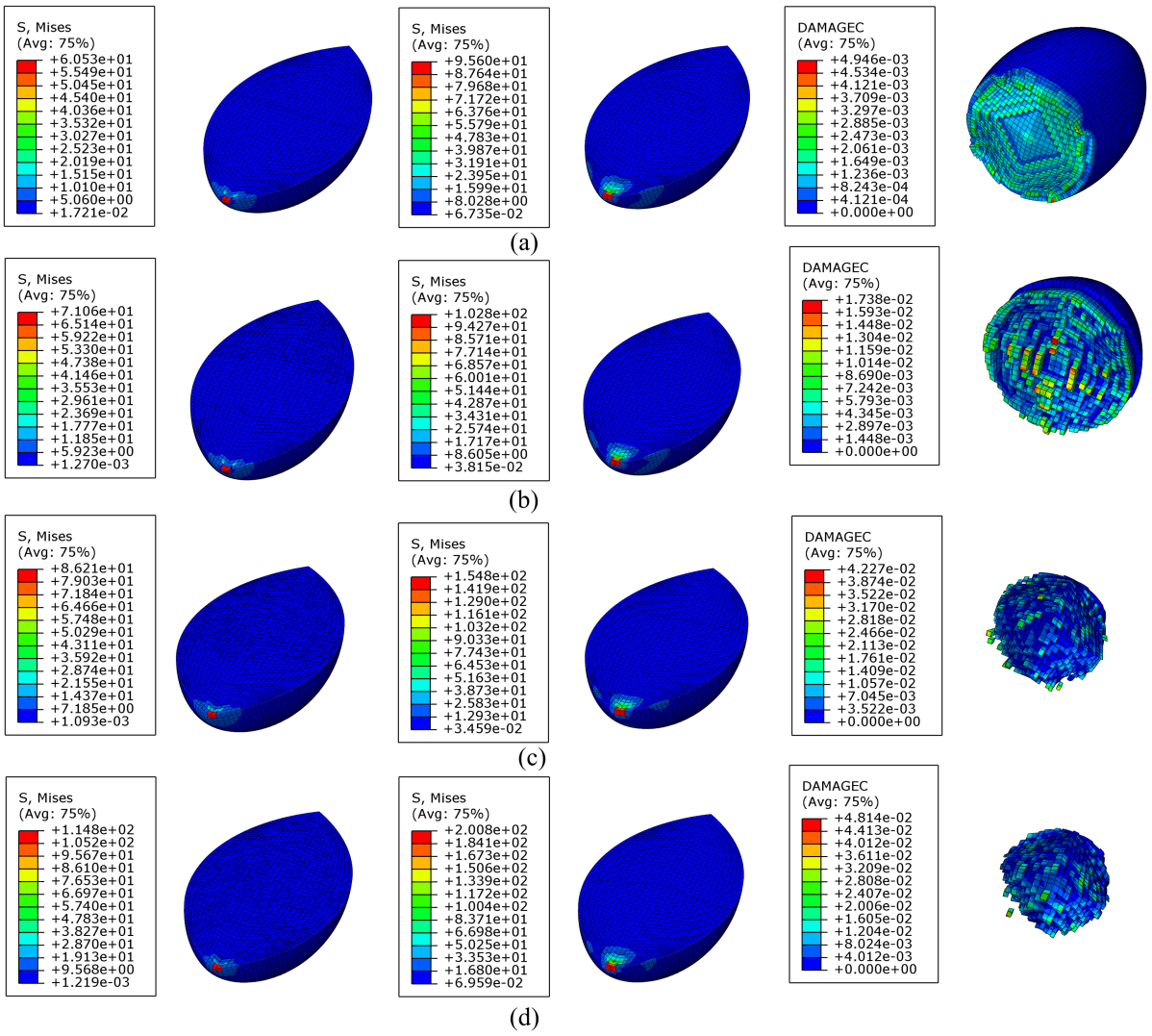

Figure 4.3: In the first column, the equivalent von Mises stresses in the impact frame 21 are presented, in the second column in frame 25 and in the last column the final damage of the material under conditions (a) CON-OVA75-10 (b) CON-OVA75-20 (c) CON-OVA75-40 (d) CON-OVA75-60

The increase in impact velocity shown in Fig. 4.4 illustrates the evolution of the von

Mises equivalent stress and the damage to the Ø15 oval particle. The first column of Fig. 4.4 shows the von Mises equivalent stress values at the moment of impact in frame 21, while the second column shows in frame 25. In view of this, it is possible to observe the shape of the stress distribution in the projectile and the displacement of the critical stress according to the evolution of the evaluated frame. It is important to note that when evaluating the equivalent von Mises stress in frame 25, the numerical values are lower than the value of frame 21 in this condition, with the exception of the speed of 60m/s, considering that according to the increase in the contact, the greater the contact area due to increased deformation. The increase in speed causes significant damage to the material. From a speed of 10m/s, the projectile goes through the shattering process and the material is completely damaged at 60m/s.

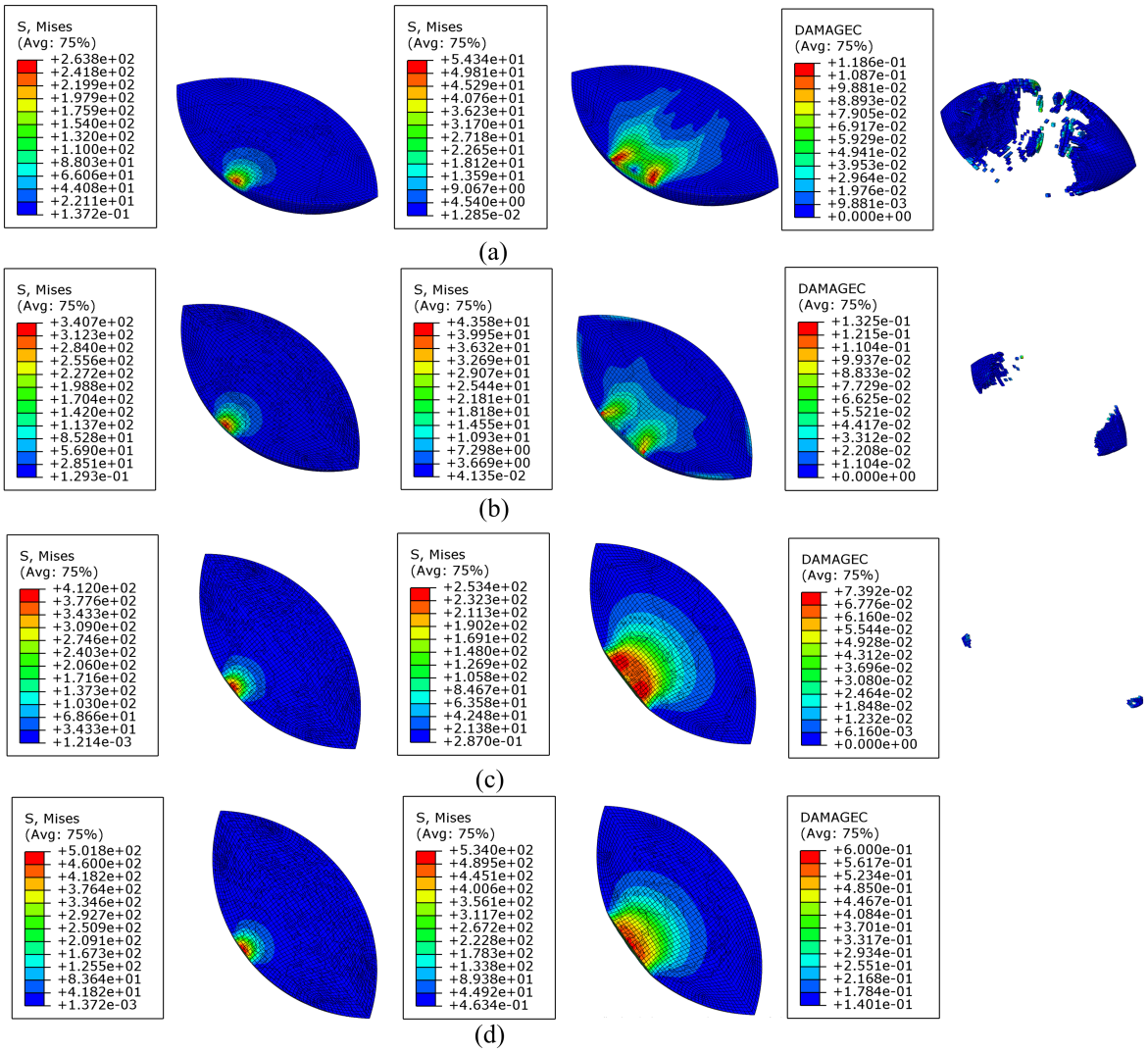

Figure 4.4: In the first column, the equivalent von Mises stresses in the impact frame 21 are presented, in the second column in frame 25 and in the last column the final damage of the material under conditions (a)CON-OVA15-10 (b) CON-OVA15-20 (c) CON-OVA15-40 (d) CON-OVA15-60

The increase in impact velocity shown in Fig .4.5 illustrates the evolution of the von Mises equivalent stress and the damage to the 30° sharp particle. The first column of Fig. 4.5 shows the von Mises equivalent stress values at the moment of impact in frame 21, while the second column shows in frame 25. In view of this, it is possible to observe the shape of the stress distribution in the projectile and the displacement of the critical stress according to the evolution of the evaluated frame. It is important to emphasize that when evaluating the equivalent von Mises stress in frame 25, the numerical values are lower than the value of frame 21 at speeds of 10 and 20m/s, and higher at speeds of 40 and 60m/s. The increase in speed causes significant damage to the material. From a speed of 10m/s, the projectile goes through the shattering process and the material is not completely damaged in any of the conditions.

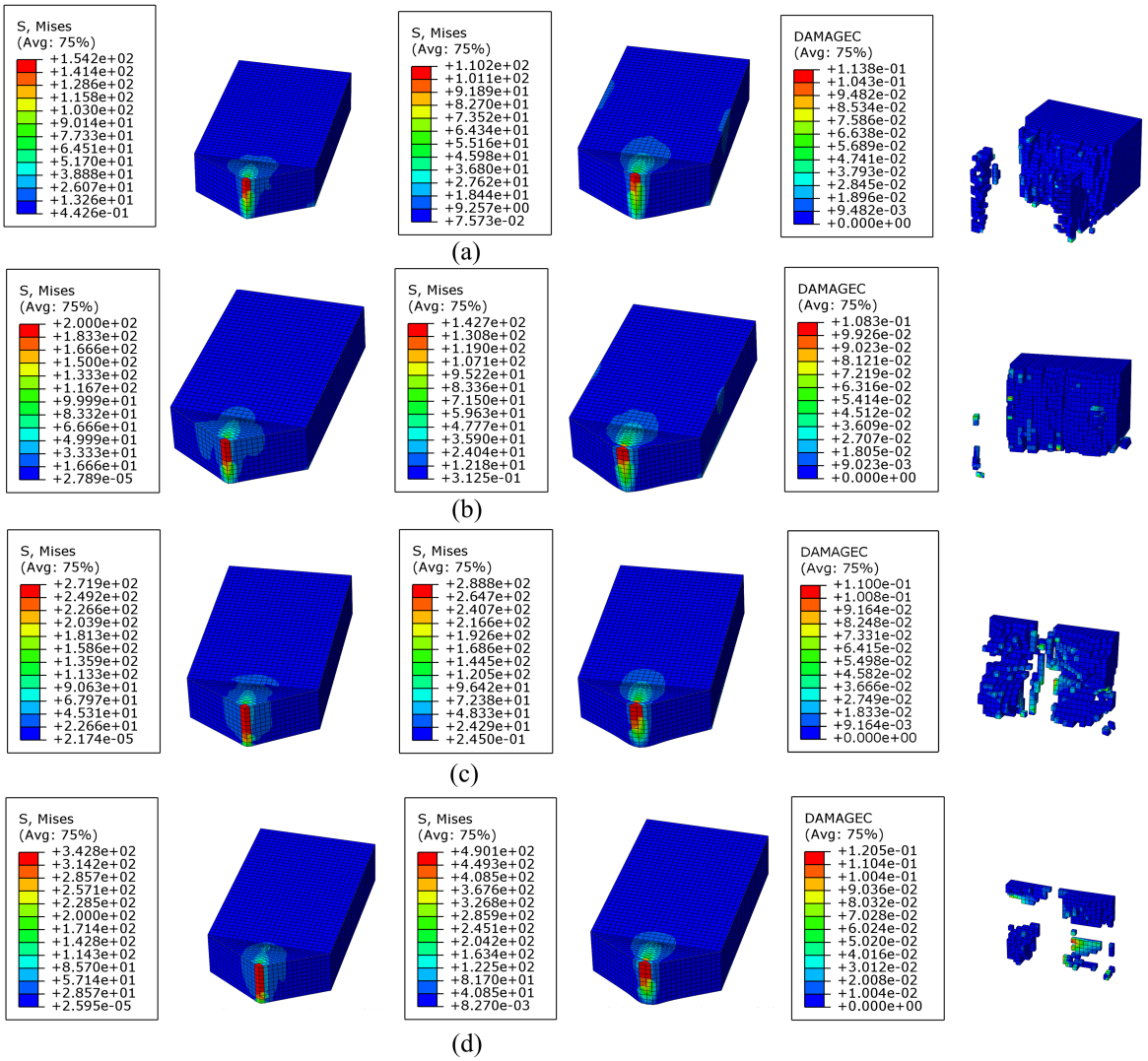

Figure 4.5: In the first column, the equivalent von Mises stresses in the impact frame 21 are presented, in the second column in frame 25 and in the last column the final damage of the material under conditions (a) CON-SRP30-10 (b) CON- SRP30-20 (c) CON-SRP30-40 (d) CON-SRP30-60

The increase in impact velocity shown in Fig. 4.6 illustrates the evolution of the von Mises equivalent stress and the damage to the 45° sharp particle. The first column of Fig. 4.6 shows the von Mises equivalent stress values at the moment of impact in frame 21, while the second column shows in frame 25. In view of this, it is possible to observe the shape of the stress distribution in the projectile and the displacement of the critical stress according to the evolution of the evaluated frame. It is important to emphasize that when evaluating the equivalent von Mises stress in frame 25, the numerical values are lower than the value in frame 21, with the exception of the speed of 10m/s. The increase in speed causes significant damage to the material. From a speed of 10m/s, the projectile goes through the shattering process and the material is not completely damaged in any of the conditions.

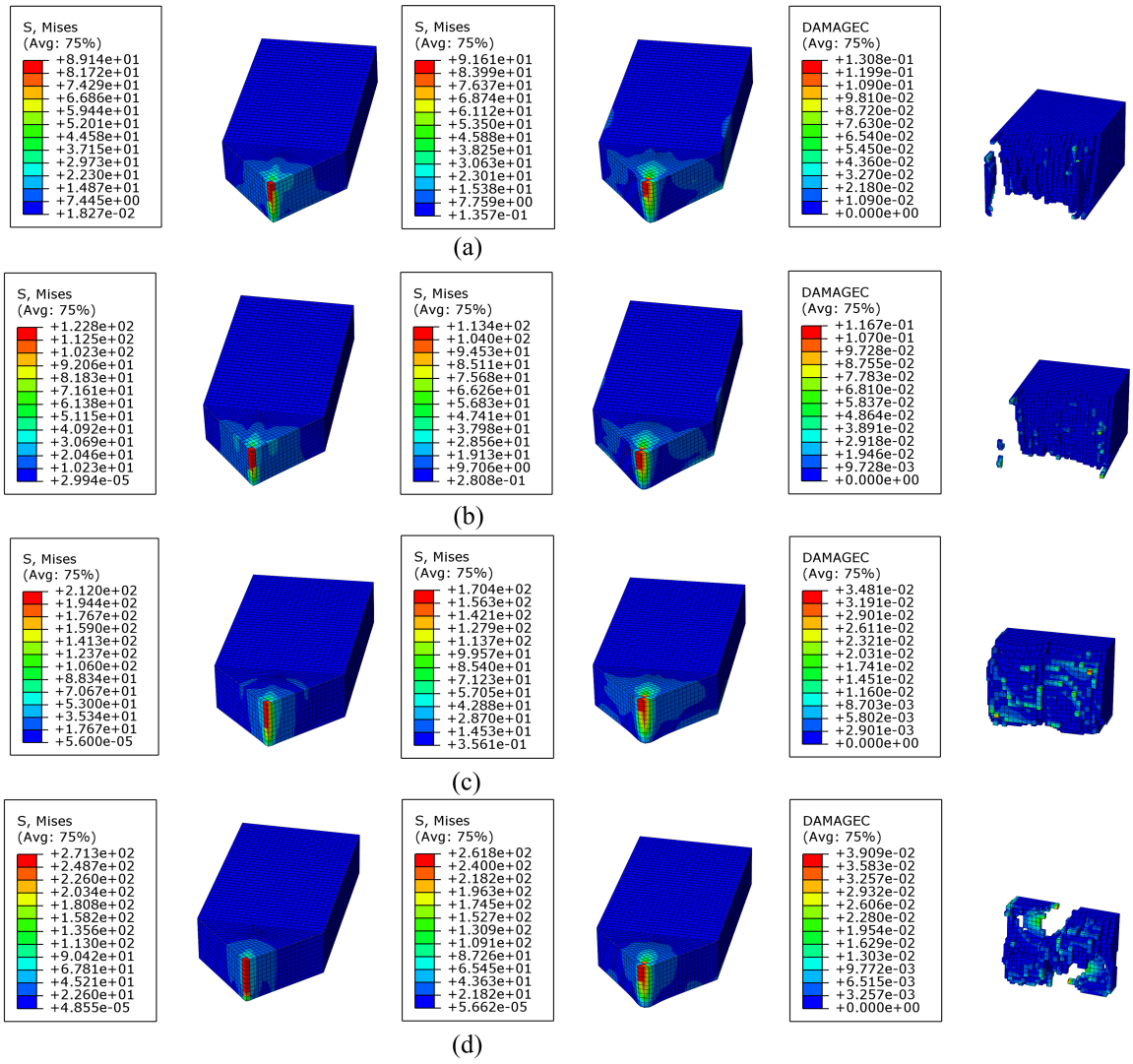

Figure 4.6: In the first column, the equivalent of Mises stresses in the impact frame 21 are presented, in the second column in frame 25 and in the last column the final damage of the material under conditions (a) CON-SRP45-10 (b) CON-SRP45-20 (c) CON-SRP45-40 (d) CON-SRP45-60

Table 4.2 shows the damage percentages of all arenite projectiles that can be seen in

Fig's 4.7-4.12. These figures show the maximum von Mises equivalent stresses, the contact pressures and the Final damage of each geometry at speeds of 10, 20, 40 and 60m/s respectively. After evaluating the results obtained, it was noted that the percentage of damage from the projectile impacting on the flat counterpart:

- At an impact speed of 10m/s all projectiles were damaged less than 25% of initial volume.
- At an impact velocity of 20m/s only the 45° pointed projectile and the 7.5 mm oval were damaged less than 40% of the initial volume.
- At an impact speed of 40m/s only the 45° pointed projectiles and the 7.5mm oval were damaged less than 50% of the initial volume.
- At a speed of 60m/s only the 45° pointed projectile damaged less than 80% of its initial volume.

Table 4.2: Percentage of damage to arenite projectiles after impact on the metallic flat counterpart

V(m/s)	SPH7.5mm	SPH15mm	SRP30º	SRP45º	OVA7.5mm	OVA15mm
10	20%	20%	20%	10%	15%	25%
20	75%	35%	55%	40%	30%	50%
40	90%	80%	70%	65%	45%	90%
60	99%	90%	80%	75%	85%	99%

4.1.2 Arenite qualitative behavior

By evaluating Fig's 4.7-4.12 it is possible to understand how the shape and velocity of the particle affect the mechanical behavior, considering that for each of the 6 geometries, four velocities were used with the arenite projectile and specific stresses and damage were generated for each geometry.

The increase in impact velocity shown in Fig. 4.7 illustrates the evolution of the von Mises equivalent stress and the damage to the Ø7.5 sphere particle, with the exception of the velocity of 40m/s in frame 21 where a stress peak occurs. The first column of Fig. 4.7 shows the von Mises equivalent stress values at the moment of impact in frame 21, while the second column shows in frame 25. In view of this, it is possible to observe the shape of the stress distribution in the projectile and the displacement of the critical stress according to the evolution of the evaluated frame. It is important to emphasize that when evaluating the equivalent von Mises stress in frame 25, the numerical values are lower than the value of frame 21 at speeds of 10 and 20m/s, and higher at speeds of 40 and 60m/s. The increase in speed causes significant damage to the material, from the speed of 10m/s the projectile goes through the shattering process and the material is not completely damaged.

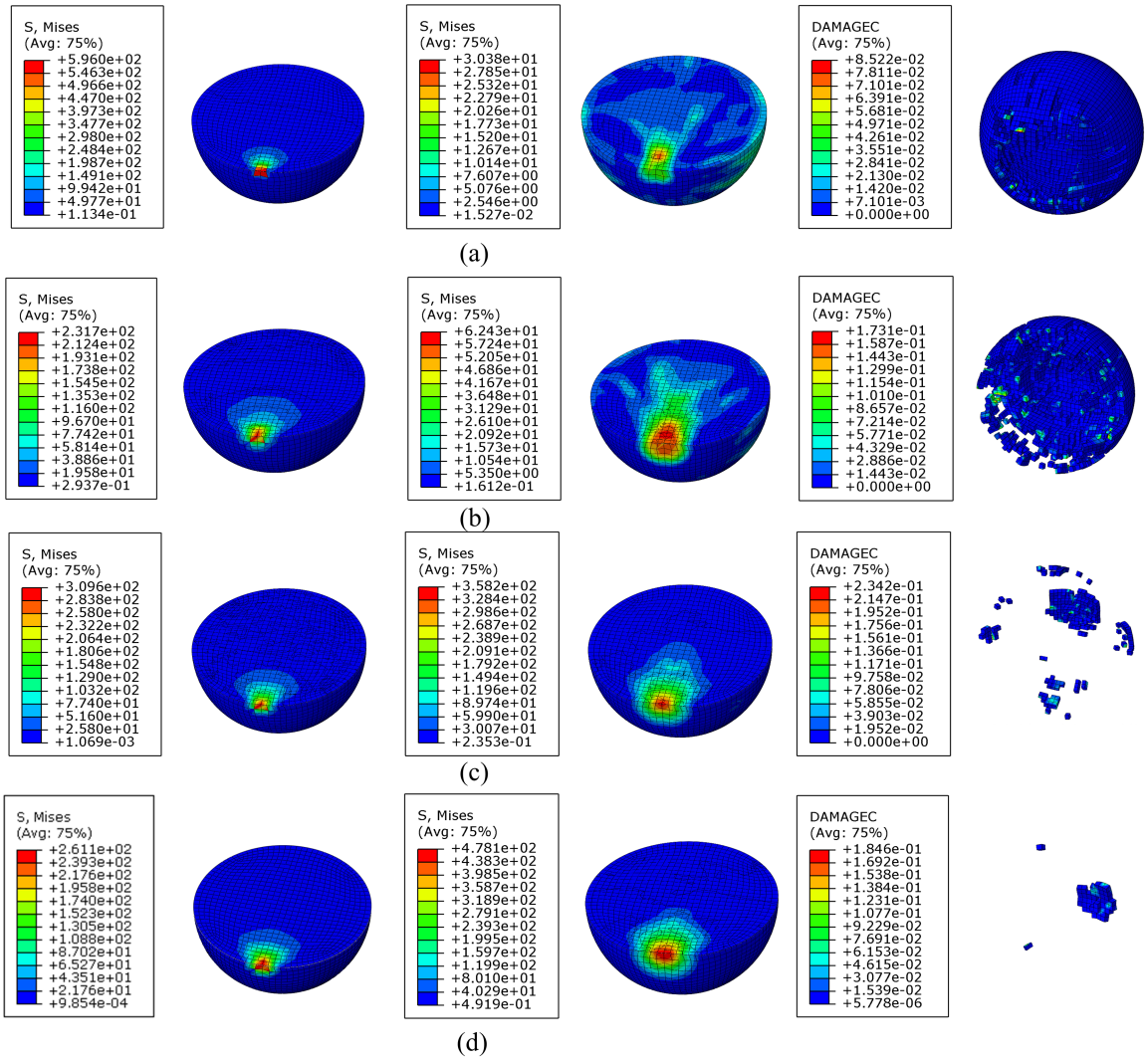

Figure 4.7: In the first column, the equivalent von Mises stresses in the impact frame 21 are presented, in the second column in frame 25 and in the last column the final damage of the material under conditions (a) ARE-SPH75-10 (b) ARE-SPH75-20 (c) ARE-SPH75-40 (d) ARE-SPH75-60

The increase in impact velocity shown in Fig. 4.8 illustrates the evolution of the von Mises equivalent stress and the damage to the Ø15 sphere particle, with the exception of the velocity of 20m/s in frame 21 where a stress peak occurs. The first column of Fig. 4.8 shows the von Mises equivalent stress values at the moment of impact in frame 21, while the second column shows in frame 25. In view of this, it is possible to observe the shape of the stress distribution in the projectile and the displacement of the critical stress according to the evolution of the evaluated frame. It is important to emphasize that when evaluating the equivalent von Mises stress in frame 25, the numerical values are lower than the value of frame 21 at speeds of 10 and 20m/s, and higher at speeds of 40 and 60m/s. The increase in speed causes significant damage to the material. From a speed of 10m/s, the projectile goes through the shattering process and the material is not completely damaged.

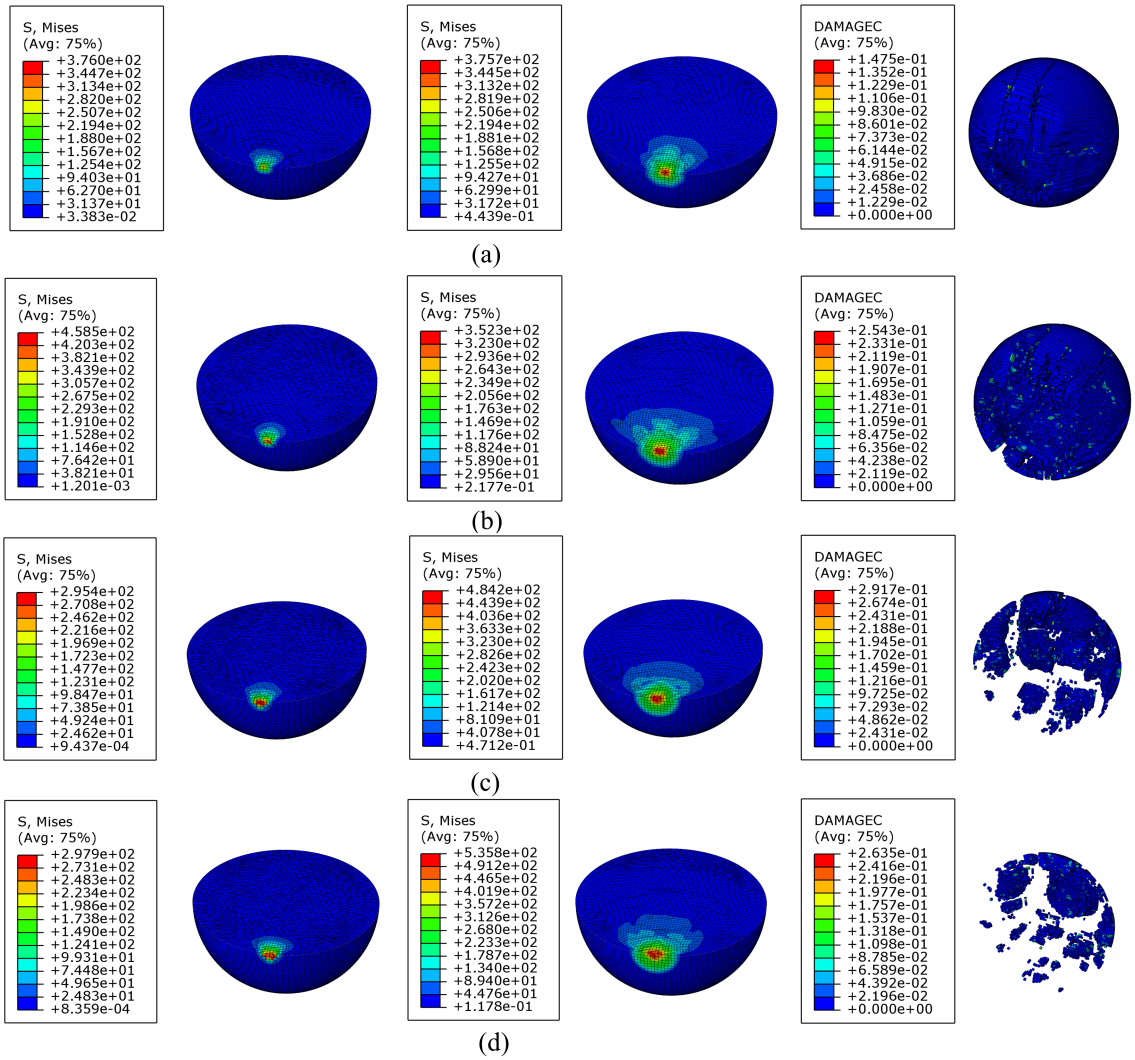

Figure 4.8: In the first column, the equivalent von Mises stresses in the impact frame 21 are presented, in the second column in frame 25 and in the last column the final damage of the material under conditions (a) ARE-SPH15-10 (b) ARE-SPH15-20 (c) ARE-SPH15-40 (d) ARE-SPH15-60

The increase in impact velocity shown in Fig. 4.9 illustrates the evolution of the von Mises equivalent stress and the damage to the Ø7.5 oval particle, with the exception of the 40m/s velocity in frame 21 where there is a decrease in stress compared to other conditions. The first column of Fig. 4.9 shows the von Mises equivalent stress values at the moment of impact in frame 21, while the second column shows in frame 25. In view of this, it is possible to observe the shape of the stress distribution in the projectile and the displacement of the critical stress according to the evolution of the evaluated frame. It is important to note that when evaluating the equivalent von Mises stress in frame 25 the numerical values are higher than the value in frame 21 in this condition, considering that, according to the analyzed geometry, the contact area does not increase significantly between these two frames which provides greater tensions. The increase in speed causes significant damage to the material.

From a speed of 10m/s, the projectile goes through the shattering process, but the material is not completely damaged.

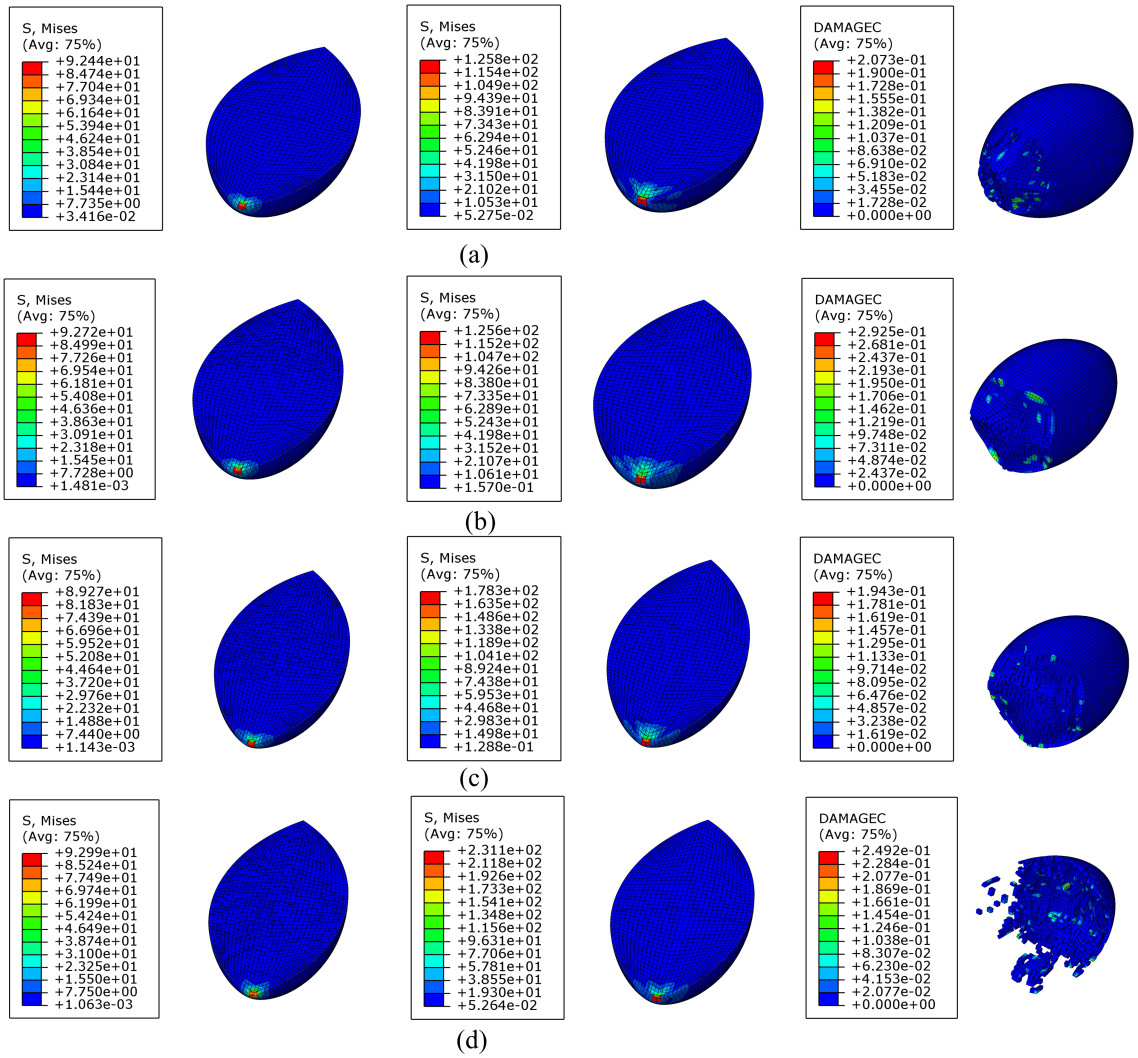

Figure 4.9: In the first column the equivalent von Mises stresses in the impact frame 21 are presented, in the second column in frame 25 and in the last column the final damage of the material under conditions (a) ARE-OVA75-10 (b) ARE-OVA75-20 (c) ARE-OVA75-40 (d) ARE-OVA75-60

The increase in impact velocity shown in Fig. 4.10 illustrates the evolution of the von Mises equivalent stress and the damage to the Ø15 oval particle, with the exception of the velocity of 40m/s in frame 21 where a stress peak occurs compared to the other conditions. The first column of Fig. 4.10 shows the von Mises equivalent stress values at the moment of impact in frame 21, while the second column shows in frame 25. In view of this, it is possible to observe the shape of the stress distribution in the projectile and the displacement of the critical stress according to the evolution of the evaluated frame. It is important to note that when evaluating the equivalent von Mises stress in frame 25, the numerical values are lower than the value of frame 21 in this condition, with the exception of the speed of 60m/s,

considering that according to the increase in the contact, the greater the contact area due to increased deformation. The increase in speed causes significant damage to the material. From a speed of 10m/s, the projectile goes through the shattering process and the material is completely damaged at 60m/s.

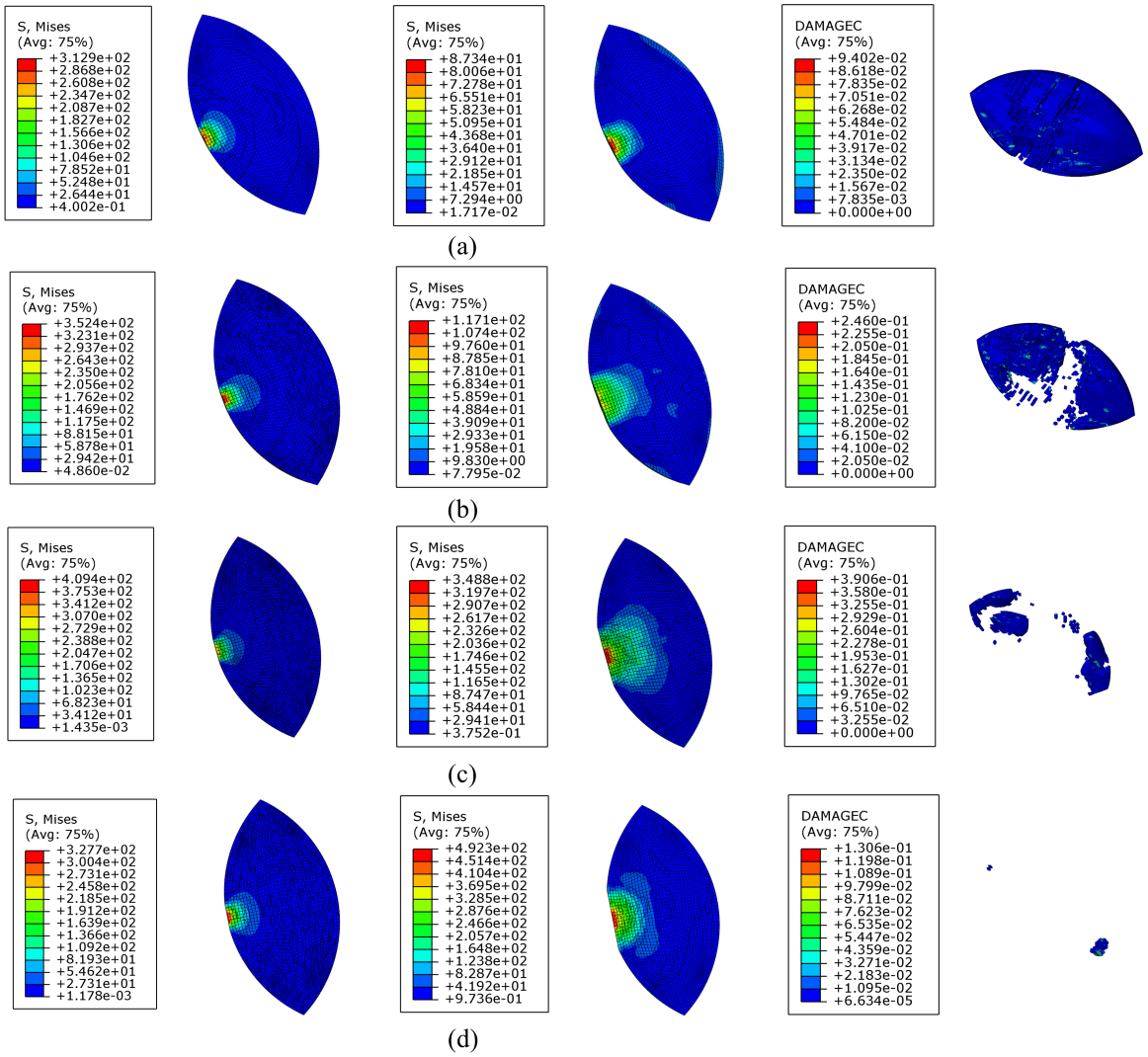

Figure 4.10: In the first column, the equivalent von Mises stresses in the impact frame 21 are presented, in the second column in frame 25 and in the last column the final damage of the material under conditions (a) ARE-OVA15-10 (b) ARE-OVA15-20 (c) ARE-OVA15-40 (d) ARE-OVA15-60

The increase in impact velocity shown in Fig. 4.11 illustrates the evolution of the von Mises equivalent stress and the damage to the 30° sharp particle, with the exception of the 20m/s velocity in frame 21 where a stress peak occurs compared to other conditions. The first column of Fig. 4.11 shows the von Mises equivalent stress values at the moment of impact in frame 21, while the second column shows in frame 25. In view of this, it is possible to observe the shape of the stress distribution in the projectile and the displacement of the critical stress according to the evolution of the evaluated frame. It is important to emphasize

that when evaluating the equivalent von Mises stress in frame 25, the numerical values are lower than the value of frame 21 at speeds of 10 and 20m/s, and higher at speeds of 40 and 60m/s. The increase in speed causes significant damage to the material, from the speed of 10m/s the projectile goes through the shattering process and the material is not completely damaged in any of the conditions.

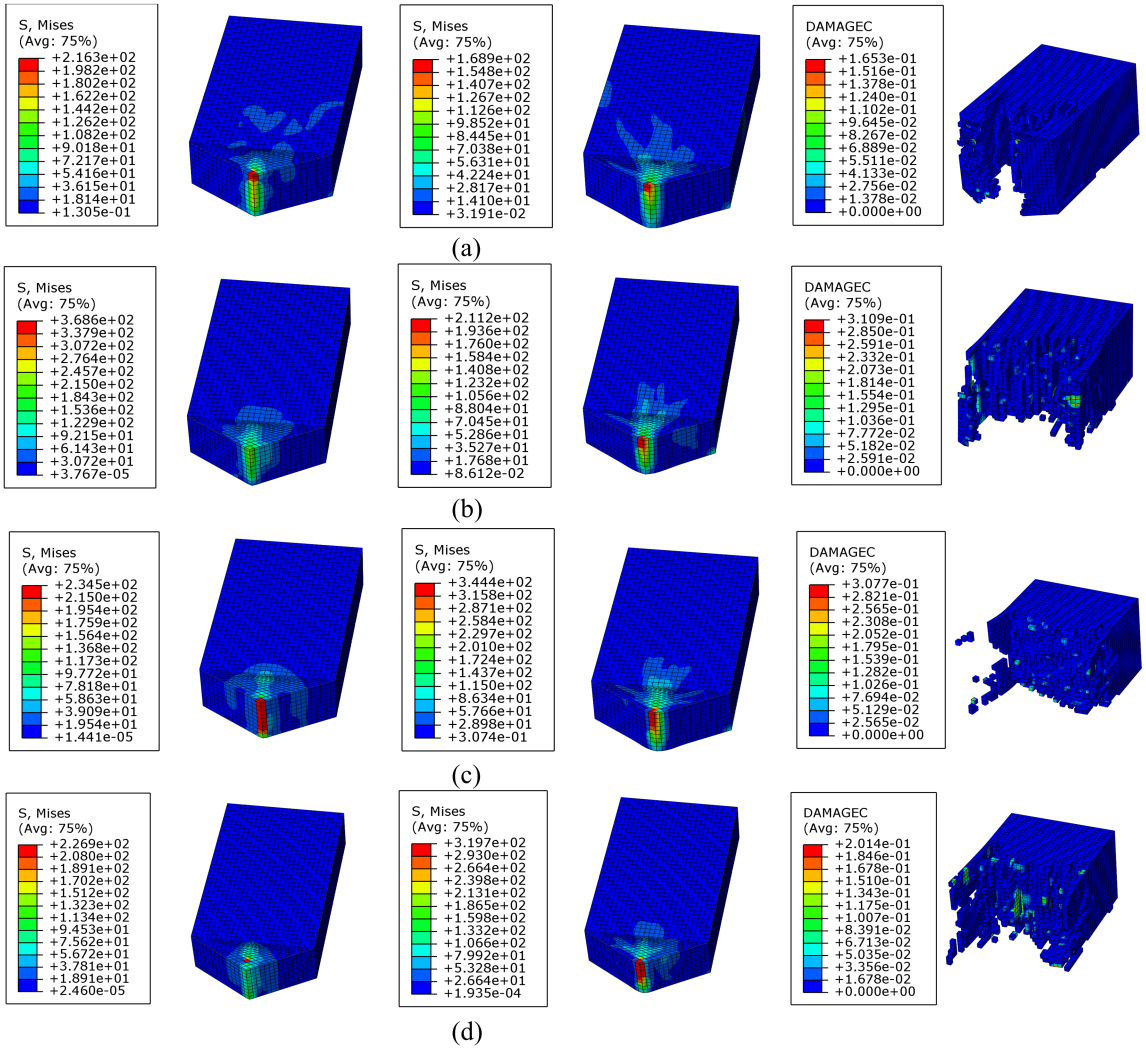

Figure 4.11: In the first column the equivalent von Mises stresses in the impact frame 21 are presented, in the second column in frame 25 and in the last column the final damage of the material under conditions (a) ARE-SRP30-10 (b) ARE-SRP30-20 (c) ARE-SRP30-40 (d) ARE-SRP30-60

The increase in impact velocity shown in Fig. 4.12 illustrates the evolution of the von Mises equivalent stress and the damage to the 45° sharp particle. The first column of Fig. 4.12 shows the von Mises equivalent stress values at the moment of impact in frame 21, while the second column shows in frame 25. In view of this, it is possible to observe the shape of the stress distribution in the projectile and the displacement of the critical stress according to the evolution of the evaluated frame. It is important to emphasize that when evaluating the

equivalent von Mises stress in frame 25, the numerical values are higher than the value in frame 21. The increase in speed causes significant damage to the material. From a speed of 10m/s, the projectile goes through the shattering process and the material is not completely damaged in any of the conditions.

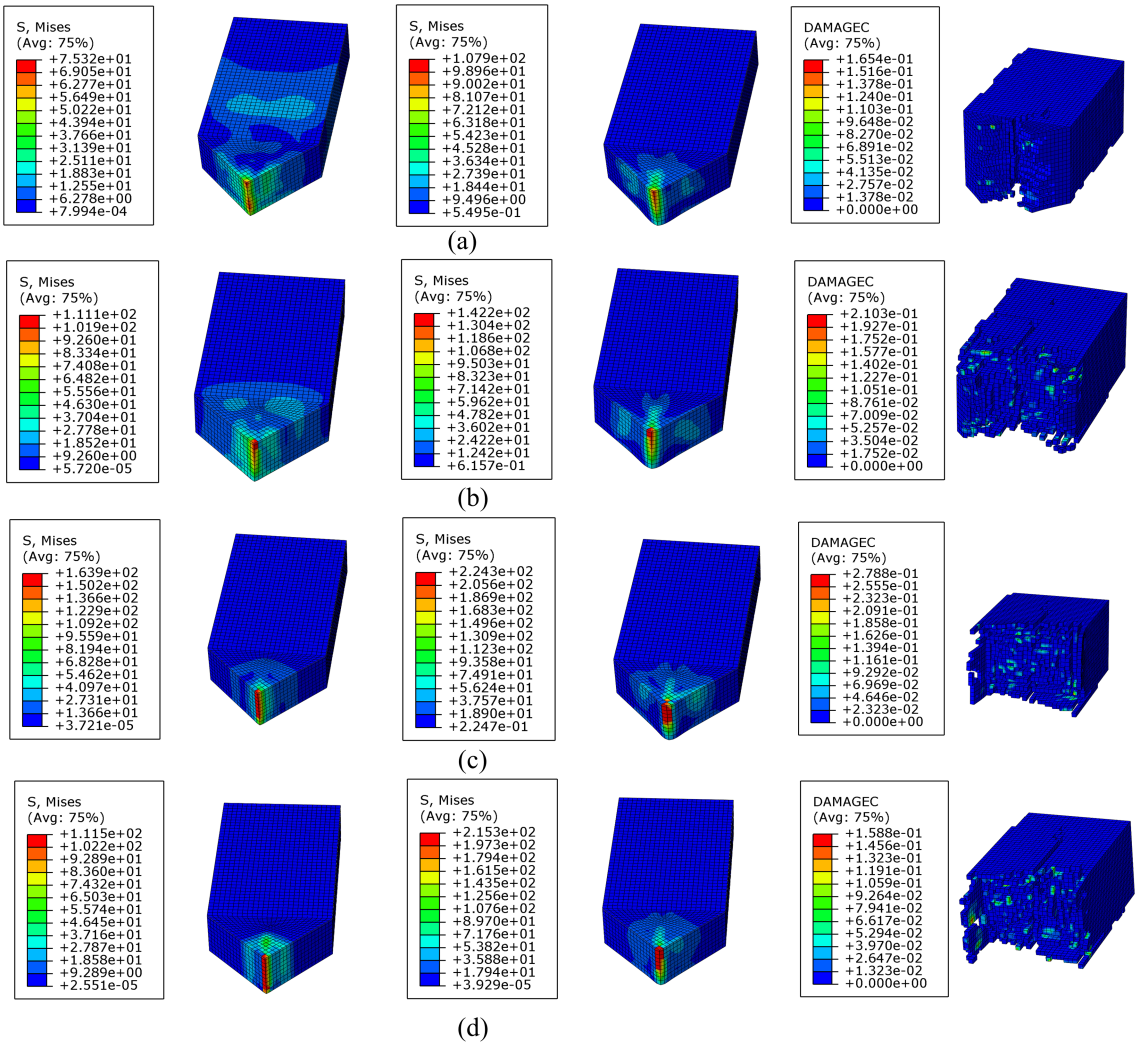

Figure 4.12: In the first column the equivalent von Mises stresses in the impact frame 21 are presented, in the second column in frame 25 and in the last column the final damage of the material under conditions (a) ARE-SRP45-10 (b) ARE-SRP45-20 (c) ARE-SRP45-40 (d) ARE-SRP45-60

Table 4.3 shows the damage percentages of all granite projectiles that can be seen in Fig's. 4.13-4.18 and show the maximum von Mises equivalent stresses, contact pressures and final damage of each geometry at speeds of 10, 20, 40 and 60m/s, respectively. After evaluating the results obtained, it was noted that the percentage of damage from the projectile impacting on the flat counterpart a:

- At an impact speed of 10m/s all projectiles were damaged less than 25% of initial

volume.

- At an impact velocity of 20m/s only the 45° pointed projectile and the 7.5 mm oval were damaged less than 25% of the initial volume.
- An impact velocity of 40m/s only the 7.5 mm oval projectile was damaged less than 50% of the initial volume.
- At a speed of 60m/s all projectiles were damaged more than 80% of their initial volume.

Table 4.3: Percentage of damage to granite projectiles after impact on the metallic flat counterpart.

V(m/s)	SPH7.5mm	SPH15mm	SRP30º	SRP45º	OVA7.5mm	OVA15mm
10	5%	15%	25%	15%	10%	20%
20	45%	35%	45%	25%	20%	35%
40	85%	75%	75%	70%	45%	75%
60	98%	95%	85%	90%	85%	99%

4.1.3 Granite qualitative behavior

By evaluating Fig.'s 4.13-4.18, it is possible to understand how the shape and velocity of the particle affect the mechanical behavior, considering that for each of the 6 geometries, four velocities were used with the granite projectile and specific stresses and damage were generated for each geometry.

The increase in impact velocity shown in Fig. 4.13 illustrates the von Mises equivalent stress and the sphere particle damage of Ø7.5. The first column of Fig. 4.13 shows the von Mises equivalent stress values at the moment of impact in frame 21, while the second column shows in frame 25. In view of this, it is possible to observe the shape of the stress distribution in the projectile and the displacement of the critical stress according to the evolution of the evaluated frame. It is important to note that when evaluating the equivalent von Mises stress in frame 25, the numerical values are lower than the value in frame 21 in this condition, with the exception of the speed of 60m/s, considering that according to the increase in the contact, the greater the contact area due to increased deformation. The increase in speed causes significant damage to the material, from the speed of 10m/s the projectile goes through the shattering process and the material is not completely damaged in any of the conditions.

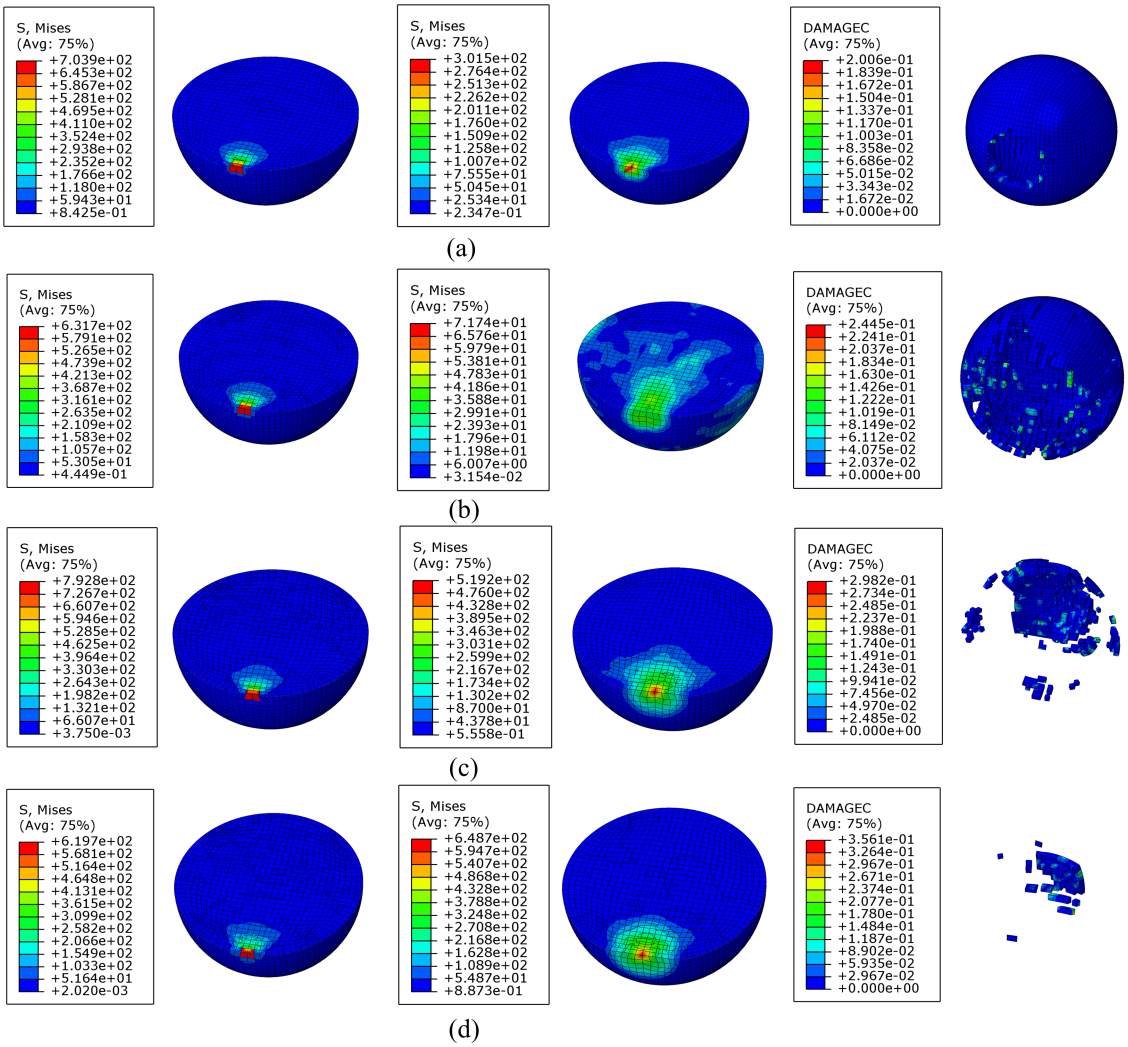

Figure 4.13: In the first column, the equivalent von Mises stresses in the impact frame 21 are presented, in the second column in frame 25 and in the last column the final damage of the material under conditions. (a) GRA-SPH75-10 (b) GRA-SPH75-20 (c) GRA-SPH75-40 (d) GRA-SPH75-60.

The increase in impact velocity shown in Fig. 4.14 illustrates the evolution of the von Mises equivalent stress and the damage to the Ø15mm sphere particle. The first column of Fig. 4.14 shows the von Mises equivalent stress values at the moment of impact in frame 21, while the second column shows in frame 25. In view of this, it is possible to observe the shape of the stress distribution in the projectile and the displacement of the critical stress according to the evolution of the evaluated frame. It is important to emphasize that when evaluating the equivalent von Mises stress in frame 25, the numerical values are higher than the value of frame 21 at speeds of 40 and 60m/s, and lower at speeds of 10 and 20m/s. The increase in speed causes significant damage to the material. From a speed of 10m/s, the projectile goes through the shattering process and the material is not completely damaged.

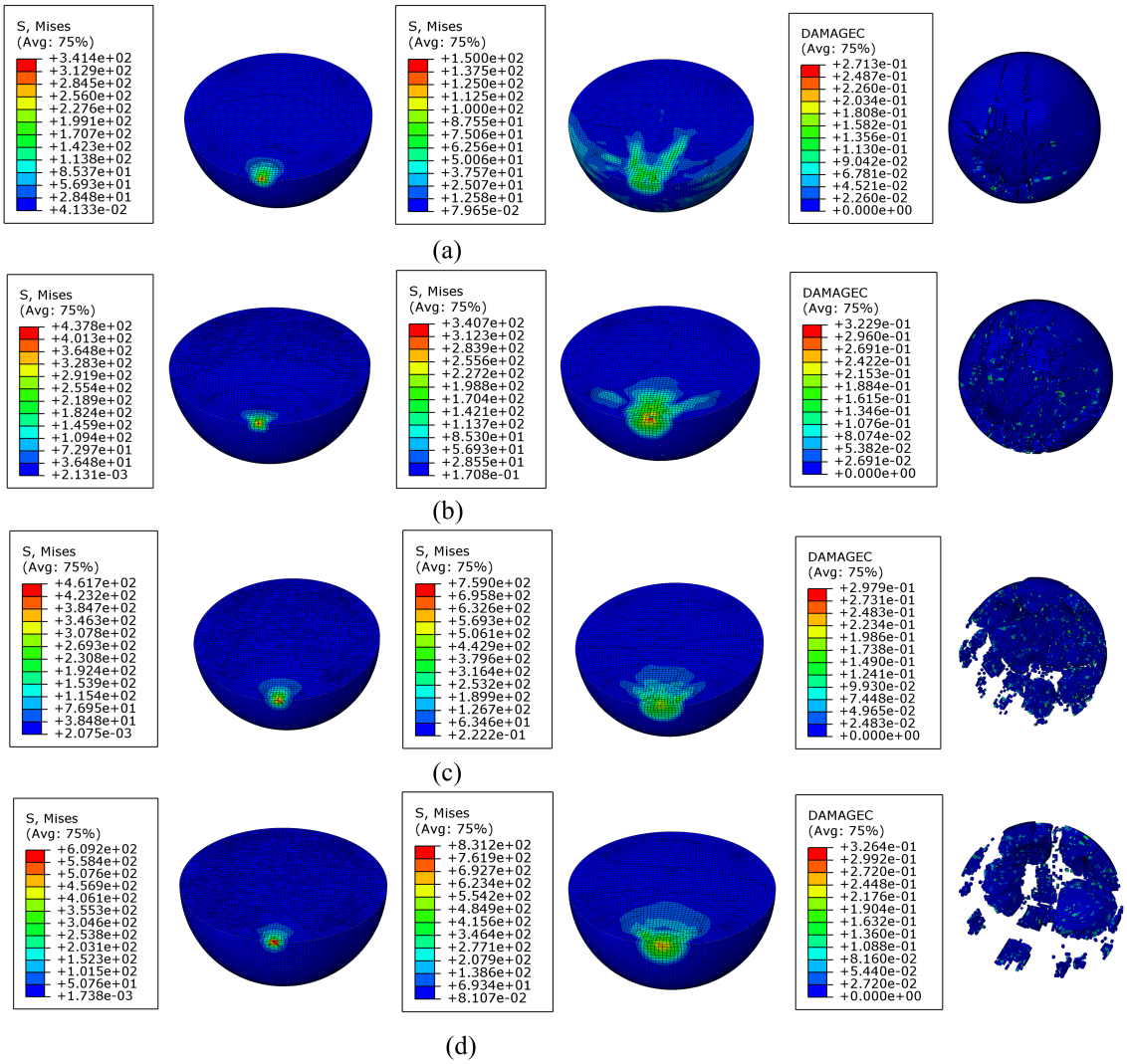

Figure 4.14: In the first column, the equivalent von Mises stresses in the impact frame 21 are presented, in the second column in frame 25 and in the last column the final damage of the material under conditions. (a) GRA-SPH15-10 (b) GRA-SPH15-20 (c) GRA-SPH15-40 (d) GRA-SPH15-60.

The increase in impact velocity shown in Fig. 4.15 illustrates the evolution of the von Mises equivalent stress and the damage to the Ø7.5 oval particle. The first column of Fig. 4.15 shows the von Mises equivalent stress values at the moment of impact in frame 21, while the second column shows in frame 25. In view of this, it is possible to observe the shape of the stress distribution in the projectile and the displacement of the critical stress according to the evolution of the evaluated frame. It is important to emphasize that when evaluating the equivalent von Mises stress in frame 25 the numerical values are higher than the value in frame 21 in this condition, considering that, according to the analyzed geometry, the contact area does not increase significantly between these two frames which provides greater tensions. The increase in speed causes significant damage to the material. From a speed of 10m/s, the projectile goes through the shattering process, but the material is not

completely damaged.

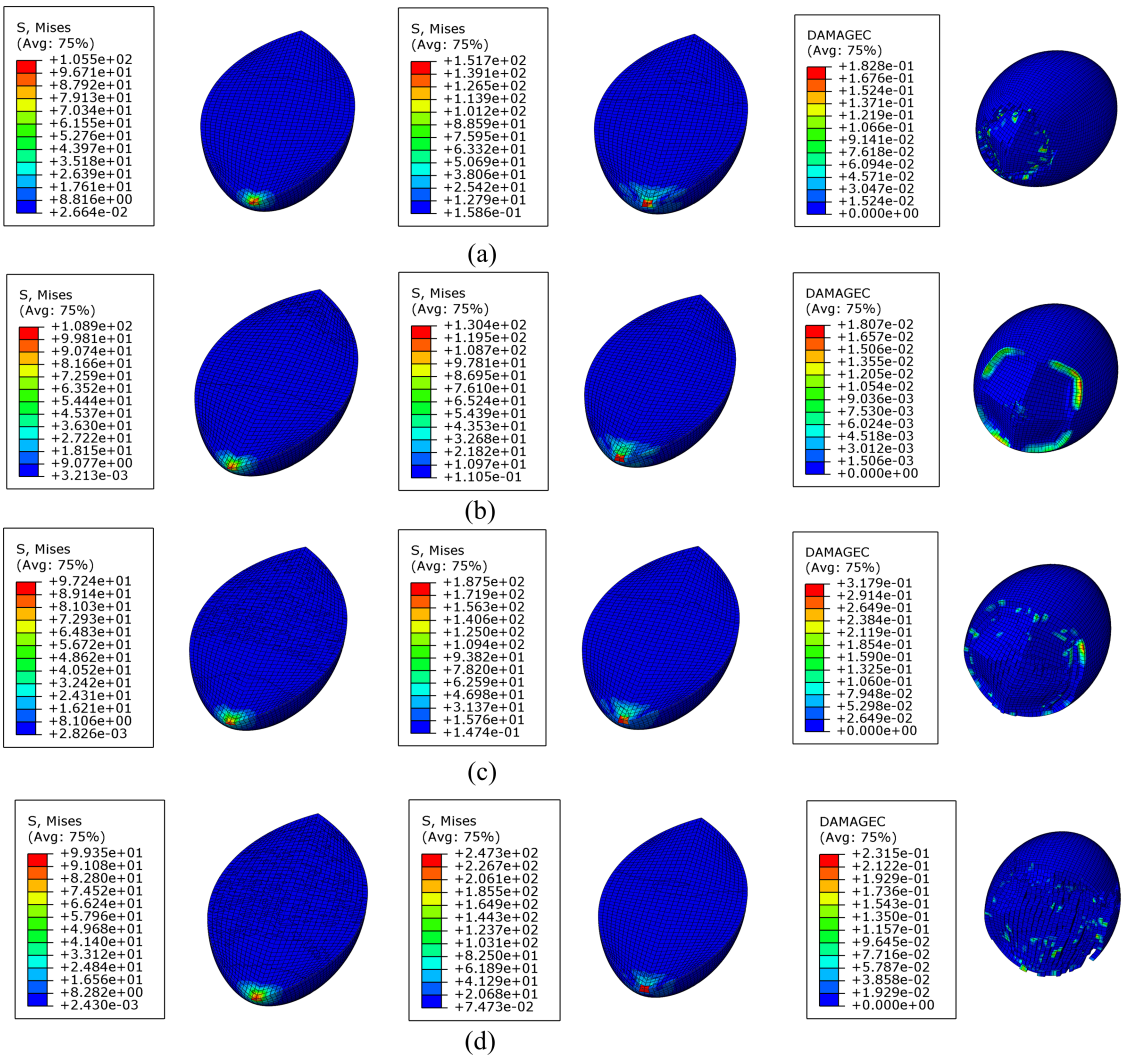

Figure 4.15: In the first column the equivalent von Mises stresses in the impact frame 21 are presented, in the second column in frame 25 and in the last column the final damage of the material under conditions. (a) GRA-OVA75-10 (b) GRA-OVA75-20 (c) GRA-OVA75-40 (d) GRA-OVA75-60.

The increase in impact velocity shown in Fig. 4.16 illustrates the evolution of the von Mises equivalent stress and the damage to the Ø15 oval particle. The first column of Fig. 4.16 shows the von Mises equivalent stress values at the moment of impact in frame 21, while the second column shows in frame 25. In view of this, it is possible to observe the shape of the stress distribution in the projectile and the displacement of the critical stress according to the evolution of the evaluated frame. It is important to note that when evaluating the equivalent von Mises stress in frame 25, the numerical values are lower than the value in frame 21 in this condition, with the exception of the speed of 60m/s, considering that according to the increase in the contact, the greater the contact area due to increased deformation. The increase in speed causes significant damage to the material. From a speed of 10m/s, the

projectile goes through the shattering process and the material is not completely damaged.

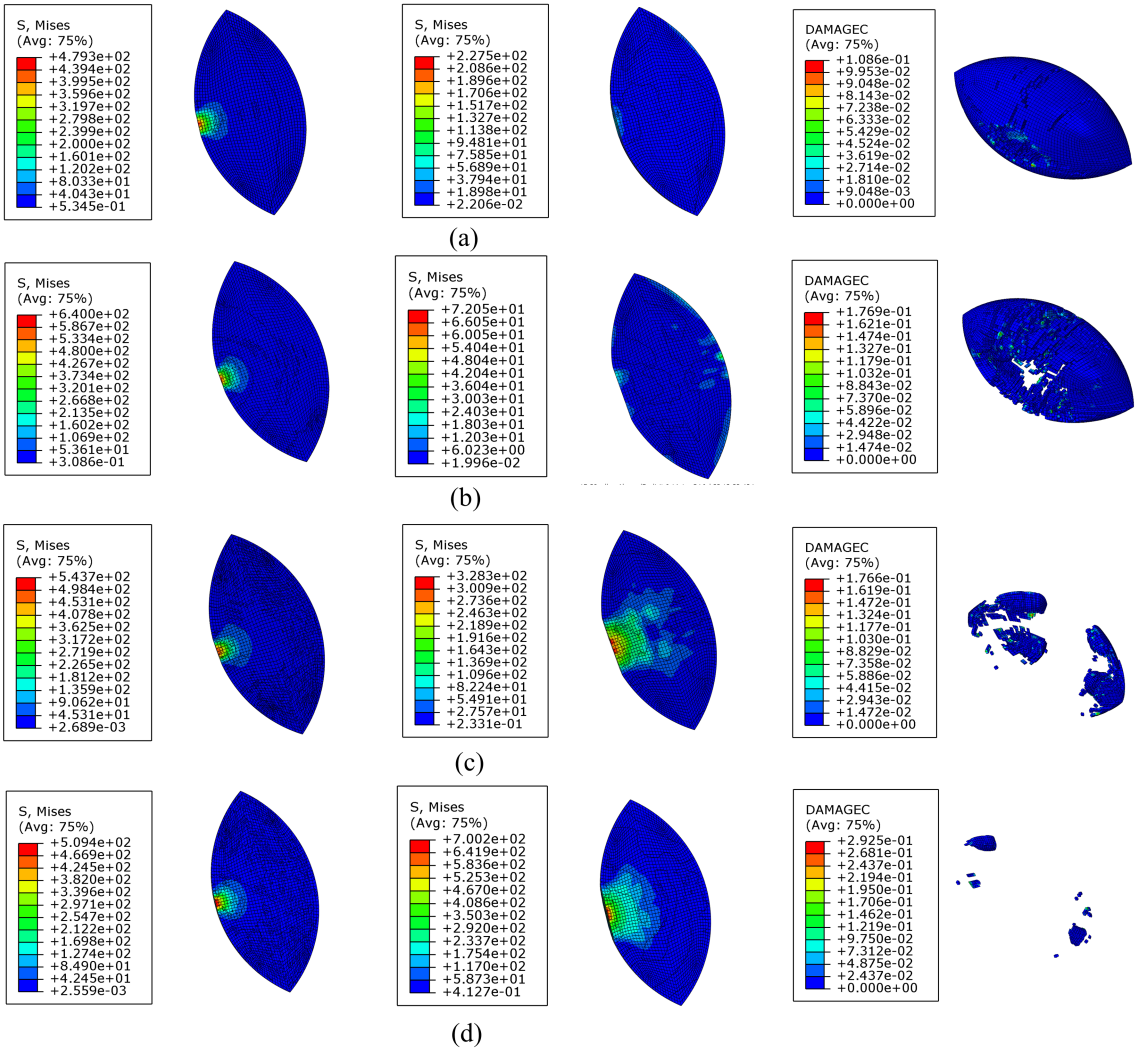

Figure 4.16: In the first column the equivalent von Mises stresses in the impact frame 21 are presented, in the second column in frame 25 and in the last column the final damage of the material under conditions. (a) GRA-OVA15-10 (b) GRA-OVA15-20 (c) GRA-OVA15-40 (d) GRA-OVA15-60.

The increase in impact velocity shown in Fig. 4.17 illustrates the evolution of the von Mises equivalent stress and the damage to the 30° sharp particle. The first column of Fig. 4.17 shows the von Mises equivalent stress values at the moment of impact in frame 21, while the second column shows in frame 25. In view of this, it is possible to observe the shape of the stress distribution in the projectile and the displacement of the critical stress according to the evolution of the evaluated frame. It is important to emphasize that when evaluating the equivalent von Mises stress in frame 25, the numerical values are lower than the value of frame 21 at the speed of 20m/s, and higher at the other speeds. The increase in speed causes significant damage to the material. From a speed of 10m/s, the projectile goes through the shattering process and the material is not completely damaged in any of the conditions.

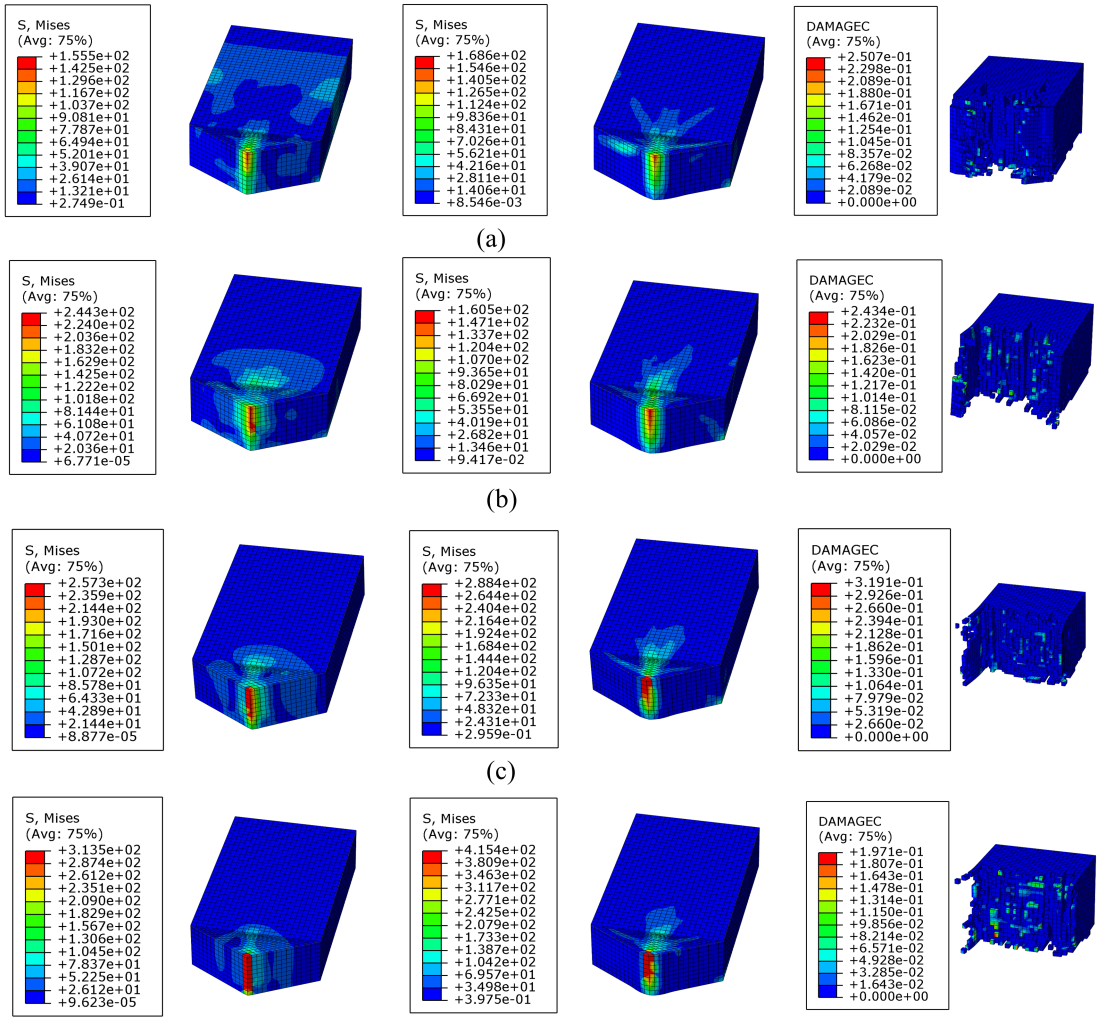

Figure 4.17: In the first column the equivalent von Mises stresses in the impact frame 21 are presented, in the second column in frame 25 and in the last column the final damage of the material under conditions. (a) GRA-SRP30-10 (b) GRA-SRP30-20 (c) GRA-SRP30-40 (d) GRA-SRP30-60.

The increase in impact velocity shown in Fig. 4.18 illustrates the evolution of the von Mises equivalent stress and the damage to the 45° sharp particle. The first column of Fig. 4.18 shows the von Mises equivalent stress values at the moment of impact in frame 21, while the second column shows in frame 25. In view of this, it is possible to observe the shape of the stress distribution in the projectile and the displacement of the critical stress according to the evolution of the evaluated frame. It is important to emphasize that when evaluating the equivalent von Mises stress in frame 25, the numerical values are higher than the value in frame 21. The increase in speed causes significant damage to the material. From a speed of 10m/s, the projectile goes through the shattering process and the material is not completely damaged in any of the conditions.

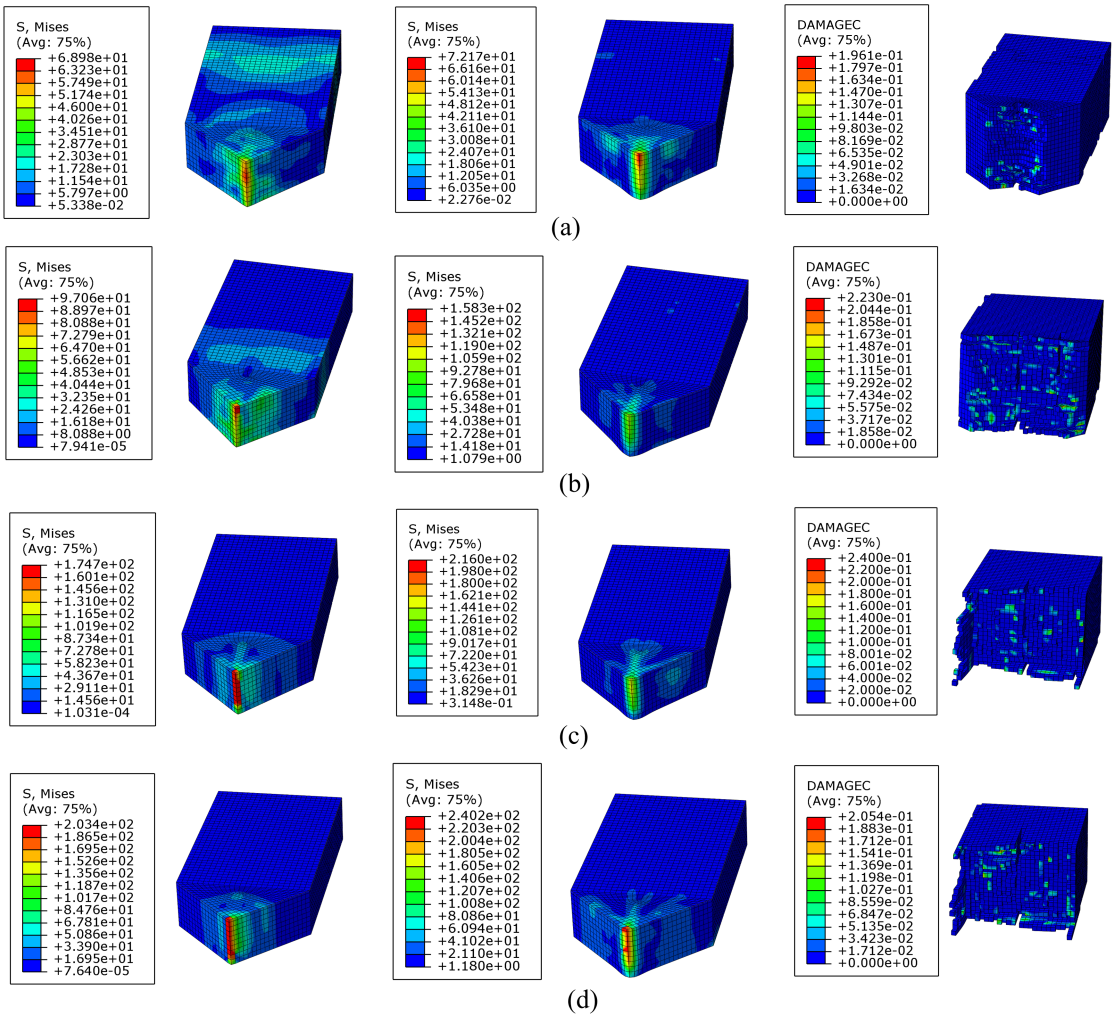

Figure 4.18: In the first column the equivalent von Mises stresses in the impact frame 21 are presented, in the second column in frame 25 and in the last column the final damage of the material under conditions. (a) GRA-SRP45-10 (b) GRA-SPR45-20 (c) GRA-SRP45-40 (d) GRA-SRP45-60.

4.2 Quantitative analysis

In order to understand the behavior of the impact model between a projectile and a flat counterpart, an impact study of six different geometries is carried out, applying four impact velocities (10m/s, 20m/s, 40m/s and 60m/s) and varying the projectile material (concrete, granite and arenite). In order to better understand the behavior of each geometry, the film analogy was used, evaluating three video frames with strategic times so that the first frame is evaluated right at the moment of contact, while the second frame was evaluated 4 frames after contact and the third frame was evaluated after contact, that is, 9 frames after contact.

4.2.1 Sphere 7.5mm quantitative analysis

The first geometry to be analyzed was the 7.5 mm diameter sphere projectile. The results for this configuration are shown in Fig. 4.19. Fig. 4.19(a) represents the von Mises equivalent stress distribution of the projectile for the three types of materials analyzed (concrete, granite and arenite), it is important to evaluate Fig. 4.19(a) concomitantly with Fig. 4.20(a), which represents the contact pressure, and Fig. 4.21(a), which presents the equivalent plastic deformation. Note that the three materials analyzed did not have similar curves in frame 21, considering that at this moment the impact velocity reduction process is occurring due to the collision, consequently the transformation of the projectile's kinetic energy into internal energy is taking place (deformation energy). For this reason, the aforementioned graphics are disconnected and have different behaviors. When evaluating frames 25 and 30, shown in Fig's 4.19, 4.20 and 4.21, the stabilization of the contact area is noted, which allows for the identification of the impact behavior of the Ø7.5mm projectile, considering that the graphics have greater connections and similarities.

After evaluating the results observed in Fig's 4.19, 4.20 and 4.21, it was noted that after the stabilization of the contact area, the projectile impacting on the flat counterpart:

- An impact velocity of 10m/s generated very close projectile contact stresses and pressures for both types of materials, except granite, as well as for equivalent plastic strain values. However, it was found that the granite projectile was less damaged than the other materials. The granite projectile generated greater stresses in the metallic flat counterpart, consequently greater plastic deformations, but did not generate significant damage. The arenite and concrete projectiles did not generate deformations equivalent to the one observed in the flat counterparts.

- An impact velocity of 20m/s where it was found that the three materials had different stresses in the projectiles. However, the contact pressures generated were close for the three types of materials, as well as the plastic deformation. The equivalent stress in the granite projectile is still higher compared to other materials. The granite projectile generated greater stresses in the metallic flat counterpart, as well as greater equivalent deformations. The arenite and concrete projectiles did not generate deformations equivalent to the one observed in the flat counterparts at this impact velocity.

- An impact velocity of 40m/s where it was found that the three materials had different stresses in the projectiles. The equivalent stress in the concrete projectile is lower compared to other materials, because at this speed the concrete material is completely shattered with a damage percentage of 100. The tension generated in the projectile by arenite is higher than that of granite. The granite projectile generated greater stresses in the metallic flat counterpart, as well as greater equivalent deformations. The arenite and concrete projectiles did not generate deformations equivalent to the one observed in the flat counterparts at this impact velocity.

- A speed of 60m/s generated different stresses and strains for the three types of materials, with granite generating higher stresses for the projectile and granite generating higher stresses and strains for the flat counterpart. However, all three types of materials go through a chipping process and the materials are completely damaged.

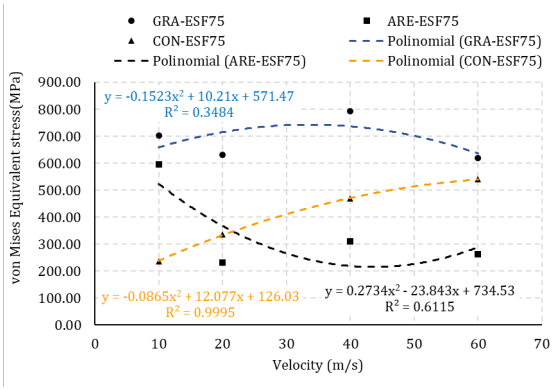

(a)

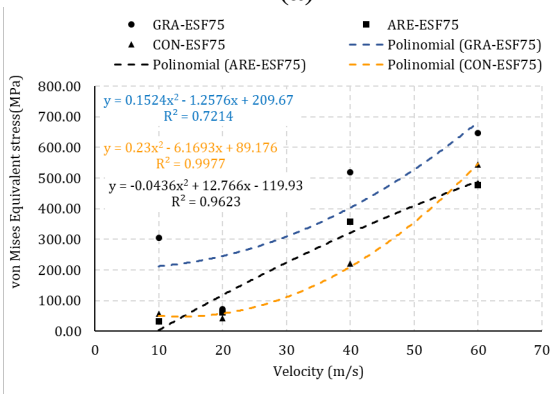

(b)

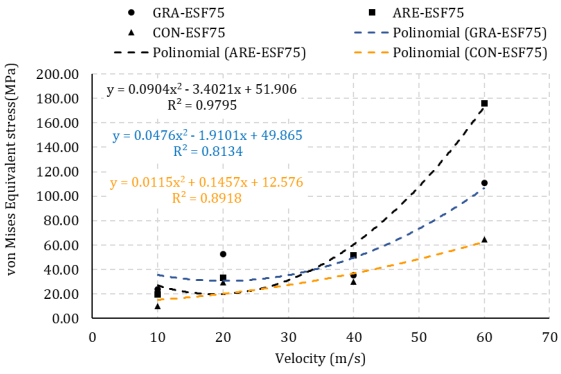

(c)

Figure 4.19: Equivalent von Mises Stress versus Velocity in (a) Frame 21 (b) Frame 25 (c) Frame 30

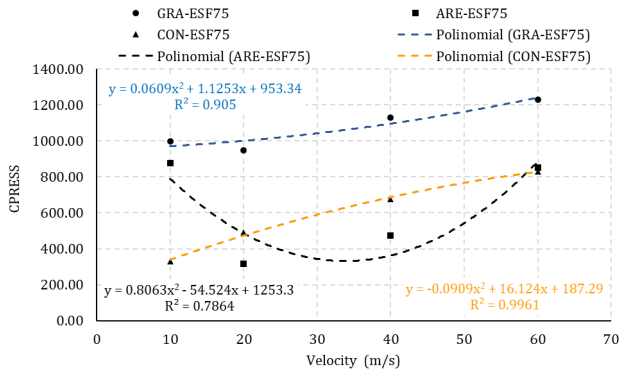

(a)

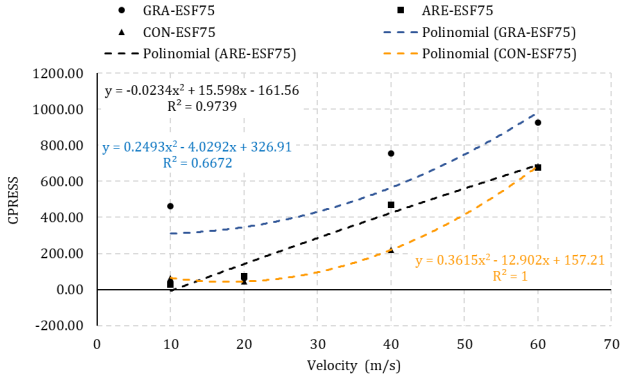

(b)

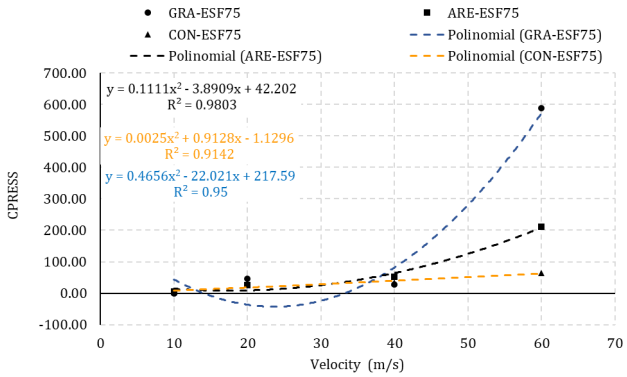

(c)

Figure 4.20: Contact pressure (CPRESS) versus Speed in (a) Frame 21 (b) Frame 25 (c) Frame 30

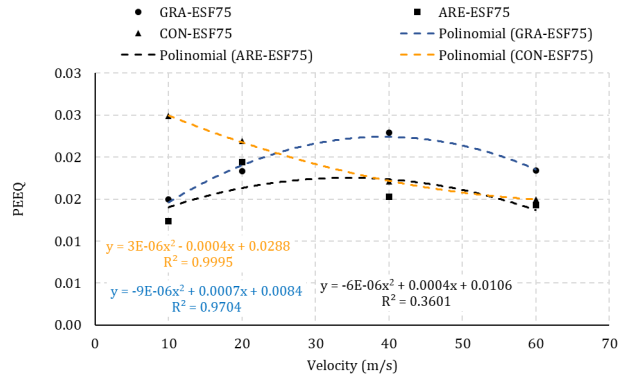

(a)

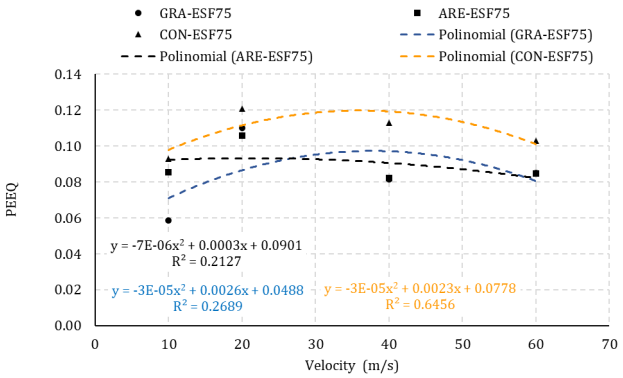

(b)

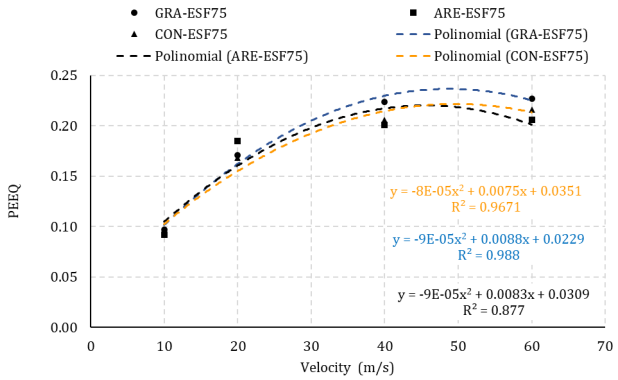

(c)

Figure 4.21: Equivalent plastic deformation (PEEQ) versus Speed in (a) Frame 21 (b) Frame 25 (c) Frame 30

4.2.2 Sphere 15mm quantitative analysis

The second geometry to be analyzed was the sphere projectile with a diameter of 15mm. The results for this configuration are shown in Fig. 4.22. Fig. 4.22(a) represents the von Mises equivalent stress distribution of the projectile for the three types of materials analyzed (concrete, granite and arenite), it is important to evaluate Fig. 4.22(a) concomitantly with Fig. 4.23(a), which represents the contact pressure, and Fig. 4.24(a), which presents the

equivalent plastic deformation. Note that the three materials analyzed did not have similar curves in frame 21, considering that at this moment the impact velocity reduction process is occurring due to the collision, consequently the transformation of the projectile's kinetic energy into internal energy is taking place (deformation energy). For this reason, the aforementioned graphics are disconnected and have different behaviors. When evaluating frames 25 and 30, shown in Fig's 4.22, 4.23 and 4.24, the stabilization of the contact area can be seen, which allows for the identification of the impact behavior of the Ø 15 mm projectile, considering that the graphics present larger connections and similarities.

After evaluating the results observed in Fig.s 4.22, 4.23 and 4.24, it was noted that after the stabilization of the contact area, the projectile impacting on the flat counterpart:

- An impact velocity of 10m/s generated very close projectile contact stresses and pressures for both types of materials, with the exception of arenite. As for plastic deformation, concrete differs from others with lower values. However, it was found that the granite projectile was less damaged than the other materials. The granite projectile generated greater stresses in the metallic flat counterpart, consequently greater plastic deformations, but did not generate significant damage. The arenite and concrete projectiles did not generate deformations equivalent to the one observed in the flat counterparts.

- An impact speed of 20m/s it was found that the two materials had simmilar stresses in the projectiles, with the exception of the concrete that generated less stress, as well as lower contact pressure, because at this speed the concrete material has more 80 percent damaged. However, the contact pressures generated were different for the three types of materials, unlike the plastic deformation, which were similar for arenite and granite, whereas for concrete it was much higher. The equivalent stress in the arenite projectile is higher compared to other materials. The granite projectile generated greater stresses in the metallic flat counterpart, as well as greater equivalent deformations. The arenite and concrete projectiles did not generate deformations equivalent to the one observed in the flat counterparts at this impact velocity.

- An impact velocity of 40m/s it was found that the three materials had different stresses in the projectiles. The equivalent stress in the concrete projectile is lower compared to other materials, because at this speed the concrete material is completely shattered with a damage percentage of 100 percent. The tension generated in the projectile by arenite is higher than that of granite. The granite projectile generated greater stresses in the metallic flat counterpart, as well as greater equivalent deformations. The arenite and concrete projectiles did not generate deformations equivalent to the one observed in the flat counterparts at this impact velocity.

- A speed of 60m/s generated different stresses and strains for the three types of materials, with granite generating higher stresses for the projectile and granite generating

higher stresses and strains for the flat counterpart. However, all three types of materials go through a chipping process and the materials are almost completely damaged.

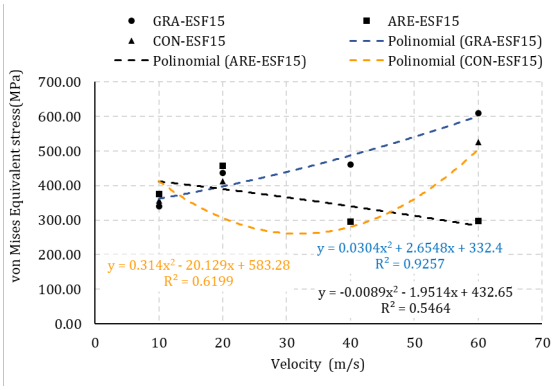

(a)

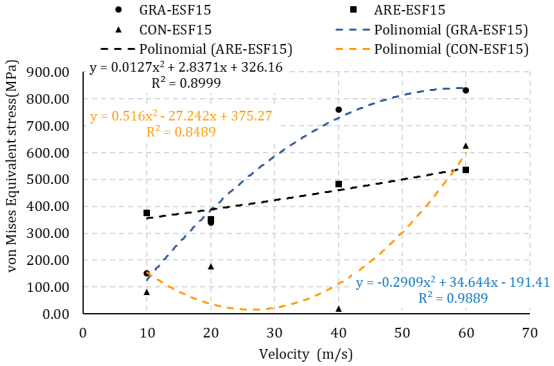

(b)

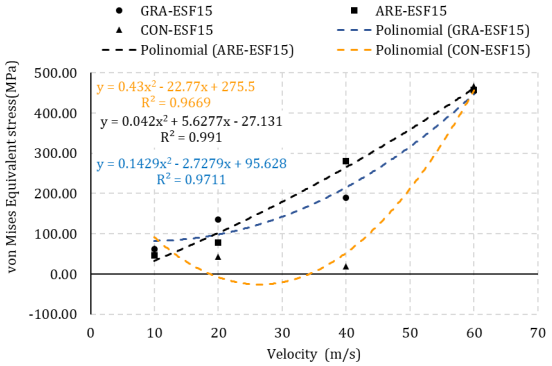

(c)

Figure 4.22: Equivalent von Mises Stress versus Speed in (a) Frame 21 (b) Frame 25 (c) Frame 30

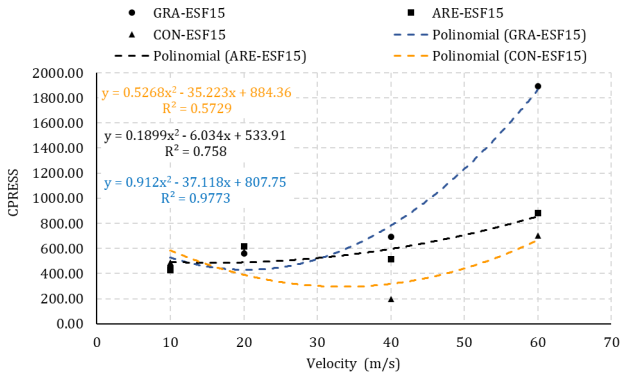

(a)

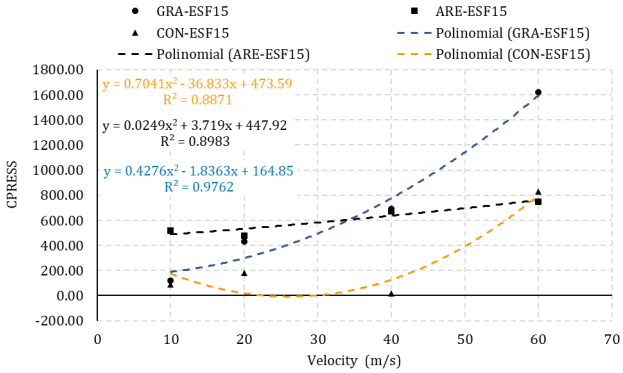

(b)

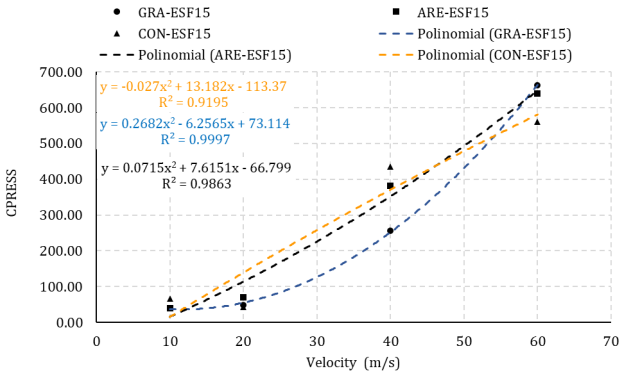

(c)

Figure 4.23: Contact pressure (CPRESS) versus Speed in (a) Frame 21 (b) Frame 25 (c) Frame 30

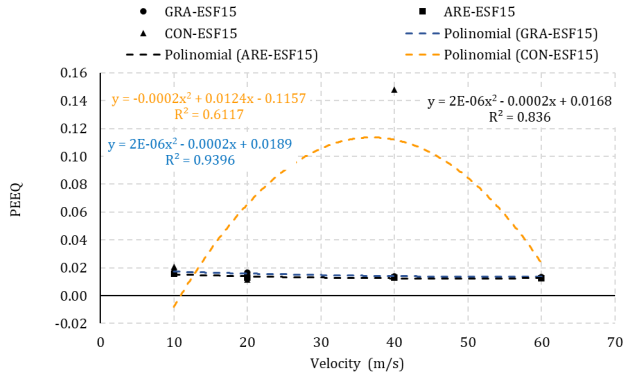

(a)

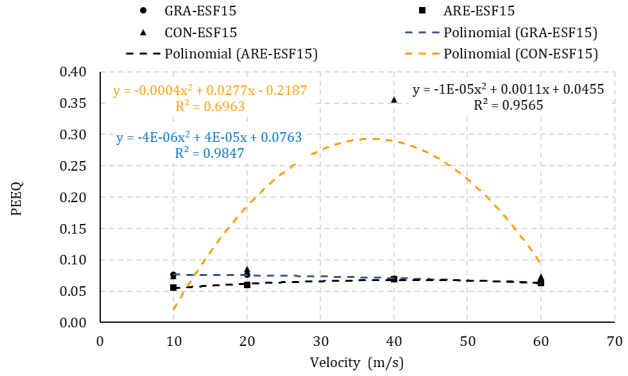

(b)

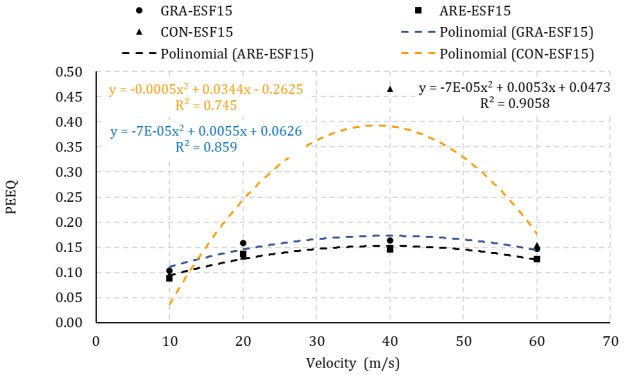

(c)

Figure 4.24: Equivalent plastic deformation (PEEQ) versus Velocity in (a) Frame 21 (b) Frame 25 (c) Frame 30

4.2.3 Sharp 30° quantitative analysis

The third geometry to be analyzed was the sharp 30° projectile. The results for this configuration are shown in Fig. 4.25. Fig. 4.25(a) represents the von Mises equivalent stress distribution of the projectile for the three types of materials analyzed (concrete, granite and arenite), it is important to evaluate Fig. 4.25(a) concomitantly with Fig. 4.26(a), which represents the contact pressure, and Fig 4.27(a) which presents the equivalent plastic defor-

mation. Note that the three materials analyzed did not have similar curves in frame 21, considering that at this moment the impact velocity reduction process is occurring due to the collision, consequently the transformation of the projectile's kinetic energy into internal energy is taking place (deformation energy). For this reason, the aforementioned graphics are disconnected and have different behaviors. When evaluating frames 25 and 30, shown in Fig's. 4.25, 4.26 and 4.27, the stabilization of the contact area is noted, which allows for the identification of the impact behavior of the 30° sharp projectile, given that the graphs present larger connections and similarities.

After evaluating the results observed in Fig's 4.25, 4.26 and 4.27, it was noted that after the stabilization of the contact area, the projectile impacting on the flat counterpart:

- An impact speed of 10m/s generated stresses, strains and contact pressures in the projectiles very close for both types of materials, with the exception of concrete, which has lower values. However, it was found that the granite projectile was less damaged than the other materials. The granite projectile generated greater stresses in the metallic flat counterpart, consequently greater plastic deformations, but did not generate significant damage. The arenite and concrete projectiles did not generate deformations equivalent to the one observed in the flat counterparts.

- An impact velocity of 20m/s it was found that the two materials had different stresses in the projectiles. Concrete generated less stress and deformation, as well as less contact pressure. However, the contact pressures generated were similar for both types of materials, with the exception of concrete. Unlike plastic deformation that were distinct for the three materials. The equivalent stress in the arenite projectile is higher compared to other materials. The granite projectile generated greater stresses in the metallic flat counterpart, as well as greater equivalent deformations. The arenite and concrete projectiles did not generate deformations equivalent to the one observed in the flat counterparts at this impact velocity.

- An impact velocity of 40m/s it was found that the two materials had similar stresses in the projectiles, with the exception of arenite. The equivalent stress and contact pressure in the arenite projectile are higher compared to other materials. The granite projectile generated greater stresses in the metallic flat counterpart, but the concrete projectile generated greater equivalent deformations. The arenite and concrete projectiles generated deformations equivalent to the one observed in the flat counterparts at this impact velocity.

- A speed of 60m/s generated different stresses and strains for the three types of materials, with concrete generating higher stresses for the projectile and granite generating higher stresses and strains for the flat counterpart. However, the concrete geometry undergoes a chipping process and the material is completely damaged. Unlike other geometries that still have about 20 percent of the material.

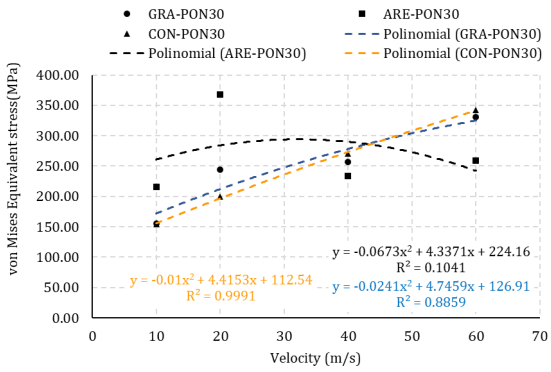

(a)

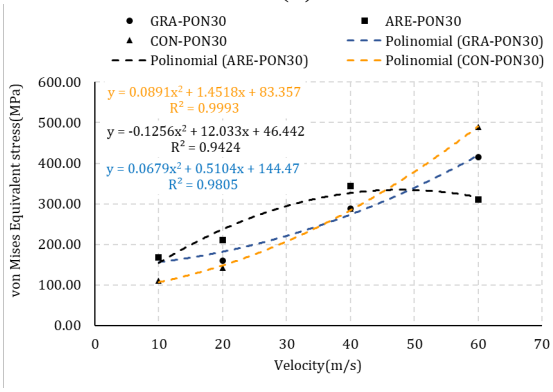

(b)

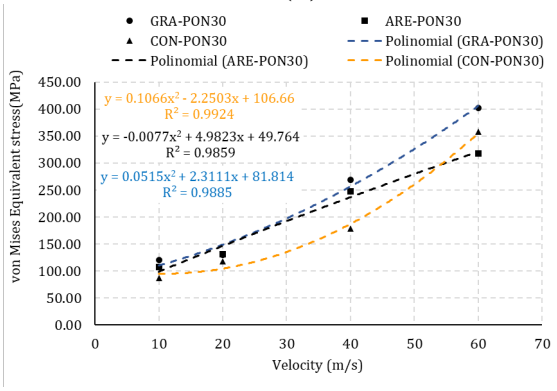

(c)

Figure 4.25: Equivalent von Mises Stress versus Speed in (a) Frame 21 (b) Frame 25 (c) Frame 30

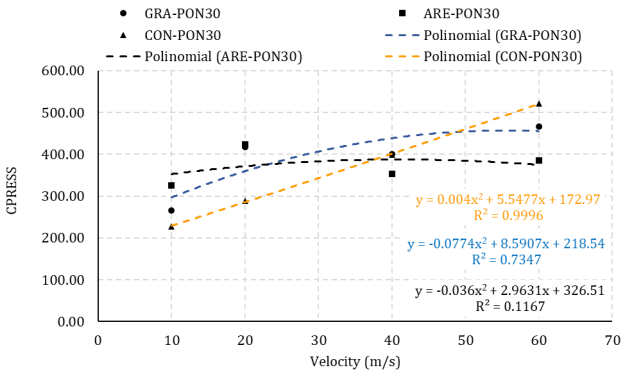

(a)

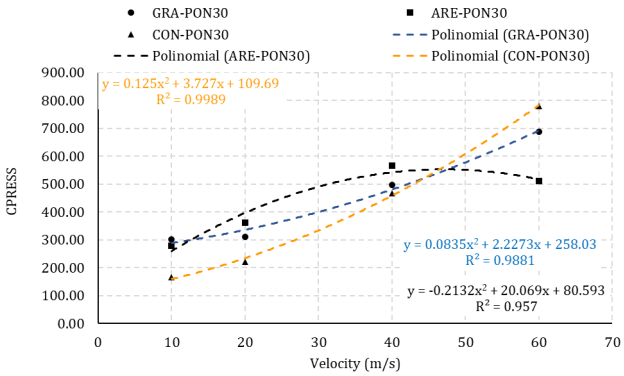

(b)

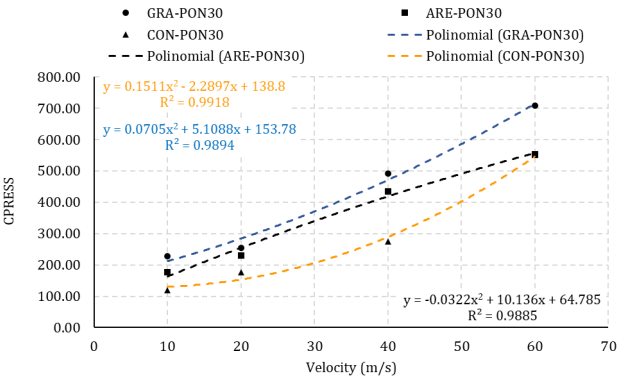

(c)

Figure 4.26: Contact pressure (CPRESS) versus Speed in (a) Frame 21 (b) Frame 25 (c) Frame 30.

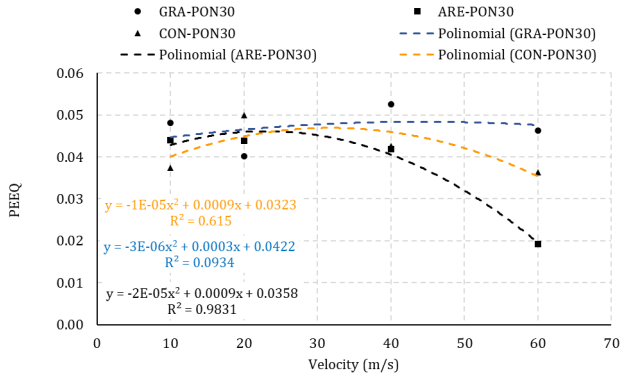

(a)

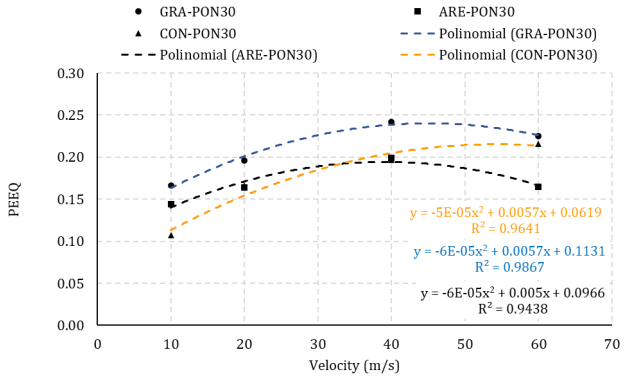

(b)

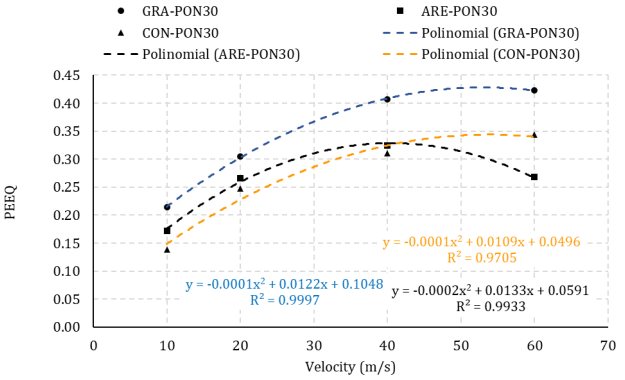

(c)

Figure 4.27: Equivalent plastic deformation (PEEQ) versus Velocity in (a) Frame 21 (b) Frame 25 (c) Frame 30.

4.2.4 Sharp 45° quantitative analysis

The fourth geometry to be analyzed was the 45° sharp projectile. The results for this configuration are shown in Fig. 4.28. Fig. 4.28(a) represents the von Mises equivalent stress graph of the projectile for the three types of materials analyzed (concrete, granite and arenite), it is important to evaluate graph 4.28(a) concomitantly with Fig. 4.29(a), which represents the contact pressure, and Fig. 4.30(a) which presents the equivalent plastic defor-

mation. Note that the three materials analyzed did not have similar curves in frame 21, considering that at this moment the impact velocity reduction process is occurring due to the collision, consequently the transformation of the projectile's kinetic energy into internal energy is taking place (deformation energy). For this reason, the aforementioned graphics are disconnected and have different behaviors. When evaluating frames 25 and 30, shown in Fig. 4.28, 4.29 and 4.30, the stabilization of the contact area is noted, which allows for the identification of the impact behavior of the 45° sharp projectile, considering that the graphs present larger connections and similarities.

After evaluating the results observed in the Fig's 4.28, 4.29 and 4.30, it was noted that after the stabilization of the contact area, the projectile impacting on the flat counterpart:

- An impact velocity of 10m/s generated very different stresses, strains and contact pressures in the projectiles for the three types of materials, with higher stresses and contact pressures in the arenite. Granite provides greater plastic deformation and less arenite among the analyzed geometries. However, it was found that the granite projectile was less damaged than the other materials.

- An impact velocity of 20m/s it was found that the three materials had different stresses in the projectiles. arenite generated greater stress and deformation, and arenite generated greater contact pressure. However, the contact pressures generated were different for the three types of materials. The arenite projectile generated greater stresses in the metallic flat counterpart, as well as greater equivalent deformations. The arenite and granite projectiles did not generate deformations equivalent to the one observed in the flat counterparts at this impact velocity. The three projectiles generated deformations equivalent to the one observed in the flat counterparts after this speed.

- An impact velocity of 40m/s it was found that the three materials had different stresses in the projectiles. The equivalent stress and contact pressure in the arenite projectile are higher compared to other materials. The granite, arenite and concrete projectiles generated similar stresses in the metallic flat counterpart, but the arenite projectile generated greater equivalent deformations.

- A speed of 60m/s generated different stresses and strains for the three types of materials, with concrete generating higher stresses and contact pressures for the projectile and granite generating higher strains. The three geometries produced stresses and strains for the metallic flat counterpart, and the concrete generated greater strains. However, the concrete geometry undergoes a chipping process and the material is completely damaged. Unlike other geometries that still have about 15 percent of the material.

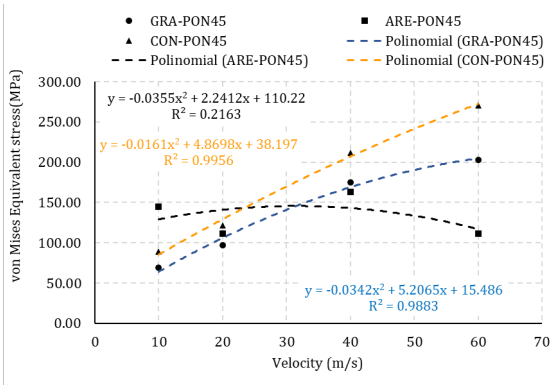

(a)

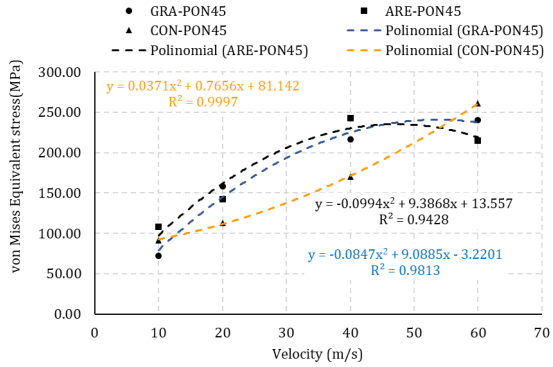

(b)

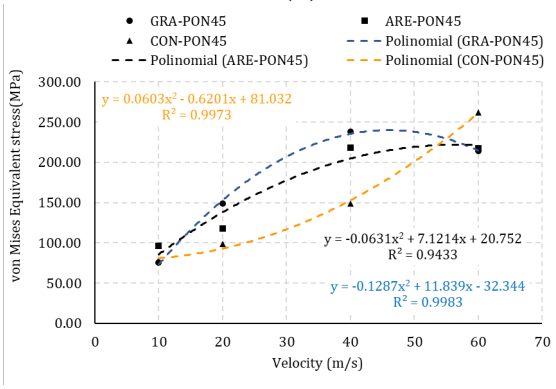

(c)

Figure 4.28: Equivalent von Mises Stress versus Speed in (a) Frame 21 (b) Frame 25 (c) Frame 30

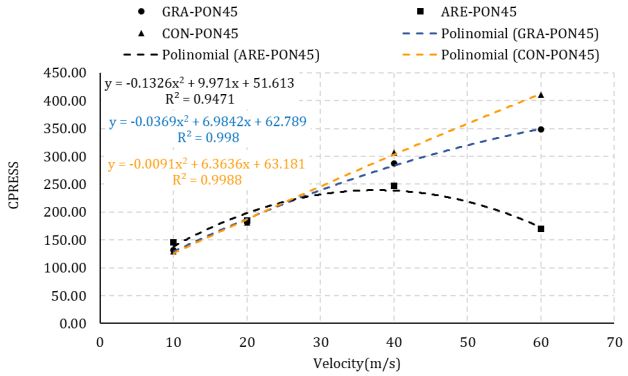

(a)

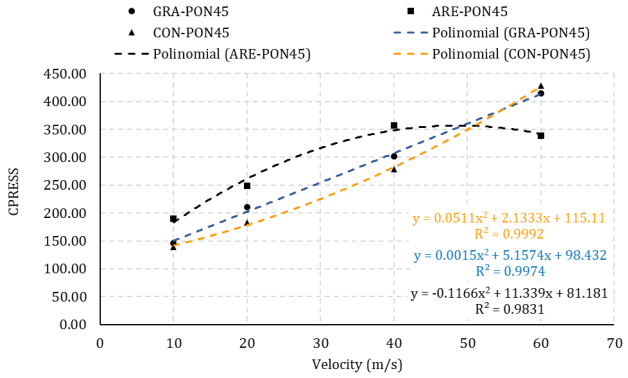

(b)

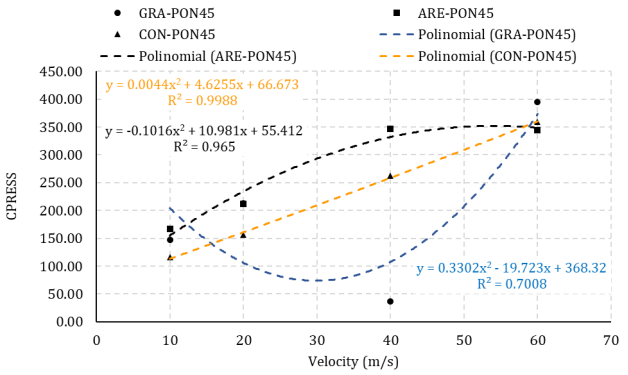

(c)

Figure 4.29: Contact pressure (CPRESS) versus Speed in (a) Frame 21 (b) Frame 25 (c) Frame 30

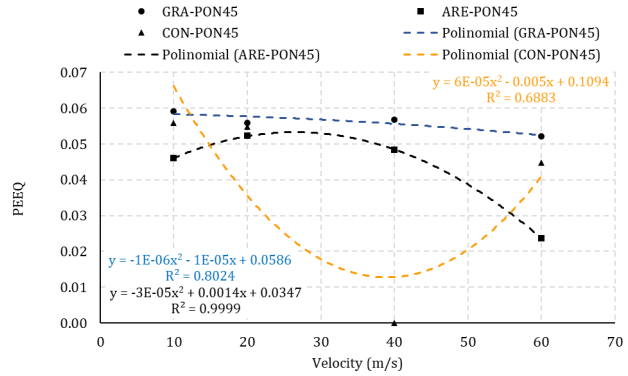

(a)

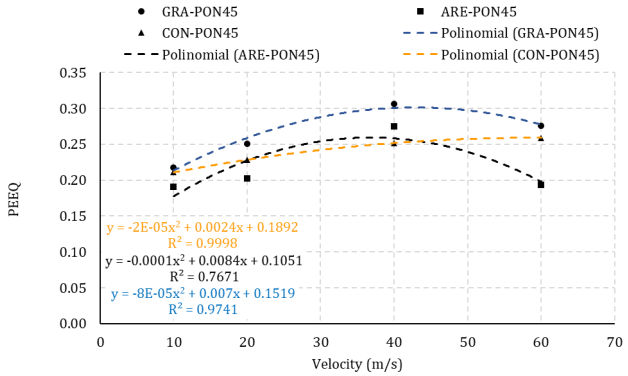

(b)

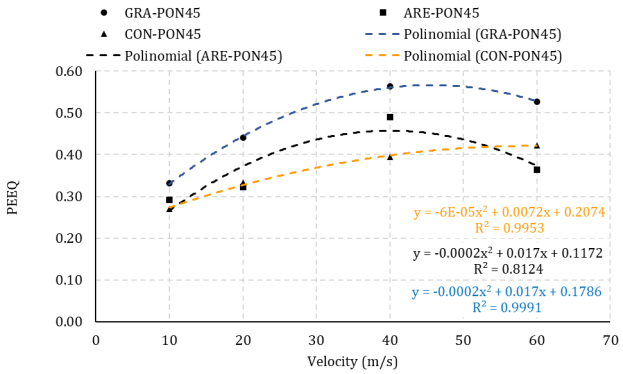

(c)

Figure 4.30: Equivalent plastic deformation (PEEQ) versus Velocity in (a) Frame 21 (b) Frame 25 (c) Frame 30

4.2.5 Oval 7.5mm quantitative analysis

The fifth geometry to be analyzed was the Ø7.5mm oval projectile. The results for this configuration are shown in Fig. 4.31. Fig. 4.31(a) represents the von Mises equivalent stress distribution of the projectile for the three types of materials analyzed (concrete, granite and arenite), it is important to evaluate Fig. 4.31(a) concomitantly with Fig. 4.32(a), which represents the contact pressure, and Fig. 4.33(a) which presents the equivalent plastic defor-

mation. Note that the three materials analyzed did not have similar curves in frame 21, considering that at this moment the impact velocity reduction process is occurring due to the collision, consequently the transformation of the projectile's kinetic energy into internal energy is taking place (deformation energy). For this reason, the aforementioned graphics are disconnected and have different behaviors. When evaluating frames 25 and 30, shown in Fig's 4.31, 4.32 and 4.33, the stabilization of the contact area is noted, which allows for the identification of the impact behavior of the Ø7.5mm oval projectile, considering that the graphics have greater connections and similarities.

After evaluating the results observed in Fig's.4.31, 4.32 and 4.33, it was noted that after the stabilization of the contact area, the projectile impacting on the flat counterpart:

- An impact speed of 10m/s generated very different stresses, strains and contact pressures in the projectiles for the three types of materials, with higher stresses and contact pressures in the granite. Granite provides greater plastic deformation and smaller concrete among the analyzed geometries. However, it was found that the granite projectile was less damaged than the other materials. The three geometries generate stresses in the flat counterpart, but do not produce plastic deformations at any of the speeds.
- An impact velocity of 20m/s it was found that the three materials remained with different stresses in the projectiles, and the granite producing higher stresses, strains and contact pressures.
- An impact velocity of 40m/s the three materials were found to have similar stresses in the concrete and arenite projectiles. The equivalent stress and contact pressure in the concrete projectile are higher compared to other materials. arenite and concrete projectiles generated similar stresses in the metallic flat counterpart.
- A velocity of 60m/s the granite generated higher stresses and contact pressures for the projectile. arenite, on the other hand, generated greater deformations, considering that it was more than 90 percent damaged.

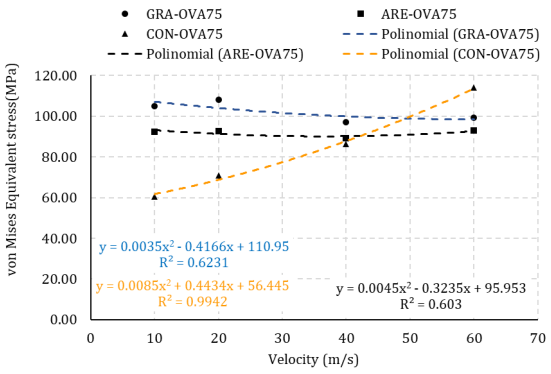

(a)

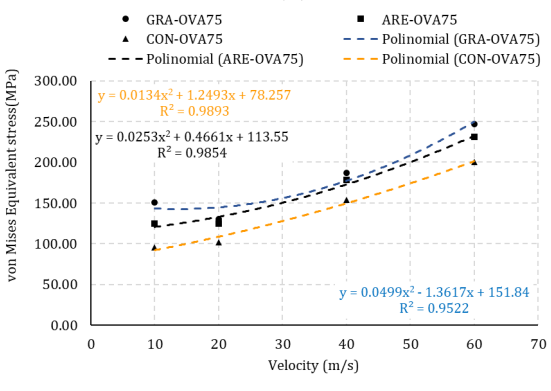

(b)

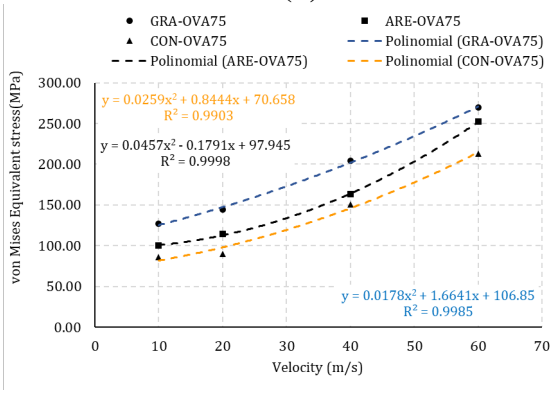

(c)

Figure 4.31: Equivalent von Mises Stress versus Speed in (a) Frame 21 (b) Frame 25 (c) Frame 30

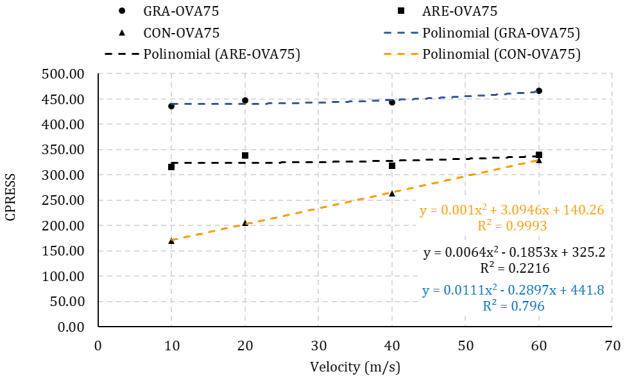

(a)

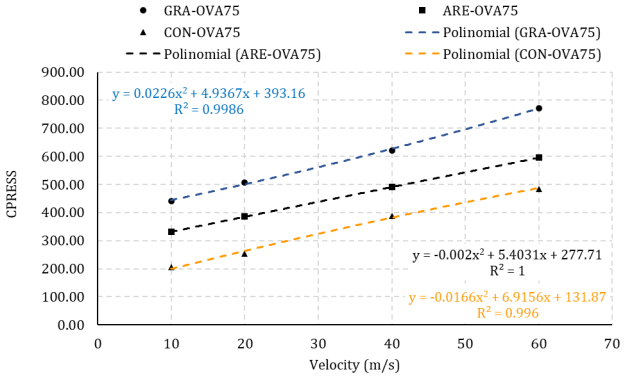

(b)

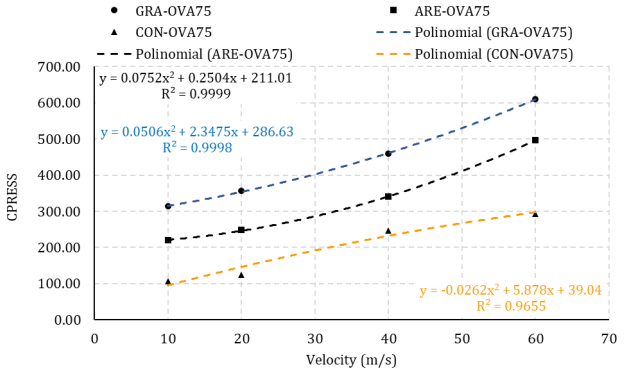

(c)

Figure 4.32: Contact pressure (CPRESS) versus Speed in (a) Frame 21 (b) Frame 25 (c) Frame 30

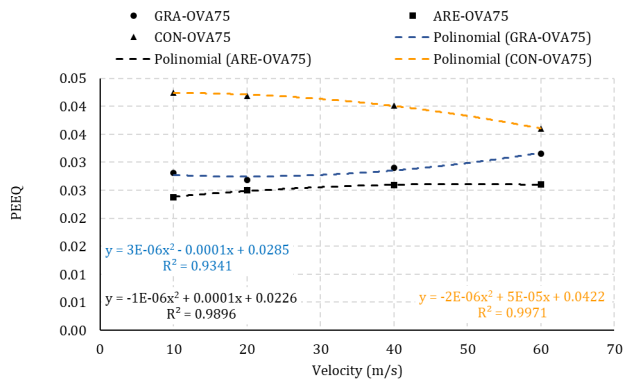

(a)

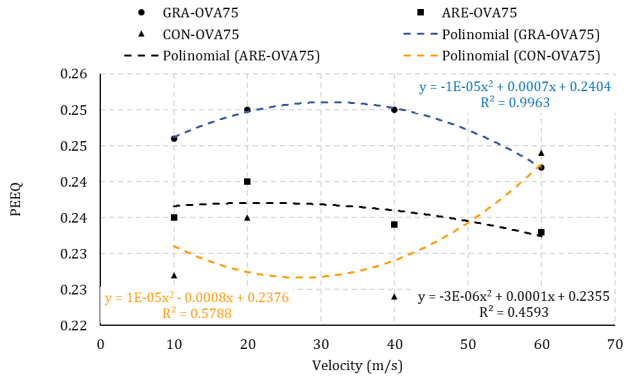

(b)

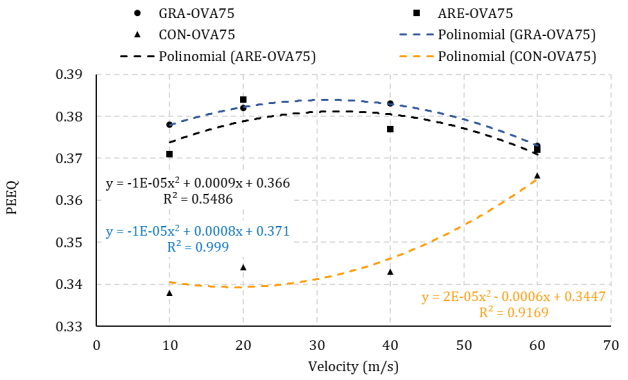

(c)

Figure 4.33: Equivalent plastic deformation (PEEQ) versus Velocity in (a) Frame 21 (b) Frame 25 (c) Frame 30.

4.2.6 Oval 15mm quantitative analysis

The sixth geometry to be analyzed was the Ø15mm oval projectile, the results for this configuration are shown in Fig. 4.34. Fig. 4.34(a) represents the von Mises equivalent stress graph of the projectile for the three types of materials analyzed (concrete, granite and arenite), it is important to evaluate Fig. 4.34(a) concomitantly with Fig. 4.35(a) which represents the contact pressure and Fig. 4.36(a) which presents the equivalent plastic deformation. Note

that the three materials analyzed did not have similar curves in frame 21, considering that at this moment the impact velocity reduction process is occurring due to the collision, consequently the transformation of the projectile's kinetic energy into internal energy is taking place (deformation energy). For this reason, the aforementioned graphics are disconnected and have different behaviors. When evaluating frames 25 and 30, shown in Fig's. 4.34, 4.35 and 4.36, we noticed the stabilization of the contact area, which allows us to identify the behavior of the impact of the Ø 15 mm oval projectile, considering that the graphics have greater connections and similarities.

After evaluating the results observed in Fig's. 4.34, 4.35 and 4.36, it was noted that after the stabilization of the contact area, the projectile impacting on the flat counterpart:

- An impact speed of 10m/s generated very different stresses, strains and contact pressures in the projectiles for the three types of materials, with higher stresses and contact pressures in the granite. Granite provides greater plastic deformation and smaller concrete among the analyzed geometries. However, it was found that the granite projectile was less damaged than the other materials. The three geometries generate stresses in the flat counterpart, but the arenite and concrete projectile does not produce plastic deformations.

- An impact velocity of 20m/s it was found that the three materials remained with different stresses in the projectiles, and the arenite producing higher stresses and strains. Granite, on the other hand, produces greater plastic deformations. The three geometries generate stresses in the flat counterpart, but the arenite and concrete projectile does not produce plastic deformations.

- An impact velocity of 40m/s the two materials were found to have similar stresses and contact pressures in the granite and arenite projectiles. The concrete projectile produced greater plastic deformations, considering that the concrete geometry undergoes a chipping process and the material is completely damaged. The three geometries generate stresses and strains in the metallic flat counterpart.

- At a speed of 60m/s, the granite generated greater stresses and strains. arenite, on the other hand, generated greater contact pressures, since it undergoes a chipping process and the material is completely damaged.

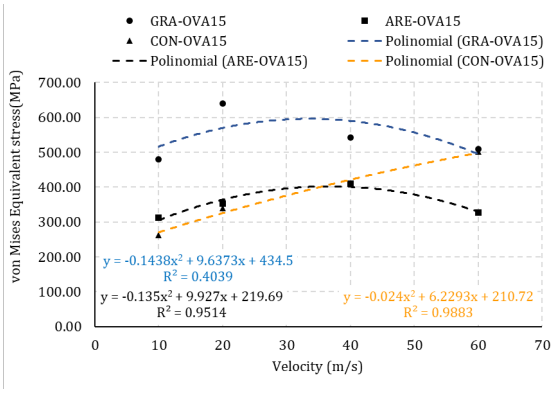

(a)

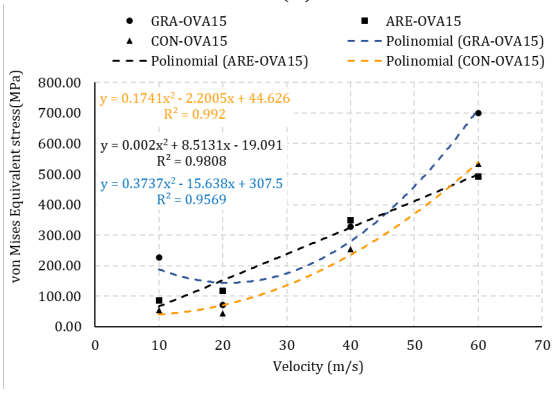

(b)

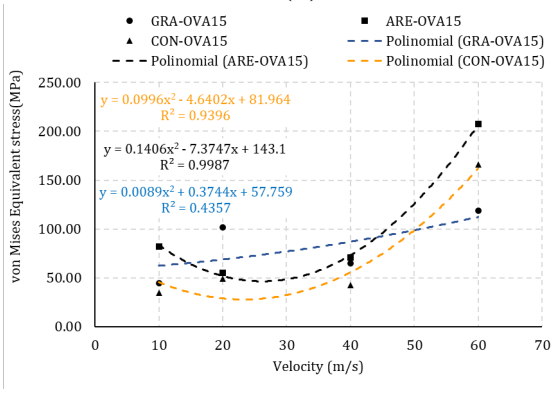

(c)

Figure 4.34: Equivalent von Mises Stress versus Speed in (a) Frame 21 (b) Frame 25 (c) Frame 30

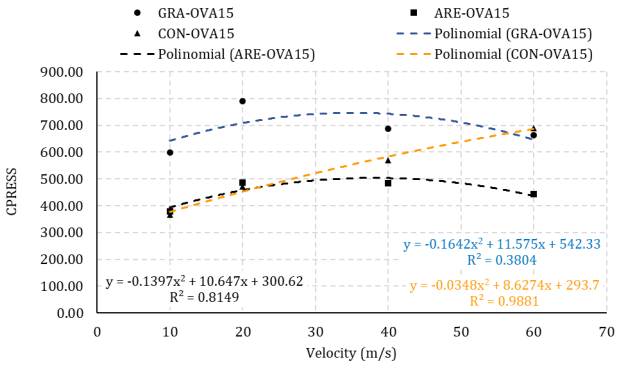

(a)

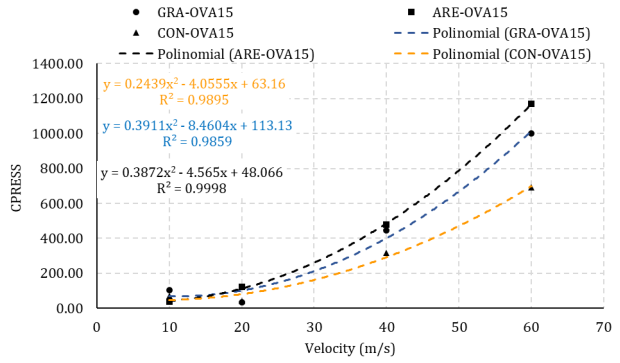

(b)

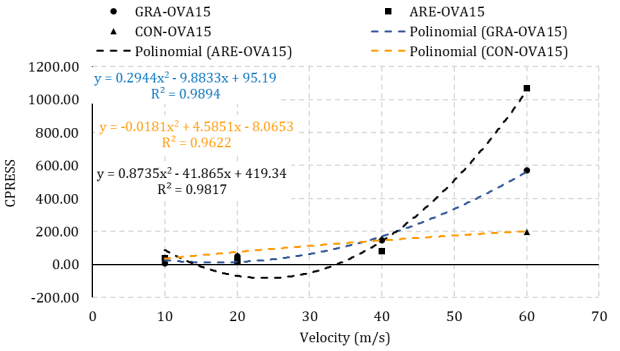

(c)

Figure 4.35: Contact pressure (CPRESS) versus Speed in (a) Frame 21 (b) Frame 25 (c) Frame 30

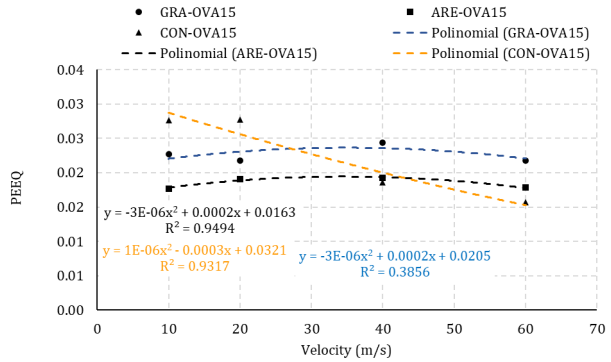

(a)

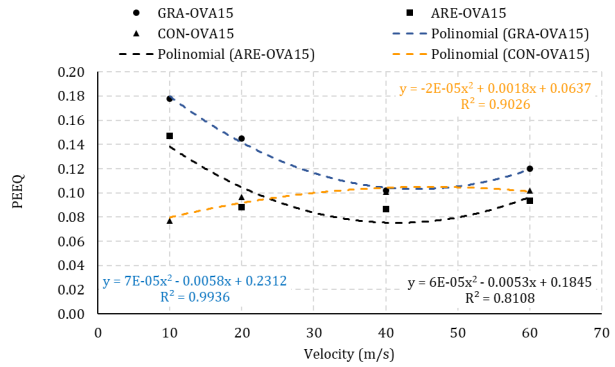

(b)

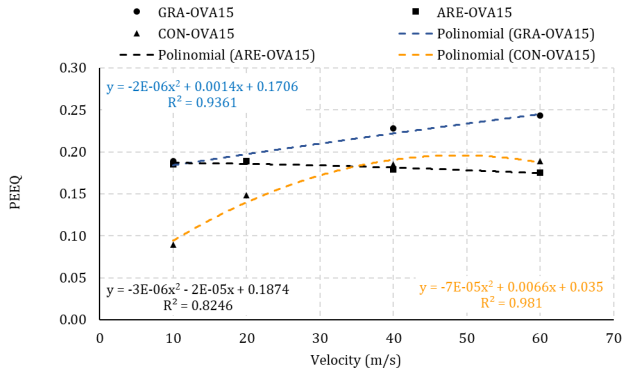

(c)

Figure 4.36: Equivalent plastic deformation (PEEQ) versus Velocity in (a) Frame 21 (b) Frame 25 (c) Frame 30

Chapter 5

CONCLUSION

This chapter describes the conclusions of the numerical simulations of six different geometries, with three types of materials, varying the impact velocity on the target material with metallic properties.

5.1 Main observations

This work presents a study on the fracture behavior of brittle rock projectiles when impacting on a metallic flat counterpart. Three types of materials, six geometries and four different velocities were analysed. The numerical model was validated by comparing the impact of some geometries with the Hertz formulae. The variables investigated were equivalent stresses, strains and damage on both the flat counterpart and the projectile. The contact interface regions between the geometries shows high concentration of stresses, inelastic strains and degradation. For a better evaluation and validation of the data, more refined meshes were used in the impact area.

By evaluating the quantitative items concomitantly with the qualitative items, it was possible to infer that the projectiles geometry, the impact velocity and the type of materials used directly influence the damage of the metallic flat counterpart and of the projectiles during the impact. Therefore, it was found that the granite projectile, being a less porous material and with greater mechanical strength, is the material that produces the highest stresses and deformations to the flat counterpart, and is also the one that is least damaged in all the analyzed geometries, when compared to concrete and arenite. It is also noticed that the increase in impact velocity is not a guarantee of greater deformations for the flat counterpart, as it was noticed that the increase in velocity significantly increases the damage of the projectiles. In view of this, it was found that the most critical geometry for the flat counterpart are the sharp projectiles, as they generate greater impact stresses and greater plastic deformations equivalent to the metallic flat counterpart.

The behaviors of concrete, granite and arenite are non-linear and are well represented

by the Concrete Damaged Plasticity Model. This model represents the real behaviors of the materials analyzed, considering the damage and loss of stiffness of the material with the increase in impact velocity.

The behavior of the metallic flat counterpart is linear and is well represented by the Johnson-Cook model. This model describes the real behavior of the metallic flat counterpart during the impact of the analyzed geometries, however, the velocity conditions, geometries and materials of the projectile did not generate significant damage and deformation to the flat counterpart.

5.2 Future work proposals

For the elaboration of future works, it is proposed the implementation of experimental studies for comparison with the values obtained in the computational simulations with proposals for the optimization of the target material. Hold on to follow the following steps:

- The elaboration of concrete, granite, arenite and metallic specimens;
- Tests in laboratories for impact tests;
- Experimentally validate the results obtained in computer simulations;
- Implement methodology for optimizing the target material;
- Implement this methodology in other industrial and engineering applications, such as the real case of cutters, ballistic impacts, vehicle and aircraft collisions;
- Implement erosive wear;
- Implement the analysis of each variable that influence erosive wear.

Considering that energy transformation occurs when the projectile impacts the flat counterpart at a speed, that is, the kinetic energy is transformed into internal energy (deformation energy), it is recommended that the amount of energy is evaluated and quantified dissipated for each phase of the process.

Considering that energy transformation occurs when the projectile impacts the flat counterpart at a speed, that is, the kinetic energy is transformed into internal energy (deformation energy), it is recommended that the amount of energy is evaluated and quantified dissipated for each phase of the process.

Considering that energy transformation occurs when the projectile impacts the flat counterpart at a speed, that is, the kinetic energy is transformed into internal energy (deformation energy), it is recommended that the amount of energy is evaluated and quantified dissipated for each phase of the process.

Advances in technology have brought us great advances in understanding the behavior of phenomena, especially erosive wear, which has been extensively studied due to its complexity. The phenomenon refers to the degradation of materials that includes industrial problems on a recurring basis, such as in aeronautics, transport, mining, among others. Erosion is an abrasive wear process such that the repeated impact of small particles moving fluid against a surface results in the removal of material from that surface [55]. According to [56] erosion is defined as: "Material damage caused by the attack of particles dragged in a fluid system, impacting the surface at high speed".

When modeling erosive wear, there is a common problem in the study of different types of wear, which corresponds to a large number of variables related to the tribo-system, which can influence the rate of material loss. Some of the variables that affect erosion can be classified under three topics [57]:

1. Impact variables describing the particles flow
   (a) The Angle of impact;
   (b) Particle velocity;
   (c) Particle concentration;
   (d) Rotation of particles on impact;
   (e) Impact time;
2. Particle variables:
   (a) Particle shape;
   (b) Particle density;
   (c) Particle size.
3. Material variables (counterpart and particles)
   (a) Young's modulus;
   (b) Poisson's coefficient;
   (c) Plastic behavior;
   (d) Nature of the carrier fluid and its temperature;
   (e) Failure behavior;
   (f) Hardness of materials.

REFERENCES

[1] MERIAM, J. L. Mecânica para engenharia. *Dinâmica, 6.ed. Rio de Janeiro*, 2009.

[2] HOEK E., . M. C. D. Fracture initiation and propagation in intact rock - A review. *Journal of Rock Mechanics and Geotechnical Engineering*, 2014.

[3] FILHO, C. l. M. Introdução à geologia de engenharia. *(5ed Santa Maria, RS. Ed. da UFSM.307p)*, 2014.

[4] ANSYS. Theory Manual. *Ansys*, v. 5.2, 1995.

[5] ABAQUS. Analysis User's Guide. *Dassault Systèmes*, v. 1, 2, 3, 4 and 5, p. 4979, 2014.

[6] HIBBITT, D.; KARLSSON, B.; SORENSEN, P. Analysis User's Manual: Prescribed Conditions, Constraints Interactions. *Dassault Systèmes, Providence*, v. 5, 2010.

[7] HIBBITT, D.; KARLSSON, B.; SORENSEN, P. Abaqus Theory Manual. *Dassault Systèmes, Providence*, 2011.

[8] JONHSON, K. L. Contact Mechanics. *Cambridge University Press, Cambridge, UK. ISBN-0-521-25576-7*, 1985.

[9] TIMOSHENKO; GOODIER. Theory of Elasticity. *3rd Edition, McGraw-Hill Kogakusha, Lda, Tóquio, Japão. ISBN-0-47-085805-5.*, 1970.

[10] BORESI, e. a. A. P. Advanced Mechanics of Materials. *3rd Edition, John Wiley Sons, New York, USA. ISBN-0-471-08892-7.*, 1978.

[11] DOCA, T. PRODEM. *Seminar on Computational Contact Mechanics*, 2010.

[12] ROYLANCE, D. Mechanical Properties of Materials. *Massachusets: MIT*, 2008.

[13] INSTRON. Yield Point. *São José dos Pinhais, PR,2021. Available in: <https://www.instron.com/pt-br/our-company/library/glossary/y/yield-point?region=Brasillang=pt-BR>. Acess in: Sept. 29th, 2021*, 2021.

[14] ARAúJO, F. A. Contribuição ao emprego da Mecânica do Dano para a análise do comportamento dinâmico não-linear de vigas em concreto armado. *Dissertação de Mestrado. Escola de Engenharia de São Carlos, Universidade de São Paulo, São Carlos*, 2003.

[15] GAMINO, A. L. Modelagem física e computacional de estruturas de concreto reforçadas com CFRP. *Tese de Doutorado (Ed. Ver.). Escola Politécnica da Universidade de São Paulo. São Paulo, 259 p.*, 2007.

[16] KACHANOV, L. Introduction to Continuum Damage Mechanics. *Kluwer Academic Publishers Journal, Brookline*, 1986.

[17] PATERSON M. S., . W. T. Experimental Rock Deformation - The Brittle Field. Experimental Rock Deformation - The Brittle Field (2nd Ed.). *Netherlands: Springer-Verlag Berlin Heidelberg*, 2005.

[18] ZHANG W., . C. Y. Continuum Damage Mechanics and Numerical Applications. (Zhejiang University Press, Org.). *Springer-Verlag Berlin Heidelberg.*, 2010.

[19] SHZU, M. A. M. Avaliação do processo de Ruptura de vigas de concreto considerando os aspectos dinâmicos. *Tese de Doutorado em Estruturas e Construção Civil, Publicação E..TD-003A/06, Departamento de Engenharia Civil e Ambiental, Universidade de Brasília, Brasília,179p*, 2006.

[20] BITTENCOURT, A. G. Efeito da radiação gama em blindagens balísticas compósitas de poliaramida. *DISSERTAÇÃO DE MESTRADO – Instituto Militar de Engenharia, Departamento de Ciência e Tecnologia, Rio de Janeiro*, 2011.

[21] FERREIRA, L. E. T. e. J. B. d. H. Mecânica da fratura. *Materiais de construção e princípios de ciência e engenharia de materiais. São Carlos: IBRACON*, 2010.

[22] MICHELI, G. Análise numerico-experimental do impacto em chapas de alumínio aeronáutico. *São Paulo*, 2008.

[23] ADAMS, B. Simulation of ballistic impacts on armored civil vehicles. *Eindhoven University of Technology*, v. 06, 2003.

[24] JOHNSON G. R., C. W. H. Fracture characteristics of three metals subjected to various strain rates, temperatures and pressures. *Engineering Fracture Mechanics, vol 21, No. 1*, 1985.

[25] SAMPAIO, M. A. B. Mecânica do contato com o método dos elementos de contorno para modelagem de máquinas tuneladoras. *São Paulo*, 2009.

[26] HERTZ, H. Ueber die Beruehrung elastischer Koerper (On Contact Between Elastic Bodies). *1882, in Gesammelte Werke (Collected Works), Vol. 1, Leipzig, Germany*, 1895.

[27] CATTANEO, C. Sul contatto di due corpi elastici: distribuzione locale degli sforzi. *Rend. Accad. Naz. Lincei, v. 27, n. 6, p. 342–348*, 1938.

[28] MINDLIN, R. Compliance of elastic bodies in contact. *(Journal of applied mechanics, v. 16, p. 159–268)*, 1949.

[29] JOHNSON, K. L. Contact Mechanics. 2003.

[30] ARAUJO S. G. A. ; DOCA, T. C. R. IMPLEMENTAÇÃO DE SOLUÇÕES ANALÍTICAS DE PROBLEMAS DE CONTATO SUPERFICIAL UTILIZANDO VBASIC. *(Apresentação de Trabalho/Congresso)*, 2017.

[31] BIENIAWSKI, Z. T. Mechanism of brittle fracture of rock: Part I - Theory of the fracture process. *International Journal of Rock Mechanics and Mining Sciences Geomechanics Abstracts*, 1967.

[32] LEMAîTRE, J. A course on damage mechanics. *Springer, New York*, 1991.

[33] MARTIN, C. D. A model for non-linear rock deformation under compression due to sub-critical crack growth. *International Journal of Rock Mechanics and Mining Sciences Geomechanics Abstracts*, 1993.

[34] MARTIN C. D., . C. N. A. The progressive fracture of Lac du Bonnet granite. *International Journal of Rock Mechanics and Mining Sciences Geomechanics Abstracts*, 1994.

[35] AUBERTIN M., . S. R. A damage initiation criterion for low porosity rocks. *International Journal of Rock Mechanics and Mining Sciences Geomechanics Abstracts*, v. 15, 1997.

[36] BASU A., C. T. B. . B. A. A. Evaluation of rock mechanical behaviors under uniaxial compression with reference to assessed weathering grades. *Rock Mechanics and Rock Engineering*, v. 93, 2009.

[37] VIDAL F. W. H., A. H. C. A. C. Tecnologia das rochas ornamentais: pesquisa, lavra e beneficiamento. *Rio de Janeiro: CETEM/MCTI, 700p*, 2013.

[38] LUIS, I. G. d. V. Ingeniería geológica. *Madrid. Prentice Hall*, 2002.

[39] COSTA, A. Uma aplicação de Métodos Computacionais e Princípios de Mecânica das Rochas no Projeto e Análise de Escavações destindas a Mineração Subterranea. *UFRJ. Tese de Doutorado 170p*, 1984.

[40] HUEBNER, K. T. E. The finite element method for engineers. *New York, John Wiley Sons*, v. 2, 1982.

[41] RAO, S. The finite element method in engineering. *Oxford, Pergamon Press*, 1989.

[42] OWEN D.; HINTON, E. Finite Elements in plasticity: theory and pratice. *Swansea, UK, Pineridge Ltda.*, 1980.

[43] HUEBNER, K. T. E. The finite element method for engineers. *J. Wiley, New York*, 1994.

[44] BATHE, K. J. Theory Manual. *Prentice Hall*, 1996.

[45] DIETER, G. E. Mechanical Metallurgy. *International Student Edition. Japan: McGraw-Hill Book*, 1961.

[46] JOHNSON G. R., C. W. H. A constitutive model and data for metals subjected to large strains, high strain rates and high temperatures. *Proc. 7th Int. Symp. on BuNistics, pp. 541547. The Hague, The Netherlands. April*, 1983.

[47] TAVARES S. S. M., P. J. M. A. H. F. G. N. C.; SILVA M. SARTURI, F. D. M. Tensile Properties of Duplex UNS S32205 and Lean Duplex UNS S32304 Steels and the Influence of Short Duration 475 °C Aging. *Materials Research*, 2012.

[48] RICE J. R., T. D. M. On the ductile enlargement of voids in triaxial stress fields. *Journal of the Mechanics and Physics of Solid, vol. 17*, 1969.

[49] BRZOSTEK, R. C. Estudo da fratura em solda ponto por fricção em alumínio AL-CLAD 2024 T351 e Alumínio 2014-T351: Uma abordagem numérica e experimentall. *Dissertação (Mestrado em Engenharia) – Universidade Federal do Rio Grande do Sul, Porto Alegre*, v. 1, 2012.

[50] LUBLINER J., O. J. O. S.; OñATE, E. A plastic damage model for concrete. *Int. J. Solids Structures, 25(3)*, 1988.

[51] LEE, J.; FENVES, G. L. Plastic-damage model for cyclic loading of concrete structures. *Journal of Engineering Mechanics, 124:892–900*, 1998.

[52] KMIECIK, P.; KAMI´NSKI, M. Modelling of reinforced concrete structures and composite structures with concrete strength degradation taken into consideration. *Archives of Civil and Mechanical Engineering, 11(3):623–636*, 2011.

[53] VILNAY M., C. L.; COTSOVOS, D. M. Advanced material modelling of concrete in abaqus. *9th International Concrete Conference: Environment, Efficiency and Economic Challenges for Concrete*, 2016.

[54] LUBLINER J., O. J. O. S.; OñATE, E. A plastic damage model for concrete. *Int. J. Solids Structures, 25(3):299–326.*, 1989.

[55] HUTCHINGS, I. Particle erosion of ductle metals: a machanism of material removal. *Wear 27*, 1974.

[56] BITTER, J. A study of erosion phenomena. *Wear 6*, 1963.

[57] FINNIE, I. Some observations on erosion of ductile metals. *Wear*, 1971.